Ion Interactions with Carbon Nanomaterial Surfaces in Aqueous and Non-aqueous Solutions

Dissertation

zur Erlangung des akademischen Grades eines
Doktors der Naturwissenschaften
– Dr. rer. nat. –

vorgelegt von

Andrey I. Frolov

geboren in Ivanovo, USSR

Fakultät für Chemie
der
Universität Duisburg-Essen

2011

Die vorliegende Arbeit wurde im Zeitraum von Juli 2008 bis Juni 2011 im Arbeitskreis von PhD, DSc, Priv.-Doz. Maxim V. Fedorov am Max-Planck-Institut für Mathematik in den Naturwissenschaften, Leipzig, durchgeführt.

Tag der Disputation: 20.09.2011

Gutachter:	PhD, DSc, Priv.-Doz. Maxim V. Fedorov
	Prof. Dr. Eckhard Spohr
Vorsitzender:	Prof. Dr. Thomas Schrader

Contents

List of Figures

List of Tables

1 Introduction

1.1 Salt effects at solvation interfaces

Electrolyte solutions are widely present in nature. Indeed, almost whole liquid water on Earth possesses dissolved salts: oceans, seas, and to less extent lakes and rivers are solution of different salts. Consequently, all the biological liquids: cytoplasm, blood, lymph, etc. contain ions. Most of the technological liquids contain, either as additives or impurities, dissolved ions. Thus, understanding ionic solvation is important for almost any process taking place in liquid phase.

There are very many known salts: from alkali halides (like NaCl) to salts constituting of bulky molecular ions (like ionic liquids). Different ions have different solvation properties. Some salts are very well soluble (like NaCl in water), some are not (like $BaSO_4$ in water). Different ions interact with solvent molecules and other ions in a different way. Thus, using different ions one can adjust the properties of the buffer solvent. The pioneering work in this direction was done by Franz Hofmeister [1], who investigated effects of different ions on the stability of proteins in aqueous solutions. Since then, a lot of work has been done on specific ion effects [2, 3]. But still there are open question and a lot of new studies appear in the field.

1.2 Carbon nanomaterials

There is a big breakthrough in nanotechnology nowadays [6]. Carbon nanomaterials (CNM) are promising objects for a wide range of applications in different areas: photonics, electronics, supercapacitors, sensorics, drug delivery, etc. [7]. There are different carbon nanomaterials: carbon nanotubes, fullerenes, carbon “nanoonions“, etc. (see Figure 1).

Carbon "nanoonions" (CNOs) are spherical nanoparticles with 5-10 nm diameter consisting of concentric shells of graphene sheets that can be considered as multi-shell fullerenes [8] (see Figure 1b). Due to their ability to handle high power, CNOs have recently attracted attention for electrodes of micro-supercapacitors [8].

Carbon nanotubes (CNTs) are cylindrical nanoobjects which can be considered as the rolled-up graphene sheets. There are single-wall and multi-wall CNTs [7]. *Single-wall CNTs (SWNTs)* have diameter range from 0.4 to 3 nm [7]. Despite the structure of a SWNT is similar to the structure of a single graphene sheet, which possesses semi-conductor properties, SWNTs can be both metallic or semiconducting [7]. Whether a SWNT is metallic or semiconducting is determined by the direction about which the graphene sheet is rolled to form the SWNT (see

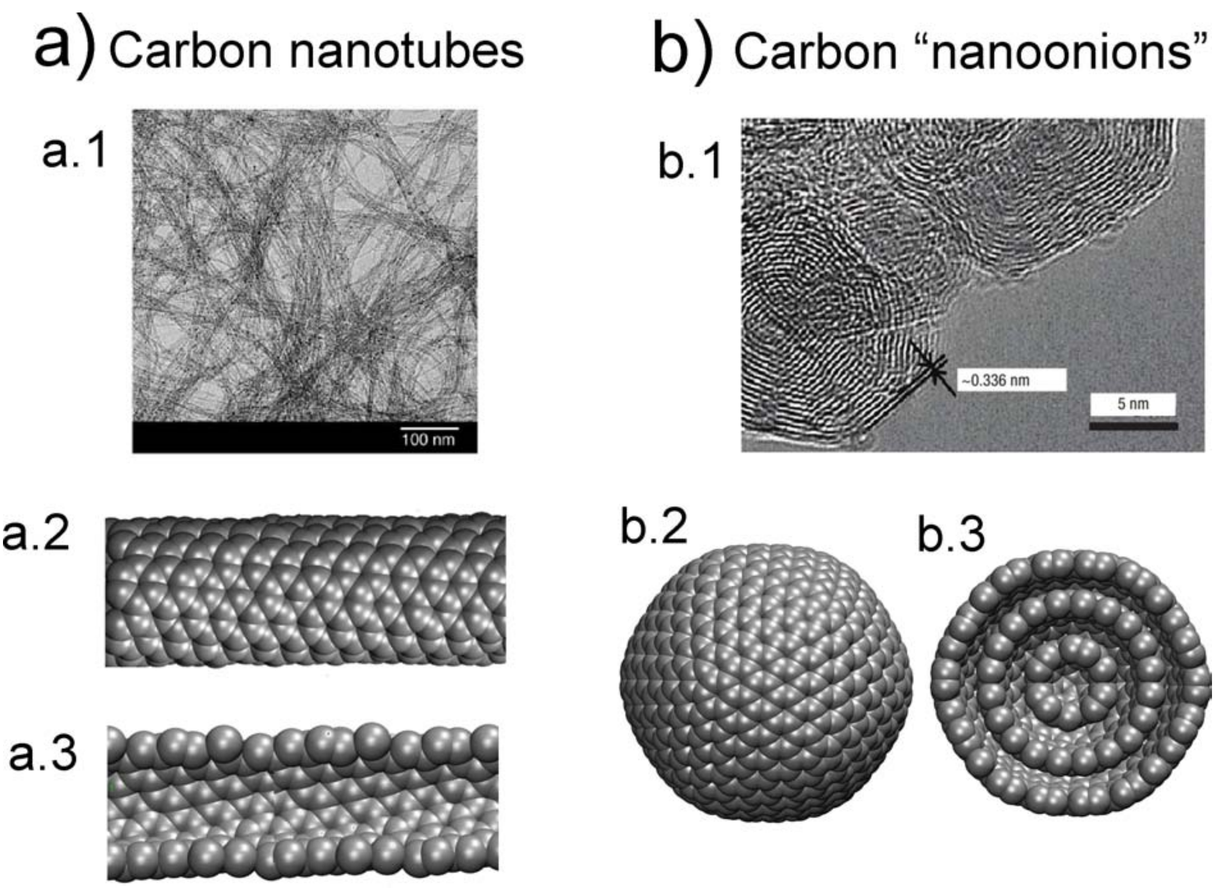

Figure 1: Carbon nanomaterials considered in the study. a) Carbon nanotubes: a.1. transmission electron microscopy (TEM) image of single walled CNTs (replotted from the reference [4] with permissions, Copyright ©2003, American Association for the Advancement of Science), a.2. model of the single-walled CNT in molecular dynamics (MD) simulations, carbon atoms are represented by grey balls, a.3. slice of the model CNT. b) Carbon "nanoonions": b.1. TEM image of the carbon "nanoonions" (replotted from the reference [5] with permissions, Copyright ©2007 Elsevier), b.2. model of the carbon "nanoonion" in MD simulations, carbon atoms are represented by grey balls, b.3. slice of the model carbon "nanoonion" representing the layered structure.

Figure 2). This direction is uniquely defined by the chiral vector of the CNT, which can be specified by two integer coefficients (n, m) in the superposition of the graphene unit vectors $\mathbf{a_1}$ and $\mathbf{a_2}$ (see Figure 2a). To construct a SWNT of certain chirality from the graphene sheet one has to roll the graphene sheet around the axis perpendicular to SWNT chiral vector, such that the start and end points of the chiral vector "meet" each other in one point. The chiral vector can be written as:

$$\mathbf{C} = n\mathbf{a_1} + m\mathbf{a_2}, \tag{1}$$

where $\mathbf{a}_1$ and $\mathbf{a}_2$ are graphene units vectors (as defined on the Figure 2), n and m are integer coefficients. One can distinguish several types of SWNT chiralities: armchair (n=m), zigzag (n=0 or m=0), or chiral (all other variants of the n and m combination) [7] (see Figure 2b). All armchair SWNTs are metallic. Those SWNTs with ($n - m$) evenly divisible by 3 are semi-conductors with a tiny band-gap, thus we consider them as metallic. All others are semiconductors having the band gap inversely proportional to the nanotube diameter [7]. *Multi-wall CNTs (MWNTs)* are usually metallic, because there is a high probability to observe a metallic SWNT inside a MWNT.

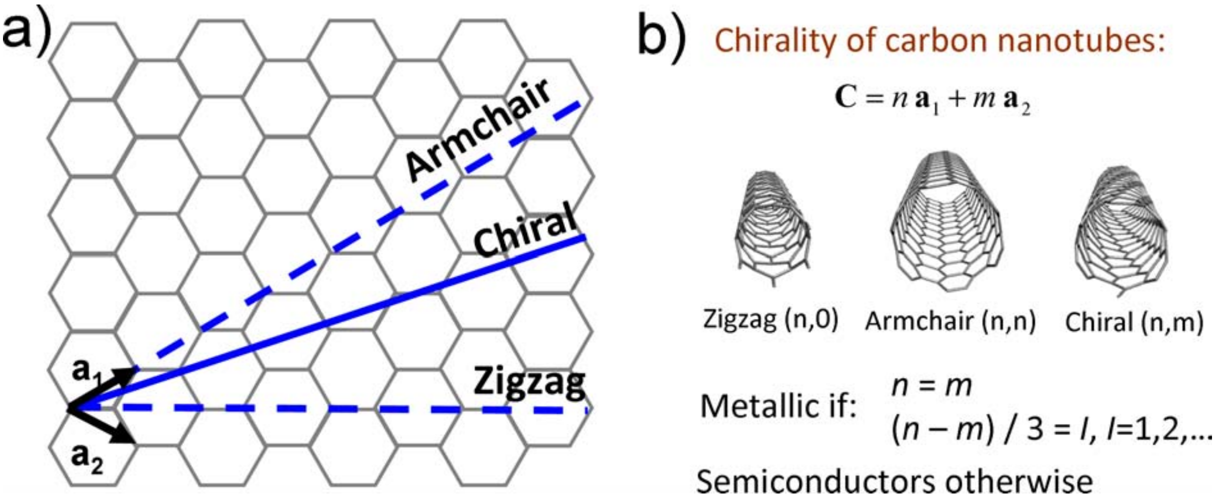

Figure 2: Carbon nanotubes are rolled graphene sheets. a) Representation of a graphene sheet. By the blue lines we illustrate the possible rolling axes of the graphene sheet. The vectors $\mathbf{a_1}$ and $\mathbf{a_2}$ are unit vectors of the graphene lattice. The picture is adopted from Ref. [9]. b) Carbon nanotube chirality resulting from different chiral vectors. The chiral vector **C** is a superposition of the unit vectors of the graphene sheet. To construct a SWNT of certain chirality from the graphene sheet one has to roll the graphene sheet around the axis perpendicular to SWNT chiral vector, such that the start and end points of the chiral vector "meet" each other in one point.

1.3 Importance of carbon nanomaterial dispersions

Most of applications require solubilisation of CNMs because solutions provide a convenient instrument to manipulate the materials. Liquid dispersions of carbon nanomaterials, and in particular CNTs, are a subject of intensive research these days due to their wide areas of applications [10, 11, 12, 13, 14]. However, the inert nature of the CNM surface makes them extremely solvophobic to the most of commonly used solvents [10, 11, 12, 13, 14]. That poses a great challenge for chemists and nanoscientists working on CNM applications. As a consequence, there have been spent many efforts to find efficient ways of dispersing CNMs in liquid phase either through chemical modification of their surface [10, 11, 12, 15, 16] or through adding dispersing agents (e.g. surfactants) into solution to stabilize the CNM dispersions [14, 17, 18, 19, 20, 10, 21, 22].

1.3.1 Aqueous dispersions

The CNM aqueous dispersions are important for many application areas of CNMs such as photonics, biological and environmental sensing, drug delivery and bioimaging [7, 23, 24]. CNM aqueous dispersions hold great promise as functional or processing liquids in micro/nano systems. The CNMs aqueous dispersions could be used inside of micro-fluidic devices targeting specific biomolecules [25] or as essential components in the emerging solvent based molecular engineering processes, e.g. in the Langmuir-Blodgett deposition of aligned CNTs array [26] or nano-ink printing of CNT functional arrays [27].

Although water as a solvent is unavoidable in many bio-related applications of CNMs [17, 16, 28], this is not the best solvent for making stable CNM dispersions [29, 30]. It is practically impossible to disperse any noticeable amount of pristine CNTs in bulk water, where in the absence of dispersants any pristine carbon materials instantly precipitate [14, 29]. Thus, solubilization of carbon nanotubes in water requires either covalent or noncovalent functionalization of nanotubes [20, 15, 10].

1.3.2 Organic solvent dispersions

Recently, it has been shown that several organic solvents, like N-methyl-2-pyrrolidone (NMP) are much more efficient for dispersing CNTs and other CNMs than water [29, 30, 31, 32]. Such, it has been shown that it is possible to disperse considerable amounts of pristine CNTs and graphene in bulk NMP without adding any dispersing agents [31]. That explains why these days non-aqueous (organic) solvents attract considerable attention of experimental nanoscientists as well as theoreticians [30, 32, 33, 34].

Recently, the mechanisms of interactions between CNM species in organic solvents were investigated by molecular dynamics simulations. In the work of Mac Kernan and Blau [34] it was found that a single layer of NMP raises a big barrier between interacting carbon nanotubes in CNT-NMP dispersions, preventing their aggregation into bundles. Similar effects were observed for graphene sheets by Shih et al. [32]. They showed that the origin of the barrier is the strong van der Waals interactions of the confined NMP molecules with the surface of the graphene sheets. In contrast, as the results of Ref. [32] show, there is almost no such a barrier in aqueous solution, because of the weak water molecules interactions with the inert surface of graphene [32]. We note, however, that the discussed works were mainly focused on the mechanisms of CNM aggregation, rather than on molecular effects of solvent environment associated with dispersion mechanisms of a single CNT or graphene sheet in NMP. Still, there is lack of information about the molecular-scale effects at the CNM-organic solvent interface. The role of other dispersion components (ions, cosolvents, cosolutes) is also not clear.

1.3.3 Ionic Liquid dispersions

Interest in CNMs dispersed in room temperature ionic liquids (RTILs) is rapidly growing these days [35, 36, 37, 38]. One of the main reasons is the extraordinary electrochemical properties of RTILs [39, 40, 41, 42, 43] as well as of CNM composite materials [35, 36, 44]. Such, the use of CNTs (e.g. nanotube forest) and ionic liquids has promising supercapacitor applications [36, 45, 37]. We also note that in many emerging electrochemical applications, RTILs are actively used in mixtures with organic solvents (e.g. acetonitrile) to avoid problems related with the high viscosity of neat RTILs [46, 36, 47].

It has been shown that RTILs based on a combination of imidazolium-based cations with hydrophobic anions (e.g. BF_4 or bis (trifluoromethylsulfonyl) imide (TFSI)) are moisture stable and have promising electrochemical applications [42]. Among those, the TFSI-based RTILs have good stability (such, in Ref. [42] there have been discussed that the BF_4 anion is not stable against carbon electrodes) and have large electrochemical window [48, 49]. Ion conductivity of EMIm-TFSI (EMIm satys for 1-ethyl-3-methylimidazolium) is comparable to the best of organic electrolyte solutions [35] and this liquid is stable (no decomposition) up to 300-400°C. The TFSI-based ionic liquids are practically not miscible with water but they are well miscible with several organic solvents as, e.g., acetonitrile [50].

It has been shown in many experimental [51, 52, 41, 53, 54, 55, 56, 57] and theoretical [58, 59, 60, 61, 62, 63, 64, 65, 66] studies that the molecular structure of RTIL ions strongly influences the structure of the RTIL liquids at different charged and uncharged interfaces. Such, in several experimental studies the orientation of ionic liquid molecular ions were investigated at the liquid - vacuum interface [52, 67, 68]. Nakajima et al. [67] investigated the liquid - vacuum interface of different 1-alkyl-3-methylimidazolium – bis (trifluoromethylsulfonyl) imide ionic liquids using the high-resolution Rutherford backscattering spectroscopy. They showed that, due to the solvophobic nature, long alkyl chains of cations point away from the bulk liquid to vacuum and therefore stimulate the imidazolium ring to stay perpendicular to the surface. Lockett et al. [52] showed that asymmetry in the size and shape of molecular ions results in unequal distribution of molecular cations and anions in a direction normal to the RTIL-vacuum interface. These results suggest that the molecular structure of RTIL ions should make significant effects at the CNM-RTIL interfaces. However, there is a lack of molecular level information on the mechanisms of the RTIL interactions with nanocarbon electrodes. Even less is known about the molecular effects of organic solvent on the interface properties of RTIL-solvent mixtures at the nanocarbon surfaces. The basic mechanisms of the electrical double layer formation in such systems (particularly, in RTIL-acetonitrile mixtures) are also not sufficiently explored.

Due to the recent progress in molecular-level experimental techniques there has been obtained very important information on the layering structure of ionic liquids at neutral and charged interfaces [69, 55, 56, 70]. Endres et al. [56] quoted an "undoubted" formation of at least three solvation layers of EMIm-TFSI on metal electrodes detected by atomic force microscopy (AFM) (note, that they name EMIm-TFSI as 1-ethyl-3-methylimidazolium bis [trifluoromethylsulfonyl] amide). Recently, Hayes et al. [70] investigated the influence of the electric potential on the interface solvation layers in 1-ethyl-3-methylimidazolium tris (pentafluoroethyl) trifluorophosphate ([EMIm]FAP) and 1-butyl-1-methylpyrrolidinium tris (pentafluoroethyl) trifluorophosphate ([Py]FAP) by AFM. Applying an electric potential, they found that the innermost layer changes its structure and becomes more strongly bound to the surface. At the cathode, for "the first time an interfacial (innermost) anionic layer at a solid interface has been detected by AFM".

However, still many details of the interface structure of RTILs and their mixtures are not easily accessible by direct experiments. Molecular simulations can provide complimentary information to the experimental data that should help to obtain a detailed picture of the interface phenomena in RTIL systems (see more discussion on this subject in Ref. [36]). Therefore, we decided to use fully atomistic simulation methods to study basic mechanisms of the RTIL interactions with the CNT surface.

1.4 Ion effects on carbon nanomaterial dispersion properties

The effects of ions may be of particular interest here because, as it is known from biochemical and colloidal sciences, ions may have profound effects on stability of biomolecular [71, 72, 73] and colloidal dispersions [74, 75, 76, 77], interacting in different ways with biomolecules and dispersed particles [71, 78, 79]. Recently, ion effects attracted attention of scientists working on CNMs dispersions.

Firstly, the most of technical and biological aqueous environments of CNMs contain different salts and, as it has been recently reported by several groups, the salt ions make significant effects on physical-chemical properties of CNMs in water solutions [80, 81, 82, 83, 84].

Secondly, as it has be discussed earlier, SWNTs of different chirality possess very different properties. Thus, to efficiently exploit the properties of a certain CNT chirality, one has to find a way of effective chirality separation, because as prepared samples of CNTs contain mixtures of metallic and semiconducting CNTs with a wide range of diameter distributions [7]. The selective separation of CNTs chiralities is a great challenge, which limits nanotechnological applications of CNTs. But so far there is no universal and efficient method for CNT separation. Recently, it has been shown that a salt addition into the SWNT dispersions might serve as an efficient tool for chirality separation of CNTs [81, 80, 84]. Niyogi et al. reported a way of "diameter-dependent separation of metallic and semiconducting SWNTs, without the use of any additional cosurfactant" with the use of salt addition in the SWNT dispersions and the subsequent ultracentrifugation [81]. Ju et al. showed that an efficient individualization and chirality enrichment of the (8,6) SWNTs from a nanotube sample with broad diameter distribution could be achieved using two types of surfactants and a salt addition [85]. These works indicate the potential and importance of the use of salt addition as a tool for tuning physico-chemical properties and stability of nanoobject solutions and dispersions, and for selective diameter and chirality separation of the CNTs from their dispersions.

The solvation properties of SWNTs are usually monitored by absorption, photoluminescence (PL) and Raman spectroscopy via investigation of resonance features for specific nanotubes chiralities [80, 81]. Semiconducting SWNTs produce photoluminescence (PL) spectra [86]. Importantly, the semiconducting SWNTs show different characteristic "spots" on the excitation-emission PL two dimensional map [86], which makes it possible to analyze the SWNT chirality population in the SWNT dispersions. The SWNT PL is of vital importance for realization of CNT sensor applications using the fluorescence resonance energy transfer between CNT and its biological/chemical surroundings and for the development of ultrafast photonics CNT-based devices using PL quenching effects [29, 87, 88, 89, 90]. It was shown that different ions can make various effects on the PL spectra of SWNTs in aqueous dispersions stabilized by surfactants [80, 81, 82, 83, 84]. However, we are not aware about a detailed study of ion effects on CNTs in their organic solvent dispersions. Partially, this can be explained by the fact that many commonly used inorganic salts (e.g. NaCl) are hardly soluble in organic solvents such as NMP [91]. The salts addition manifests itself in modification of the electric field around nanotubes by ions, resulting in the quenching of PL of SWNTs [80, 81, 82]. Importantly, Brege et al. revealed that the strength of PL quenching effect has strong correlation with the ionic radius of the quenching ions, showing the increase in quenching with the increase in the ionic radius [82, 83].

Despite of the widespread reports on significant ion effects on physical-chemical properties of CNMs, the molecular mechanisms of ion interactions with the CNM surfaces are still far from complete understanding and further experimental and theoretical investigations are required.

2 Theoretical background

2.1 Molecular parameters and functions describing ionic solutions

2.1.1 Radial Distribution Function

The radial distribution function $g(r)$ (RDF) is an important property characterizing the structure of condensed systems. It can be obtained experimentally from X-ray or neutron scattering (see for example Ref. [92]). The RDF function is defined through the following relation (for distribution of particles a around particles x) [93]:

$$\rho_a \int g_{xa}(r) 4\pi r^2 dr = N_a - 1 \tag{2}$$

where ρ_a is the number density of the particles a, N_a is the number of particles a in the sample, r is the distance between particles x and certain point in the the space.

The function shows the ensemble average of the relative density profile of particles a at the certain distance r from a particle x:

$$g_{xa}(r) = \left\langle \frac{\rho_a(r)}{\rho_a^0} \right\rangle_{ensemble} \tag{3}$$

where ρ_a^0 is the number density of particles a in the bulk liquid.

An example RDF is given on the Figure 3.

2.1.2 Pair Correlation Function

For homogeneous liquid systems the RDF function is equal to the Pair Correlation Function (PCF) of the corresponding particles [93]. For simplicity let us consider the distribution of particles a around the particles of the same type in an one-component liquid. We consider ensemble of indistinguishable particles. The general definition of the PCF is given via Pair ($\rho^{(2)}(\mathbf{r}_1, \mathbf{r}_2)$) and Unitary Distribution Functions ($\rho^{(1)}(\mathbf{r}_i)$) (we omit subscript a at the functions for simplicity):

$$g^{(2)}(\mathbf{r}_1, \mathbf{r}_2) = \frac{\rho^{(2)}(\mathbf{r}_1, \mathbf{r}_2)}{\rho^{(1)}(\mathbf{r}_1)\rho^{(1)}(\mathbf{r}_2)} \tag{4}$$

where $\mathbf{r}_i$ is the radius-vector of the particle i in the space.

The Pair Distribution Function ($\rho^{(2)}(\mathbf{r}_1, \mathbf{r}_2)$) shows the probability that one molecule of the system will be found in elementary volume $d\mathbf{r}_1$ at $\mathbf{r}_1$ and another in $d\mathbf{r}_2$ at $\mathbf{r}_2$, if a configuration of the system is observed [93].

The ensemble average definition of the PCF would be [93]:

$$g^{(2)}(\mathbf{r}_1, \mathbf{r}_2) = \frac{N(N-1)}{\rho^{(1)}(\mathbf{r}_1)\rho^{(1)}(\mathbf{r}_2)} \frac{\int ... \int U(\mathbf{r}_1 ... \mathbf{r}_N) d\mathbf{r}_3 ... d\mathbf{r}_N}{Z_{conf}} \tag{5}$$

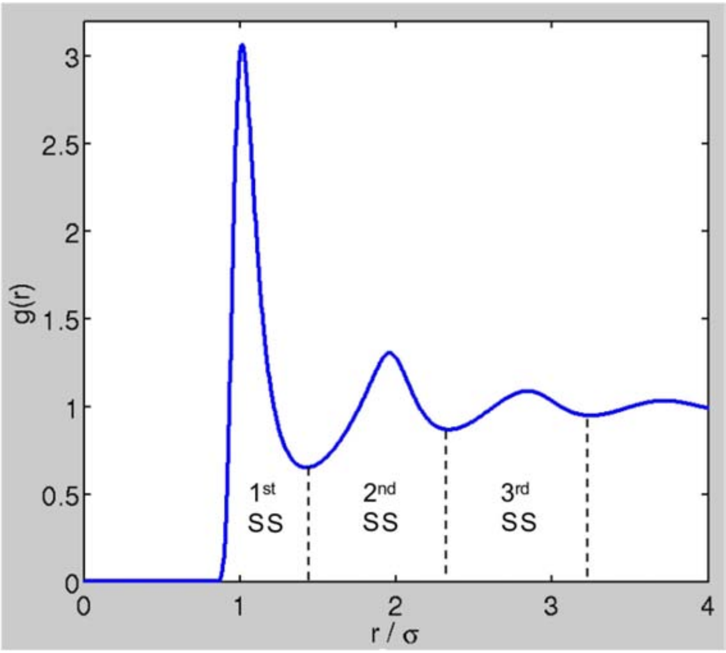

Figure 3: Definition of the solvation shells based on the particle-solvent radial distribution function $g(r)$. Distance is given in the diameters of the solvent molecules (σ). Thin dashed lines indicate the boundaries of the first, second and so on solvation shells (SS), which usually correspond to the positions of the minima on the $g(r)$.

where the Z_{conf} is the configuration integral of the system, N is the number of molecules in the ensemble, U is the potential energy of the system, k_B is the Boltzmann constant, T is temperature. The integration is performed over the positions of all particles in the ensemble except two of them.

For homogeneous liquid the Unitary Distribution Functions is constant and equal to the bulk density of the liquid ($\rho^{(1)}(\mathbf{r}_i) = \rho$) [93]. The mutual correlations of the particles depend only on the relative distance between particles $r = |\mathbf{r}_1 - \mathbf{r}_2|$, rather than on the absolute positions of the particles. Thus, the Equation 4 reduces to:

$$g^{(2)}(0, r) = \frac{\rho^{(2)}(0, r)}{\rho^2} \tag{6}$$

which corresponds to the definition of the RDF.

2.1.3 Potential of Mean Force

Potential of Mean Force (PMF) can be defined in different ways. Let us consider a homogeneous system containing N spherically symmetric particles in volume V with temperature T (NVT-ensemble). The most intuitive way to define the PMF would be as follows:

1. PMF is an effective potential acting between two molecules *i* and *j* in the condensed phase. Let us first consider the interaction between two molecules (i and j) in the gas phase, where we may neglect the interactions of the two molecules with all others. The interaction between the two molecules results in the forces acting on these two molecules, since the force is the minus gradient of the interaction potential. The forces result in the accelerations of the particles. So, the i^{th} molecule causes force on the j^{th} molecule, and the j^{th} molecule causes force on the i^{th} molecule.

We employ the same scheme for the liquid phase. Let us consider molecules i and j out of an ensemble of N molecules. In the ensemble of molecules the forces acting on the molecules i and j are not only the result of mutual interaction of the molecules i and j but also their interactions with all other molecules in the ensemble of N molecules. Let us formulate this in the following way: the molecules i and j interact with each other via a modified (compared to the gas phase) potential, this potential includes an average influence of all particles onto i and j molecules. This potential is called the Potential of Mean Force (PMF). This potential results in a force acting on the molecule j at the distance r from the molecule i. The force is exactly the averaged (over the ensemble) force acting on the molecule j having occurred at distance r from the molecule i in the ensemble of N molecules.

The definition of the PMF via ensemble average of the force acting on the particle j $(-\overrightarrow{grad}_j U)$ reads:

$$-\overrightarrow{grad}_j PMF(\mathbf{r}_{ij}, \Omega_{ij}) = \frac{\int ... \int exp(-\beta U)(-\overrightarrow{grad}_j U) d\mathbf{r}_3 ... d\mathbf{r}_N d\mathbf{\Omega}_3 ... d\mathbf{\Omega}_N}{\int ... \int exp(-\beta U) d\mathbf{r}_1 ... d\mathbf{r}_N d\mathbf{\Omega}_1 ... d\mathbf{\Omega}_N} \qquad (7)$$

where β is the inverse temperature ($\beta = (k_B T)^{-1}$), U is the potential energy of the system, $\overrightarrow{grad}_j$ is gradient operator on the position of particle j, the denominator is the configuration integral of the system (Z_{conf}). Thus PMF is the potential that causes the mean force acting on the particle j.

From this definition PMF can be calculated in the following way. Let us consider the Molecular Dynamics (MD) simulation of the system of N spherical particles. On each integration step we choose 2 molecules, let say i and j, calculate the distance r between them, and store the forces acting on the molecule j (calculated in the MD scheme). Then we repeat the procedure for a sufficient number of MD integration time steps. Finally we average all the stored forces that appeared we collected for the same separations between particles from r to $r + dr$, where dr is a specified resolution of the PMF function. Now, we have the "mean force" between two particles in the system as the function of r. Integral of the "Mean Force" will give us the "Potential of Mean Force" as the function of r.

PMF can be calculated not only as a function of r, but actually as a function of any spatial variable (e.g. angles) and their combinations. It may also be a function of coordinates of several particles.

2. PMF can be defined through the n-particle correlation functions.

Let us define the PMF between two non-spherical particles in a one-component homogeneous system in NVT-ensemble through the following relation [94]:

$$PMF(\mathbf{r}_{ij}, \Omega_{ij}) = -k_B T \ln g(\mathbf{r}_{ij}, \Omega_{ij})$$

where $g(\mathbf{r}_{ij}, \Omega_{ij})$ is the molecular pair correlation function, $\mathbf{r}_{ij} = \{x_{ij}, y_{ij}, z_{ij}\}$ and $\Omega_{ij} = \{\phi_{ij}, \theta_{ij}, \psi_{ij}\}$ are the radius-vector between i^{th} and j^{th} molecules (e.g. between their center of masses) and the relative orientations of the i^{th} and j^{th} molecules (given by a set of Euler angles). Equivalently we can write:

$$g(\mathbf{r}_{ij}, \Omega_{ij}) = e^{-\beta PMF(\mathbf{r}_{ij}, \Omega_{ij})} \tag{8}$$

where β is the inverse temperature ($\beta = (k_B T)^{-1}$).

It can be showed [94] that substituting the expression (Equation 8) into the definition of the pair correlation function (Equation 5) will result in Equation 7.

3. PMF can be defined through the thermodynamic cycle.

PMF is the work involved (the Helmholtz energy in the NVT-ensemble or the Gibbs energy in the NPT-ensemble) in bringing two (or many) selected particles from infinite separation (in the condensed phase) to the final configuration (in the condensed phase) [94].

For homogeneous system containing N spherically symmetric particles in volume V with temperature T (NVT-ensemble) the two particle PMF would be:

$$PMF(r) = A(r) - A(\infty) \tag{9}$$

where A is the Helmholtz free energy.

All the three definitions of PMF are equivalent.

2.1.4 Solvation/Hydration shell

Let us consider an ion dissolved in water. Ion attracts water molecules, and as the result, a certain number of attracted water molecules are situated around the ion. The water molecules form a "shell" around the ion. The rest water molecules are also attracted to the ion, but no more water molecules can be accommodated in the very vicinity of the ion because there is not enough space left. These water molecules are situated next to the water molecules in the first shell around the ion. These molecules form the second shell molecules around ion. In the same way we can distinguish the third, forth, ... shells of solvent molecules around the ion, until the water molecules at a certain distance from the ions do not feel the influence of the ion and behave as water molecules in bulk water phase. All the water molecules that we decide to be distinct from the bulk water molecules form the *hydration shell* around ion, which can be split into *first*, *second*, etc., hydration shells (HSs) according to their distances from the ion. One should note, that the described solvent shells around the ion are not static, but rather mobile structures with not well-defined boundaries. The same formalism can be applied not only to the aqueous solutions, but rather to any solution. In this case we operate with a solvent, and all the characteristics introduced for the hydration process, are transferred to the solvation process (e.g. the term "hydration shell" is changed to the term "solvation shell" (SS), etc.).

A question arises: how to distinguish where the first HS ends and the second starts? The question has no direct answer. One has to introduce some criteria. The most frequently used criteria is to use ion-water radial distribution function (see Section 2.1.1). For condensed systems the ion-solvent RDF has an oscillatory view (see Figure 3). Usually, the boundary for the first SS is chosen to be the position of the first minimum on the RDF, for the second shell from the position of the first minimum to the position of the second minimum on g(r) and so on. In general, one can implement more sophisticated criteria.

2.1.5 Coordination number

Coordination number is an average number of solvent molecules in the first solvation shell of a solute molecule. The coordination number can be calculated from the radial distribution function in the case of a homogeneous liquid. The running coordination number of particles β in the sphere with radius r around a particle α ($n_{\alpha\beta}(r)$) reads:

$$n_{\alpha\beta}(r) = 4\pi\rho_\beta \int_0^\infty g_{\alpha\beta}(r) r^2 dr$$

where $g_{\alpha\beta}(r)$ is the $\alpha - \beta$ radial distribution function, ρ_β is the number density of the particles β in the system.

The coordination number of particles β in the first solvation shell of particles α equals to the value of the running coordination number at the distance equal to the position of the first minimum on the g(r) function. When the solvent is water the *coordination number* is called also as *hydration number*.

2.1.6 Residence time

Residence time of a solvent molecule in *the first solvation shell* of a solute molecule is the mean time one solvent molecule stays within the boundaries of the first solvation shell. The escape of water molecule from the first hydration shell of an ion can be considered as the reaction process:

$$ion - water_n = ion - water_{n-1} + water_1^{bulk}$$

where n is the hydration number of the ion.

The free energy profile along the reaction coordinate of the water escape from the first HS is given by the ion-water PMF. Thus, the activation energy is the difference of the first maximum and the first minimum on the ion-water PMF (see Refs. [95, 96, 97]):

$$E_a = PMF(r_{1^{st}max}) - PMF(r_{1^{st}min})$$

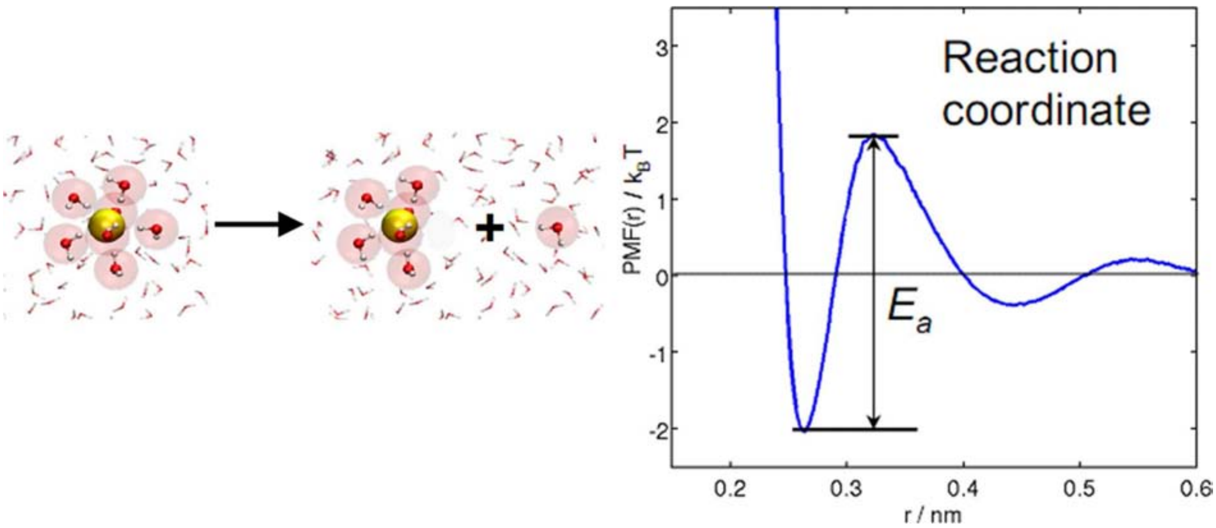

Figure 4: The process of the one water molecule release from the hydration shell of an ion. (left side) Pictorial representation of the process. (right side) The ion-water potential of mean force: the free energy profile of the process. The first barrier on the profile represents the activation free energy of water molecule release from the hydration shell of an ion.

From the kinetic theory (see e.g. [96]) we have the following relation between the residence time and the energetic barrier along the reaction coordinate between initial ($ion - water_n$) and final ($ion - water_{n-1}$) states:

$$\frac{1}{t_R} \propto e^{-\beta E_a}$$

where t_R is the residence time, E_a is the *activation energy* of the process (energetic barrier along the reaction coordinate, see Figure 4).

The conventional way to calculate the residence time is the method proposed by Impey et al. [98]. The residence time is found through fitting the auto correlation function of water molecule escape from the hydration shell of an ion:

$$R(t) = \frac{1}{N_h} \sum_{i=1} N_h \langle \theta_i(0) \cdot \theta_i(t) \rangle$$

with the exponent decay function:

$$exp(-t/t_R)$$

where $\theta_i(t)$ is the Heaviside step function (it equals to 1 if the water molecule i is in the first hydration shell of the ion at time t and to zero otherwise), N_h is the instant coordination number of the ion.

An additional criteria is usually introduced: the absence time $t_{absence}$. If a water molecule, that left the hydration shell, returns back in time less than the absence time then it is assumed that it has not left the hydration shell. This criteria is introduced to get rid of the possible oscillatory motion of the molecules at the boundary of the hydration shell, which are always set "ad-hoc" (see the discussion in the Section 2.1.4). Impey et al. proposed the absence time equal to 2 ps. The most of the authors (see e.g. Ref. [99]) usually provide calculations of the residence time for the two cases: with $t_{absence} = 0$ ps and with $t_{absence} = 2$ ps.

Another way to calculate the residence time is to follow its definition. From the trajectories of the MD simulations one can estimate the average time a water molecule stays within the first hydration shell. This method is very sensitive to the input parameters (e.g. criteria of the boundary of the first hydration shell, etc.).

2.1.7 Samoilov's energy

Samoilov obtained from the experimental data the ratio of the residence times of a water molecule in the HS of an ion and in the HS of a water molecule in the bulk water phase [95]. The ratio is related to the energetic barrier, which is usually referred to the Samoilov's energy ($\Delta E_{Samoilov}$) [95]:

$$\frac{t_R^{sol}}{t_R^0} = e^{-\beta \Delta E_{Samoilov}}$$

where t_R^{sol} and t_R^0 the residence time of a water molecule in the HS of the solute and the residence time of a water molecule in the HS of a water molecule in the bulk water phase, β is the inverse temperature.

The Samoilov's energy can be calculated from the activation energy of one water molecule release from the hydration shell of an ion and activation energy of one water molecule release from the hydration shell of a water molecule in the bulk water phase [96]:

$$\Delta E_{Samoiliov} = E_a^{ion-water} - E_a^{water-water} \tag{10}$$

2.1.8 Positive and negative hydration

According to Samoilov [95], the *hydration* is called *positive* (*negative*) if the residence time of a water molecule in the hydration shell of the solute is *larger* (*smaller*) than the residence time of a water in hydration shell of a water molecule in the bulk solvent. Mathematically it is written as:

$$\begin{cases} t_R^{sol} \geq t_R^0 & \text{corresponds to the "positive hydration",} \\ t_R^{sol} < t_R^0 & \text{corresponds to the "negative hydration".} \end{cases}$$

where t_R^{sol} and t_R^0 are the residence time of a water molecule in the HS of the ion and the residence time of a water molecule in the HS of a water molecule in the bulk water phase [95, 96].

2.1.9 Solvation Free Energy

"*Solvation free energy* is the change in Gibbs energy when [an ion or] molecule is transferred from a vacuum (or the gas phase) to a solvent. The main contributions to the solvation energy come from: (a) the cavitation energy of formation of the hole which preserves the dissolved species in the solvent; (b) the orientation energy of partial orientation of the dipoles; (c) the isotropic interaction energy of electrostatic and dispersion origin; and (d) the anisotropic energy of specific interactions, e.g. hydrogen bonds, donor-acceptor interactions etc." This definition is taken from: IUPAC Compendium of Chemical Terminology 2006 [100].

This quantity characterizes the strength of the solute-solvent interactions, compensated by the entropic terms.

2.2 Asymmetry of ion hydration

2.2.1 Charge overscreening

There is a strong asymmetry of the ions hydration. This term means that hydration characteristics of the imaginary cation and anion of the same size are considerably different. On the Figure 5 one can see the g(r) functions of the water hydrogen and oxygens around a cation and an anion of the same size (the data is adopted from the Ref. [101]). Small positively charged hydrogen sites of water molecules can come much closer to the anion surface rather than bulky oxygen atoms to the cation surface. Both, the charge of the cation and the charge of the anion, are "overscreened" by the partial charges on the water molecules as can be seen from the screening factors on the Figure 5. There is a more strong overscreening of the anion in comparison to the cation, and as a result the electrostatic potentials around the cation and anion dissolved in water are similar (see Figure 5), despite the fact that the charges of these ions are of different sign.

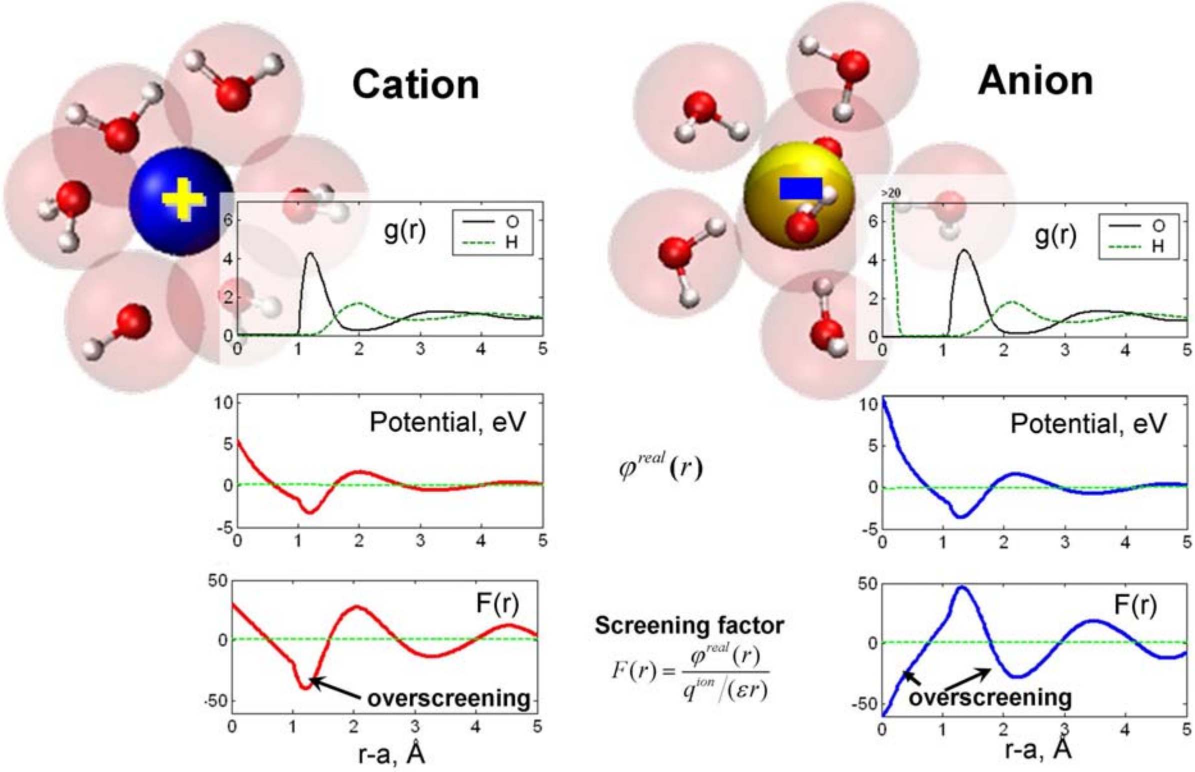

Figure 5: Asymmetry of ion hydration: top) radial distribution functions of water oxygen and hydrogen around the model cation and anion of the same size and charge, middle) the corresponding electrostatic potentials around ions, bottom) the corresponding screening functions. Adopted from the Ref. [101], Copyright ©2007 Taylor & Francis.

2.2.2 Ion hydration thermodynamics

Asymmetry of ion hydration results in the different thermodynamics of ion hydration. Such, the dehydration free energies of cations and anions as a function of ionic radii lay on different curves (Figure 6). The data show that anions are stronger hydrated than cations of the same size. This happens because of the strong interactions of the water hydrogens with the surface of the anions [104].

The entropies of the ion hydration also reveal the asymmetry of ion hydration (see Figure 7). There is a classification of ions, which characterizes ions according to their ability to increase the order of the solvent around them ("order-makers", kosmotropes) or decrease it ("order-

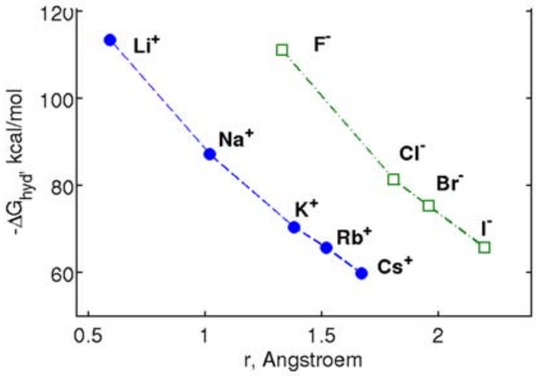

Figure 6: Asymmetry of ion hydration: the ion dehydration free energies ($-\Delta G_{hyd}$). The figure illustrates the data from Ref. [102], the ionic radii are taken from Ref. [103]. For the same size anions are stronger hydrated (the dehydration free energy is bigger) than cations.

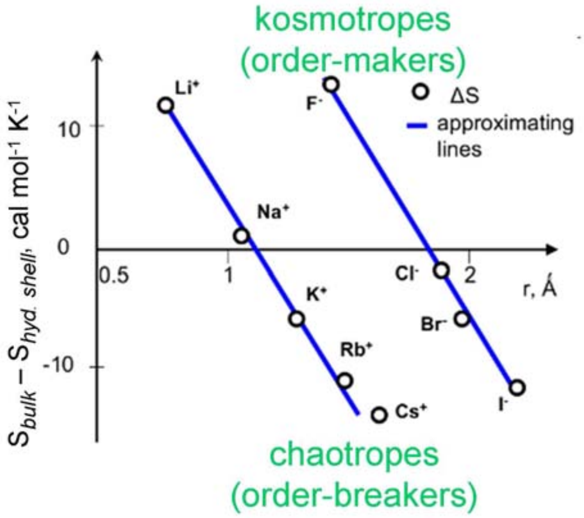

Figure 7: Asymmetry of ion hydration: ion hydration excess entropies [105] (adaptation of data of Krestov as presented by Samoilov (see Ref. [106])). The ions can be classified in two groups: kosmotropes and chaotropes. The kosmotropes increase the order of the water around them, i.e. decrease the entropy of the water molecules compared to the bulk water phase. The chaotropes decrease the order (increase the entropy) of the water molecules around them.

breakers", chaotropes) [105]. A convenient quantity, which can quantify this property, is *the ion hydration excess entropy* (see Figure 7). The ion hydration excess entropy shows the difference between the entropy of water molecules in the bulk water phase and water molecules in the HS of an ion (see Ref. [105]).

2.3 Ion direct contact formation in solution

2.3.1 General scheme

Collins et al. analyzed the process of the ion direct contact formation, and how this depends on the hydration characteristics of the single ions [105]. In the article describing the probability of the ion direct contact formation authors discuss the interplay of the ion-ion, ion-water and water-water interactions [105]. In this section inspired by the mentioned discussions we develop a general scheme of the ion direct contact formation in aqueous solutions. The general scheme is represented on the Figure 8.

Formally, the process of ion direct contact formation in a solution can be decomposed into three steps. Firstly, the partial dehydration of ions have to occur, when two ions make a direct contact. The contacting ions release some water molecules from their hydration shells. The energy cost of this process is usually referred to the *penalty for partial dehydration*. The stronger the interaction of the dissolved ions with water the larger is the penalty for their partial dehydration. Thus, formally we may say that the process of the partial dehydration is determined by the strength of the ion-water interactions.

Secondly, making a direct contact the ions interact with each other. The potential between ions contributes to the energetic changes upon the ion direct contact formation. Thus, this part represents the impact of the ion-ion interactions on the process.

Thirdly, the released solvent molecules must be hydrated in the bulk water phase. Energetic gain of this process depends on the strength of water-water interactions.

The described scheme is not perfect by any means but it brings a picture "how to think about" the phenomena of the solvent mediated interactions in solutions. One has to be careful in more tiny details, like solvent reorganization in the solvation shells of ions upon the ion direct contact formation, which is not rigorously captured by the described scheme.

The main conclusion from the above described statements is that the process of the ion direct contact formation in solution is determined by the interplay of the ion-ion, ion-water and water-water interactions. We believe that the described scheme can be extended to more complicated systems: particle interactions with different surfaces mediated by a solvent, which can be many component. Adjusting the interaction between the species (varying the chemical nature of the components) one can obtain different effects: like, preferential adsorption or depletion of particles to/from the surface, etc.

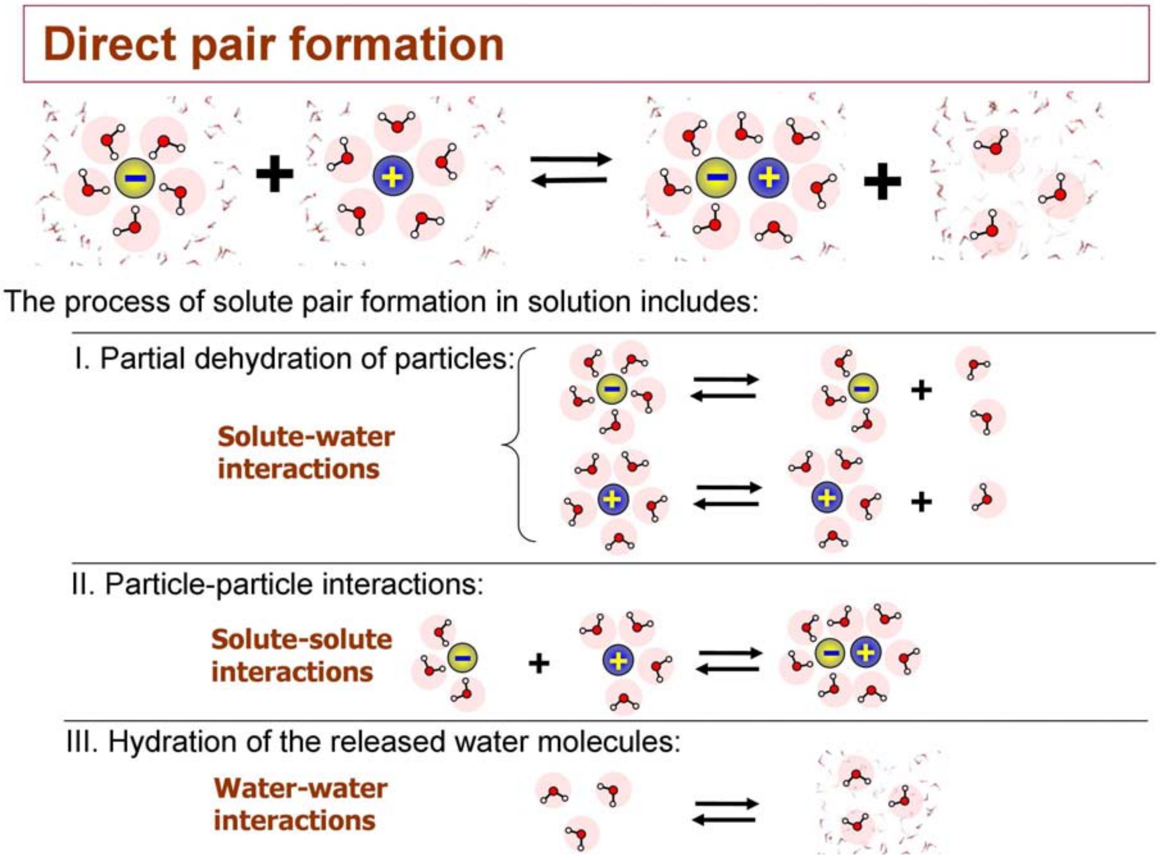

Figure 8: The mechanism of the ion direct contact formation in aqueous solutions. The process can be formally decomposed into three steps: 1) partial dehydration of the ions, 2) direct interaction of the ions, 3) hydration of the released water molecules.

2.3.2 Collins pyramid: the "law of matching water affinities"

The Collins pyramid [105] represents the principle "like likes like" [107]. The principle tells that the probability to form an ion-ion direct contact in a solution is bigger for ions of similar sizes, and smaller for ions of different sizes. This principle is a consequence of the interplay of the ion-ion, ion-water and water-water interactions [105], discussed in the Figure 8. Indeed, if an ion is big then it has a low surface charge density and, thus, it weakly interacts with the water molecules. The strength of the water-water interactions exceeds the the strength of the ion interactions with water, in this case the absolute value of the ion hydration enthalpy is low. Next, if there is a big counterion in the solution, then following the same statements, we may conclude that the absolute value of its hydration enthalpy also would be low. Thus, the case of the big ion - big counterion a corresponds to the region close to zero on the X-axis of the Collins "volcano" plot (see Figure 9a). Because the strength of the water-water interactions is stronger than the ion-water interactions for both the big ion and the big counterion, the ions will

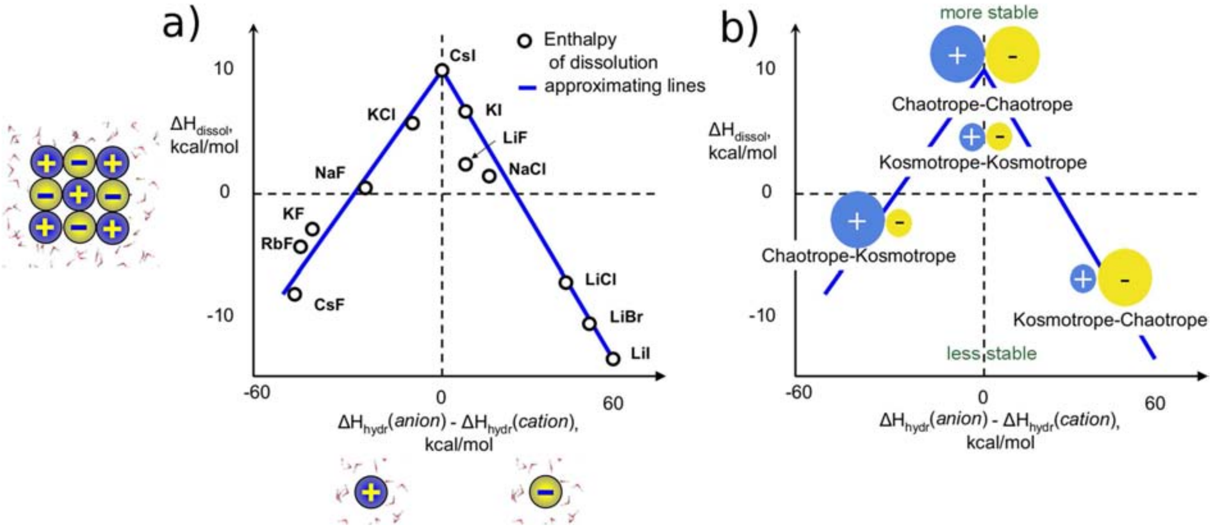

Figure 9: Collins "volcano" plots. a) The dependence of the salt dissolution enthalpy (ΔH_{dissol}) and the difference between the enthalpies of hydrations of anions and cations for different alkali halide salts. b) the same in the view of chaotropic and kosmotropic ions (please see the Ref. [105]). Adaptation of the data presented in Ref. [105]. Please, see the text (Section 2.3.2) for more details.

be "pushed" to form the direct contact to allow more water molecules interact with other water molecules, rather than with the ions. Thus, the probability of the big ion - big counterion direct contact will be high, and this reflects in the positive dissolution enthalpy (endothermic process) of the salt formed by these ions. The case of the big ion - big counterion would fall on the top of the Collins pyramid (see Figure 9).

The case of the small ion - small counterion also falls on the top of the Collins pyramid, because the strength of the ion-water interactions is not large enough to compete with strong electrostatic attraction between the small ions with the high surface charge densities. In this case the probability of the ion direct contact would also be high and the single ion hydration enthalpies would be of the same order of magnitude (there difference will be close to zero).

The cases of the small ion - big counterion fall on the foot o the "volcano" plot. In these cases the strength of the ion-water interactions will be high for the small ion and low for the big ion. As a result the hydration enthalpy of the small ion will be higher in absolute value than the hydration enthalpy of the big ion and, thus, the corresponding point will be either on the right hand side or the left hand side on the "volcano" plot. The strong small ion - water interactions will prevent the partial dehydration of the small ion and as the result the small ion will stay in the solution. Thus, the big counterion would also have to be in the solution. As a result the ions will stay apart from each other in the solution (the probability of the direct contact will be low). Due to the differences of the ion sizes the salt crystal formed by these ions would be not as stable as in the case of the ions with similar ionic radii. This is reflected in the negative salt dissolution enthalpies for the salts formed by the ions of considerably different radii (see the Figure 9).

3 Modelling approach

3.1 Molecular Dynamics simulation

In this section we describe the Molecular Dynamics technique. The information is interpreted from the books of Frenkel, Smit [108] and Allen, Tildesley [109].

Molecular Dynamics simulation is a technique for computing the equilibrium and transport properties of a mechanic N-particle system, where the dynamics of the particles obey the laws of classical mechanics. We integrate the equations of particles motion where the Lagrangian depends on the positions of all the particles in the system. As a result, we obtain coordinates, velocities and accelerations for each particle in the system as functions of time. Applying statistical mechanics we can determine thermodynamic and dynamic properties of this system.

Classical mechanics is an appropriate approximation for a wide range of systems. Only when we consider the translational or rotational motion of light atoms or molecules (He, H_2, D_2) or vibrational motion with a high frequencies ν, so that $h\nu > k_BT$, should we worry about quantum effects.

In classical mechanics the Lagrangian of the mechanical system is written as:

$$L(x, \dot{x}, t) = \sum_{i=1}^{3N} \tfrac{1}{2} m_i \dot{x}_i^2 - U(x, t)$$

where U is the potential energy of the system, x_i is the spatial coordinate of a particle in the system, N is the number of particles in the system, $x = \{x_1, ..., x_{3N}\}$ is the vector of all the particle coordinates in the system (each particle has three spatial coordinates, since we work in 3D space), $\dot{x}_i$ is the velocity vector component, $\dot{x}$ is the vector of all particle velocity components in the system, m_i is the mass of the particle which has x_i spatial coordinate, t is time.

The equations of particle motion can be written as:

$$\frac{d}{dt}\frac{\partial L}{\partial \dot{x}_i} - \frac{\partial L}{\partial x_i} = 0, \quad (i = 1, ..., 3N)$$

or equivalently as:

$$\begin{cases} m_1 \ddot{x}_1 = -\frac{\partial U(x_1, x_2, ..., x_{3N})}{\partial x_1}, \\ m_2 \ddot{x}_2 = -\frac{\partial U(x_1, x_2, ..., x_{3N})}{\partial x_2}, \\ \ldots\ldots\ldots\ldots\ldots\ldots\ldots\ldots \\ m_{3N} \ddot{x}_{3N} = -\frac{\partial U(x_1, x_2, ..., x_{3N}).}{\partial x_{3N}} \end{cases} \tag{11}$$

where $-\frac{\partial U(x_1, x_2, ..., x_{3N})}{\partial x_i} = F_i$ is the force vector component acting on the particle with x_i spatial coordinate, $\ddot{x}_i$ is the acceleration vector component.

In molecular dynamics we solve the equations of motion (Equation 11). As a result we obtain $x(t)$, $\dot{x}(t)$ that are sufficient for the full mechanical description of the mechanical system.

The system of the equations of motion does not have an analytical solution for the number of particles more than two. This is a well-known "many body problem". That is why one has to solve this with some numerical integrators. Nowadays, efficient algorithms and computer facilities allow one to solve the equation of motions with the number of particles of about $N = 10^4 - 10^5$ and number of iterations for sufficient statistics of about $10^6 - 10^9$.

3.2 Integration schemes

In this section we describe different schemes to solve the equation of motions (Equation 11) of the mechanical system numerically. The numerical method to solve the equations is called an *integrator*. To derive integrators, let us write the Taylor expansion of coordinate with respect to time [108]:

$$x_i(t + \Delta t) = x_i(t) + \dot{x}_i(t)\Delta t + \frac{\ddot{x}(t)}{2}\Delta t^2 + \frac{\dddot{x}}{3!}\Delta t^3 + \frac{\ddddot{x}}{4!}\Delta t^4 + ... \tag{12}$$

The simplest integrator is the Euler type scheme. It uses only 3 terms in this expansion. More rational integrators are the Verlet integrator and its derivatives. These integrator exploit 4 terms. All others integrators are called *higher − order* algorithms.

There are several criteria which are crucial for characterization of the integrator schemes. An integration scheme should be:

1. Time-reversible. Newton equations are time-reversible, and that is why integrator should obey this condition. Such integrators are more stable.
2. Stable for large timesteps (iteration steps). Larger timesteps allow a mechanical system to sample the phase space with less amount of iterations.
3. Preserving the constants of motion. Depending on statistical ensemble during integration different values should remain constant (total energy, temperature, etc.)
4. Area-preserving. The integrator should leave the magnitude of any volume element in phase space unchanged [108].

3.2.1 Verlet integrator

The most appropriate choice of the integration scheme for MD simulations is the Verlet integrator and its derivatives [108], because it is time-reversible, good for long-time conservation of constants of motion, area-preserving and allows relatively big timesteps.

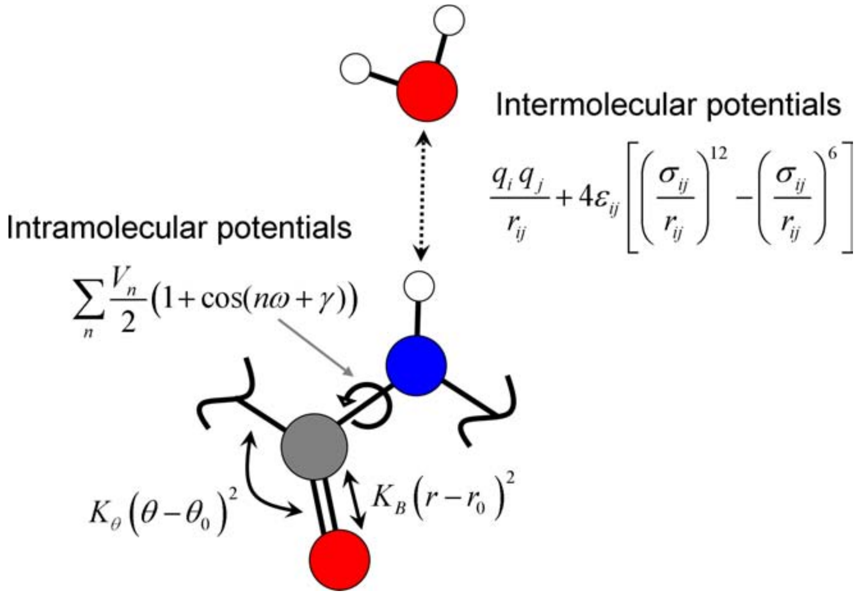

Figure 10: Representation of the inter- and intra-molecular interactions in a usual molecular dynamics simulation. The figure is adopted from Reference [110]. See the text for more details.

To derive the Verlet integrator we write the Taylor expansion of a particle coordinate around the time similar to Equation 12, but with the negative Δt:

$$x_i(t-\Delta t) = x_i(t) - \dot{x}_i(t)\Delta t - \frac{\ddot{x}(t)}{2}\Delta t^2 - \frac{\dddot{x}}{3!}\Delta t^3 - \frac{\ddddot{x}}{4!}\Delta t^4 + ... \tag{13}$$

Summing up the two equations 12 and 13 we get:

$$x(t+\Delta t) = 2x(t) - x(t-\Delta t) + \ddot{x}(t)\cdot\Delta t^2 + O(\Delta t^4) \tag{14}$$

where $\ddot{x}(t) = \frac{F(t)}{m}$.

Thus, with the Verlet integration scheme we can estimate the new positions of particles in the next time step with the error proportional only to the Δt^4 term.

3.3 Force calculation

The most part of computer resources in MD simulations (about 95%) is consumed by force calculations [108]. Forces are obtained directly from the potential energy by its partial differentiation:

$$-\frac{\partial U(x_1, x_2, ..., x_{3N})}{\partial x_i} = F_i$$

Let us describe the potential energy calculation in MD. Molecular interactions considered in the MD calculation have electrostatic origin (interaction of electrons and nuclei). To evaluate the potential energy in general case we need to solve the Shrödinger equation for huge number of particles, which makes it unfeasible to calculate. That is why in most of computer simulation of liquids the molecular interactions are approximated by some effective terms. In classical Molecular Dynamics simulation molecules are split into atomic sites, interacting with each other through effective potentials (see Figure 10). The collection of effective parameters for each atomic site is called *a Force Field*. Thus, by introducing atomic sites instead of the number of nuclei and electrons we reduce dramatically the number of degrees of freedom in the system and can avoid dealing with objects of quantum nature. The effective parameters for the interatomic potential should be parameterized by fitting against experimental data or high level quantum chemistry calculations.

Molecular interactions are classified into intramolecular ("bonded") and intermolecular ("non-bonded") interactions, and thus the potential energy of the system can be written as:

$$U = U_{bon} + U_{nb}$$

where U_{bon} and U_{nb} are the potential energies of all the bondeed and nonbonded interactions respectively.

Intra-molecular interactions are the interactions between the atoms in the same molecule which are separated usually by no more than three covalent bonds. Usually, the intermolecular potentials in the molecule are approximated by *stretching*, *bending* and *dihedral* terms (see Figure 10). For the neighbor atoms a stretching term is introduced, which is usually represented by a harmonic potential, which restraints the deviation of the bond length to its equilibrium value. For three atoms belonging to the two neighboring covalent bonds a *bending* potential is introduced, usually it is also harmonic, which restraints the angle between the two covalent bonds to its equilibrium value. The *dihedral* potential determines the rotation of the two molecular groups around a bond. This is usually represented via Fourier series. The intramolecular potential energy of the system is written as:

$$U_{bon} = \sum_{N_{bonds}} k_b (r - r_0)^2 + \sum_{N_{angles}} k_\theta (\theta - \theta_0)^2 + \sum_{N_{dihedrals}} \sum_{n} \frac{V_n}{2} (1 + \cos(n\phi + \gamma))$$

where k_b and k_θ are the stretching and bending force constant s, r_0 and θ_0 are the equilibrium values of the bond length and angle respectively, V_n are the Fourier series coefficients, γ is the cosine phase: all these parameters are empirical parameters which one has to parameterize.

The intermolecular interactions are usually subdivided into Van-der-Waals interaction and Coulomb interaction of partial charges on atoms. The Van der Walls interactions are usually represented by the so-called atom-atom Lennard-Jones (LJ) potential. Thus, the potential energy of all the nonbonded interactions reads:

$$U_{nb} = \sum_{N_{nb}} \left\{ 4\varepsilon_{ij} \left[\left(\frac{\sigma_{ij}}{r_{ij}} \right)^{12} - \left(\frac{\sigma_{ij}}{r_{ij}} \right)^{6} \right] + \frac{q_i q_j}{r_{ij}} \right\}$$

where ε_{ij} and σ_{ij} are the LJ potential parameters, and q_i and q_j are the partial charges, r_{ij} is the distance between the particular atoms i and j.

In MD simulation the intermolecular interaction usually are approximated to be pair-wise additive. This results into the fact that the complexity of the energy calculation of the system containing N particles is proportional to N^2.

The Lennard-Jones potential decays very quickly with the increase of the inter-particle distance (proportional to the r^{-6}), usually it is classified as *short-range* interaction. Thus, evaluation of the short-range interaction is necessary to do only for small distances between particles. Therefore without loss of accuracy in MD simulations one usually introduces the cutoff distance (R_{cut}) for the LJ potentials. This allows to model relatively small systems size, because the molecules "feel" each other only for short distances.

In turn, the Coulomb term decays slowly (proportional to as r^{-1}), thus it is considered to be a *long-range* interaction. And thus the use of simple cutoff technique would lead to serious artifacts. This will be discussed in the section Section 3.6 in more detail.

3.4 Periodic boundary condition

Usually, for chemical applications one needs to calculate the properties of a bulk solution (e.g. a protein dissolved in water). This implies regarding the large number of molecules in the system, which comprise the bulk solution. If we set initial coordinates of our molecules (feasible number of $10^4 - 10^5$) in a cubic simulation box, a lot of molecules would be situated at the boundary of the box. Without any corrections this will lead to not correct representation of the bulk solution properties, because the properties of the molecules close to the surface are different from the properties of molecules in the bulk solution. One way to overcome the problem is to increase the box size, which would increase the number of molecules, and as well the computation consumptions dramatically. Another way is to use the Periodic Boundary Conditions (PBC), which allows to model the bulk solution properties, without introducing the large number of molecules. The PBC technique works in the following way. We create 26 images of the initial box (see Figure 11). Particles in image boxes "copy" the motion of the initial particles. If during the MD integration any particle crosses the initial box boundary, the corresponding image molecule from the image box with the same momentum enters the initial box through the

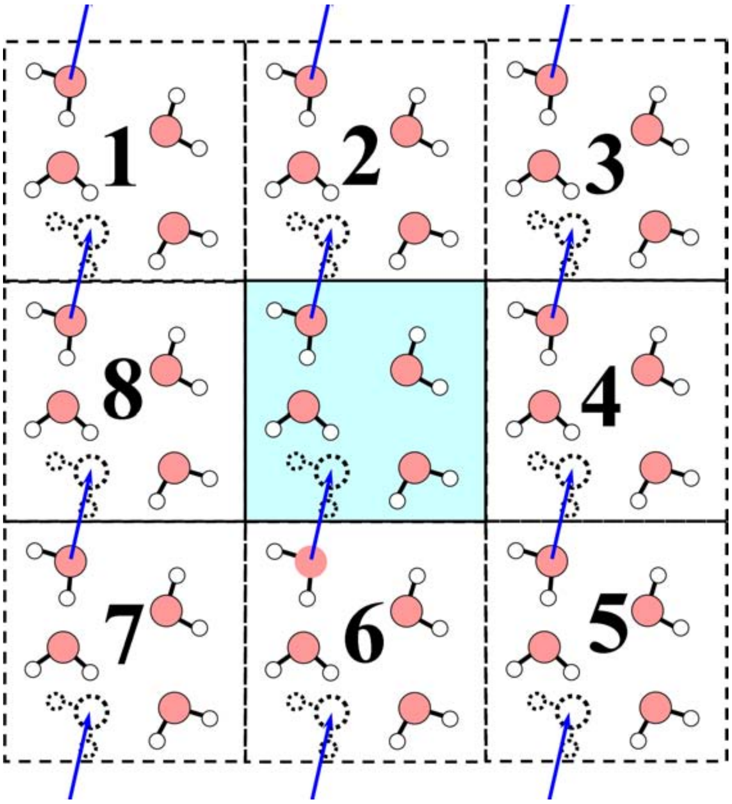

Figure 11: Schematic representation of the cubic periodic boundary conditions. The initial box is marked by the blue color. The image boxes are marked by the digits (mind, in the 3D space there are 26 images). The blue arrows represent the direction of the particle motion. The figure is adopted from the Ref. [109].

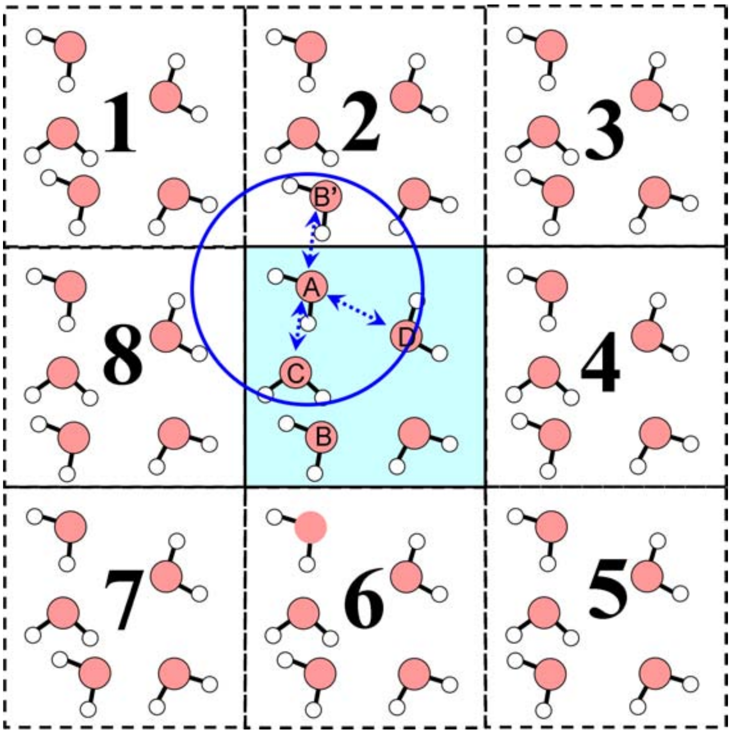

Figure 12: Schematic representation of the intermolecular interactions with the periodic boundary conditions. The blue circle represents the cutoff boundary of the for the short-range interactions. The figure is adopted from Ref. [109].

opposite side. The physical picture of this would be that the simulation box is "closed to itself". The number of particles remains constant.

PBC works also for the energy and force calculations for particle interacting via the short-range potentials (see Figure 12). For example, particle A interacts with particles C and D directly in the simulation box, but with the particle B it interacts through the boundaries of the box (it interacts with the image of the B particle - B', see the Figure 12).

3.5 Short-range interactions (Cell lists)

There are some techniques to simplify the calculation of the short-range potential terms between the particles in the system. One of the most effective is the "Cell lists" technique [108]. In this method we divide the initial box into smaller cells with edge length slightly greater than R_{cut} distance. We need to evaluate the short-range interaction between particles where the interparticle distance is less than the R_{cut} threshold. Thus, for a given cell only particles that are inside the cell and all the particles in the nearest 26 cells are of potential interest for the short-range interactions. Interactions with the particles situated in other cells can be neglected, and thus this reduces the computational consumptions. For a particular time step we can store the data on which atoms are interacting with which into a list (the "cell list"), and then use the same list for several subsequent integration time steps, this decreases the computational consumptions further. Note, that in this case the cell lists would work only if the edge length of the cells is larger then the R_{cut}. The time saving also results from the fact that we need to reevaluate the lists only if a particle being not in the list enters the cutoff region of another particle. The procedure of determining to which cell particles belong has $O(N)$ complexity. Thus, for a large system the cell lists method reduces the complexity of the evaluation of the short-range interactions from $O(N^2)$ to $O(N)$.

3.6 Long-range interactions

It is appropriate to use truncation radius technique only for short range potentials. The energy we neglect in this case is written as the following:

$$U_{tail} = \frac{N\rho}{2} \int_{R_{cut}}^{\infty} dr \cdot u(r) 4\pi r^2$$

where ρ is the number density, N is the number of particles. This equation shows that the neglected energy diverges, unless the potential energy function $u(r)$ decays faster than r^{-3} [108]. That is why we cannot use the simple truncation for the Coulomb potential.

3.7 Ewald summation method

One of the most popular techniques to calculate electrostatic energy in the MD simulations is the Ewald summation method [108]. Let us consider a system of point charges being infinitively replicated in all three directions (see Figure 13). We make an assumption that our liquid has the structure like crystal structure with our cubic cell being the unit cell of the lattice.

In the Ewald summation method we calculate the potential energy of the electrostatic interactions between our simulation box and its infinite lattice of replicas. This way we can capture the effect of the long-range Coulomb interactions on the molecules in the unit cell. This construction is just a model, therefore it can course artifacts.

The Coulomb energy of the system is a product of the charge and the potential at the certain point in space, with further summation over all charges in the simulation box:

$$U_{coul} = \tfrac{1}{2} \sum_{i=1}^{N} q_i \phi(r_i)$$

where $\phi(r)$ is the electrostatic potential at the point $\mathbf{r}_i$, q_i is the electrostatic charge on the particle i. The electrostatic potential comprises the potential created by all the charges in the

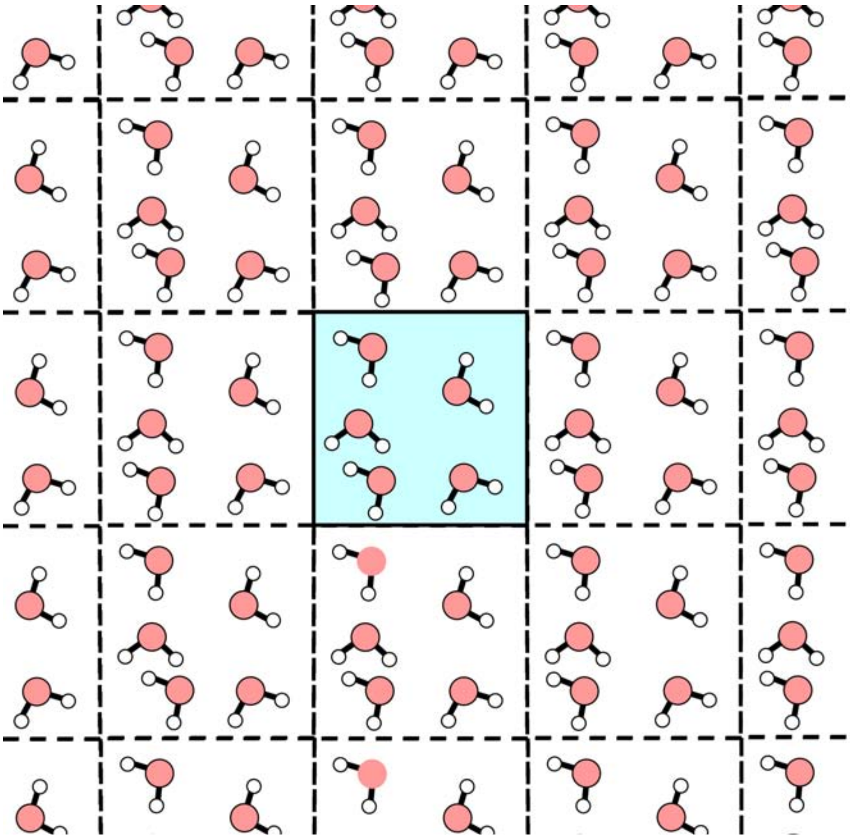

Figure 13: Infinite lattice approximation in the Ewald summation method.

infinite lattice:

$$\phi(r_i) = \sum_{n}^{\prime} \sum_{j=1}^{N} \frac{q_j}{\left| r_{ij} + nL \right|} \tag{15}$$

where n is the lattice vector responsible for the determination of a cell out of the infinite lattice, L is the unit box length, apostrophe on the summation sign means that one should sum over all the pairs $i - j$ except the pairs where i equals j and $n = 0, 0, 0$ (the initial simulation box).

This sum in Equation 15 is only conditionally-convergent [108]. To improve the convergence of this sum and not to evaluate all the pair interactions over the infinite lattice, it is possible to do the following trick: we divide the Coulomb potential into a fast decaying part (short-range) for small r and a gradually decaying (long-range) for large r:

$$\frac{1}{r} = \frac{f(r)}{r} + \frac{1 - f(r)}{r}$$

where the $f(r)$ is the "smearing" function.

In this case we can estimate the electrostatic energy coming from the short-range part using the usual cutoff scheme for the short-range interactions. The gradually decaying (long-range) term can be efficiently treated in the reciprocal (Fourier) space, where it can be represented by a small number of k-vectors.

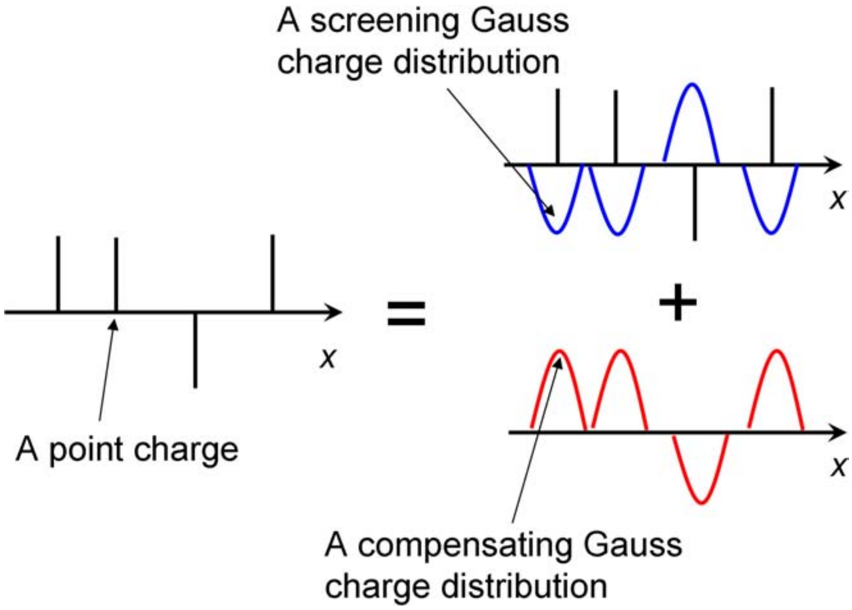

Figure 14: Pictorial representation of the decomposition of the charge density of the infinite lattice in the Ewald summation method into short-range and long-range parts. Figure is adopted from the Ref. [108].

The most often choice of the "smearing" function is the complementary error function:

$$erfc(r) = \frac{2}{\sqrt{\pi}} \int_r^{\infty} dt \cdot \exp(-t^2)$$

Let us look at the Ewald summation procedure from another "side". It turns out that introducing of the complementary error function is analogous to the following presentation of electron density of the system (see Figure 14):

- for each point charge in the system we assign a screening Gauss charge distribution of the opposite sign, which screens the initial charge.
- we introduce the same charge distribution but of the opposite sign to compensate the changes.

3.7.1 Real space Ewald sum

To prove the above statement, let us show that the point charge screened by the Gauss distribution of the opposite charge produces the electrostatic potential of the form $\frac{erfc(r)}{r}$.

The Gauss charge distribution reads:

$$\rho_{Gauss}(r) = -q_i \left(\frac{\alpha}{\pi}\right)^{\frac{3}{2}} \exp\left(-\alpha r^2\right) \tag{16}$$

where α is a numeric parameter.

The electrostatic potential produced by the Gauss charge distribution can be obtained by solving the Poisson equation:

$$-\nabla^2 \phi_{Gauss}(r) = 4\pi\rho_{Gauss}(r) \tag{17}$$

Due to the spherical symmetry of the Gauss distribution we can rewrite this equation as follows [108]:

$$-\frac{1}{r}\frac{\partial^2 r\phi_{Gauss}(r)}{\partial r^2} = 4\pi\rho_{Gauss}(r) \tag{18}$$

Analytical integration of the equation 18 gives: (first, we put r under the differential and then we take the integral of the Gauss distribution, the limits of the integration are taken to cancel the free term after the integration)

$$\begin{aligned}
-\frac{\partial r\phi_{Gauss}(r)}{\partial r} &= -4\pi q_i \left(\frac{\alpha}{\pi}\right)^{\frac{3}{2}} \int_{\infty}^{r} dr \cdot r \cdot \exp(-\alpha r^2) \\
&= 2q_i \frac{\alpha^{\frac{3}{2}}}{\pi^{\frac{1}{2}}} \int_{r}^{\infty} dr^2 \cdot \exp(-\alpha r^2) \\
&= 2q_i \left(\frac{\alpha}{\pi}\right)^{\frac{1}{2}} \exp(-\alpha r^2)
\end{aligned}$$

The second integration gives the error function:

$$\begin{aligned}
r\phi_{Gauss}(r) &= -2q_i \left(\frac{\alpha}{\pi}\right)^{\frac{1}{2}} \int_{0}^{r} dr \cdot \exp(-\alpha r^2) \\
\phi_{Gauss}(r) &= -\frac{q_i}{r} erf\left(\sqrt{\alpha} r\right)
\end{aligned} \tag{19}$$

where

$$erf(x) \equiv \frac{2}{\sqrt{\pi}} \int_0^x \exp(-u^2) du$$

is the error function.

Thus, the electrostatic potential originated from the point charge screened by a compensating Gauss charge distribution is written as the following:

$$\phi(r) = \frac{q_i}{r} - \frac{q_i}{r} erf(\sqrt{\alpha} r_{ij}) = \frac{q_i}{r} erfc(\sqrt{\alpha} r_{ij}) \tag{20}$$

The statement is proven.

This potential decays rapidly, it becomes short range. Thus, we can write the real space Ewald sum as follows:

$$U_{Ewald-real} = \frac{1}{2} \sum_{m}{}' \sum_{i,j=1}^{N} \frac{q_i q_j}{\left|r_{ij} + mL\right|} erfc(\sqrt{\alpha}\left|r_{ij} + mL\right|) \tag{21}$$

where the first sum is performed over only the nearest images of the initial cell. Their number is determined by the α parameter. The complexity to evaluate this term is proportional to $O(N)$.

3.7.2 Reciprocal space Ewald sum

To complete the Ewald summation technique we need to evaluate the contribution of the compensating charge density into the electrostatic energy of the system:

$$\rho(r) = \sum_{n} \sum_{j=1}^{N} q_j \left(\frac{\alpha}{\pi}\right)^{\frac{3}{2}} \exp\left(-\alpha \left|r - (r_j + nL)\right|^2\right) \tag{22}$$

The Poisson equation can be written in the Fourier space as follows [108]:

$$k^2 \tilde{\phi}(k) = 4\pi \tilde{\rho}(k)$$

where ∼ indicates the Fourier transformation of the corresponding function.

Let us obtain the Fourier transform of the charge density:

$$\begin{aligned}
\tilde{\rho}(k) &= \int_V dr \cdot \exp(-ikr)\rho(r) \\
&= \int_V dr \cdot \exp(-ikr) \textstyle\sum_n \sum_{j=1}^{N} q_j \left(\frac{\alpha}{\pi}\right)^{\frac{3}{2}} \exp\left(-\alpha \left|r - (r_j + nL)\right|^2\right) \\
&= \int_V dr \cdot \exp(-ikr) \textstyle\sum_{j=1}^{N} q_j \left(\frac{\alpha}{\pi}\right)^{\frac{3}{2}} \exp\left(-\alpha \left|r - r_j\right|^2\right) \\
&= \textstyle\sum_{j=1}^{N} q_j \exp(-ikr_j) \cdot \exp\left(-k^2 \middle/ 4\alpha\right)
\end{aligned}$$

Then Poisson equation for this charge density in Fourier space is:

$$\tilde{\phi}(k) = \frac{4\pi}{k^2} \sum_{j=1}^{N} q_j \exp(-ikr_j) \cdot \exp\left(-k^2 \middle/ 4\alpha\right)$$

This expression exists only if k is not equal to 0.

Now we can write the potential in the real space by applying the inverse Fourier transform:

$$\begin{aligned}
\phi(r) &= \frac{1}{V} \textstyle\sum_{k \neq 0} \tilde{\phi}(k) \exp(ikr) \\
&= \frac{1}{V} \textstyle\sum_{k \neq 0} \sum_{j=1}^{N} \frac{4\pi q_j}{k^2} \exp\left(ik\left[r - r_j\right]\right) \cdot \exp\left(-k^2 \middle/ 4\alpha\right)
\end{aligned}$$

The electrostatic energy resulting from the charge distribution can be found as a product of the charges and the potential:

$$U_{reciprocal} = \frac{1}{V} \sum_{k \neq 0} \sum_{i,j=1}^{N} \frac{4\pi q_j q_i}{k^2} \exp\left(ik\left[r_i - r_j\right]\right) \cdot \exp\left(-k^2 \middle/ 4\alpha\right)$$

$$U_{reciprocal} = \frac{1}{2V} \sum_{k \neq 0} \frac{4\pi}{k^2} \left|S(k)\right|^2 \cdot \exp\left(-k^2 \middle/ 4\alpha\right) \tag{23}$$

where $S(k)$ is the corresponding structure factor.

The structure factor is:

$$S(k) \equiv \sum_{i=1}^{N} q_i \exp(ikr_i) \tag{24}$$

Evaluation of the expression (Equation 23) still has the complexity of $O(N^2)$. But here N is a number of charges in the initial cell, rather than the infinite number of charges in the infinite lattice, though the energy is computed for the infinite periodic lattice. This energy contains an artificial term. When we calculated the real space Ewald sum we excluded the interactions of a charge with itself and with its screening Gauss distribution. Here in the compensation distribution, we have not excluded them in order to save the charge density function to be periodic and smooth, because we needed to perform the Fourier transformation. Now we should exclude this spurious term.

The electrostatic potential due to Gauss distribution is given in the Equation 19. The spurious term originates from the interaction of the point charge and the Gauss distribution. As the charge is situated in the center of the Gaussian distribution, we should determine the potential created by the this Gauss charge distribution at this point:

$$\begin{aligned}
\phi_{Gauss}(0) &= \tfrac{2}{\sqrt{\pi}} q_i \lim_{r\to 0} \tfrac{1}{r} \int_0^{\sqrt{\alpha}r} \exp(-u^2)du \left(\tfrac{0}{0}\right) \\
&= \tfrac{2}{\sqrt{\pi}} q_i \lim_{r\to 0} \tfrac{d}{dr} \int_0^{\sqrt{\alpha}r} \exp(-u^2)du \\
& \boxed{\begin{array}{lcl} t = \sqrt{\alpha}r & \rightarrow & dt = \sqrt{\alpha}dr \\ r \rightarrow 0 & \rightarrow & t \rightarrow 0 \end{array}} \\
&= \tfrac{2q_i\sqrt{\alpha}}{\sqrt{\pi}} \lim_{t\to 0} \tfrac{d}{dt} \int_0^{t} \exp(-u^2)du \\
&= \tfrac{2q_i\sqrt{\alpha}}{\sqrt{\pi}} \lim_{t\to 0} \exp\left(-t^2\right) \\
&= \frac{2q_i\sqrt{\alpha}}{\sqrt{\pi}}
\end{aligned}$$

Thus, the artificial energy term reads:

$$U_{artificial} = \frac{1}{2}\sum_{i=1}^{N} q_i \phi(r_i) = \frac{\sqrt{\alpha}}{\sqrt{\pi}} \sum_{i=1}^{N} q_i^2$$

This can be evaluated once at the very beginning of the simulation.

3.7.3 Ewald summation summary

Summary energy of point charges in the simulation box estimated by the Ewald summation reads:

$$U_{Coul} = \tfrac{1}{2} \sum_{m}{}^{\prime} \sum_{i,j=1}^{N} \frac{q_i q_j}{\left|r_{ij} + mL\right|} erfc(\sqrt{\alpha}\left|r_{ij} + mL\right|)$$

$$+ \frac{1}{2V} \sum_{k\neq 0} \frac{4\pi}{k^2} \left|S(k)\right|^2 \cdot \exp\left(-k^2 / 4\alpha\right)$$

$$-\sqrt{\frac{\alpha}{\pi}}\sum_{i=1}^{N} q_i^2 \tag{25}$$

The forces can be computed analytically from the potential energy functions [108] (see Equation 25):

$$\begin{aligned} F_i = q_i \textstyle\sum_{i,j=1}^{N} q_j \sum_m' \left(2\sqrt{\frac{\alpha}{\pi}}\exp\left(-\alpha\left|r_{ij}+mL\right|^2\right)+\frac{erfc(\sqrt{\alpha}|r_{ij}+mL|)}{|r_{ij}+mL|}\right)\frac{r_{ij}+mL}{|r_{ij}+mL|^2} \\ +\frac{q_i}{V}\textstyle\sum_j q_j \sum_{k\neq 0}\frac{4\pi k}{k^2}\left|S(k)\right|^2\cdot\exp\left(-k^2/4\alpha\right)\cdot\sin(kr_{ij}) \end{aligned} \tag{26}$$

The artificial term has no contribution to the forces.

Optimizing the value of the parameter α, the complexity of the Ewald summation can be reduced to be $O(N^{3/2})$. The parameter α determines the balance between the number of vectors in the real and reciprocal sums. Usually, the real space sum is limited by truncation radius of Lennard-Jones interactions, so in this case the main computation consumptions come from the evaluation of the reciprocal sum. Thus, to speed up the MD simulations we at first should exploit methods for efficient estimation of the electrostatic interactions in the reciprocal Ewald sum.

3.8 Mesh Ewald methods

There exist an procedure to perform Fourier Transformation efficiently - the Fast Fourier Transform (FFT), which scales as $O(N \cdot logN)$ [111, 112]. To employ FFT the charge density distribution should be discretized on a uniform mesh. The most known mesh methods are the particle mesh Ewald (PME)[113], smooth particle mesh Ewald (SPME) [112] and particle-particle particle-mesh Ewald (PPPM) (please see the references in Ref. [114]). The evaluation of the reciprocal Ewald sum using the FFT procedure comprises the following steps [115, 116]:

1. Creation of a uniform mesh in 3D space
2. Assignment (interpolation) of the charge distribution onto the mesh knots
3. Calculation of the Fourier transformation of the "mesh" charge density using the FFT procedure
4. Solution of the Poisson equation in the Fourier space
5. Transformation back to the real space. Force evaluation
6. Force assignment via the back interpolation of determined forces from the mesh knots onto positions of the point charges in the system

Let us describe the procedure of the charge assignment onto the mesh knots for the one dimensional case. Let us create the mesh with points $x_p (p = 0, N_M - 1)$. We define the charge assignment function $W(x)$, so that $W(x - x_p)$ is a part of an unit charge with x coordinate, which will be assigned onto the mesh point with x_p coordinate. Thus, the mesh charge density we obtain by convolution of the true charge density and the charge assignment function:

$$\rho_M(x_p) = \frac{1}{h} \int_0^L dx \cdot W(x - x_p) \rho(x)$$

where L is the simulation box length, $h = L/N_M$ is the distance between mesh points.

For PPPM and SPME methods the charge assignment function $W(x - x_p)$ is the cardinal B-splines. The spline order shows the number of mesh points to assign charge on. For PME method the charge assignment function is the Lagrange interpolation function. But this method is less efficient [111] than B-spline interpolation. All mesh methods alter only the reciprocal sum (Equation 23) of the initial Ewald summation.

For all the mesh Ewald methods the solution of the Poisson equation in the reciprocal space is written via the back and forward Fast Fourier Transforms [111]:

$$U_{reciprocal} = \frac{1}{2} \sum_{l \in Z} \left(\rho_M(l) \cdot \overleftarrow{FFT} \left[\tilde{G}(k) \cdot \overrightarrow{FFT}[\rho_M](k) \right] \right) \tag{27}$$

where the $\rho_M(l)$ is the charge distribution function discretized on the mesh, the l index of the mesh knots, $\tilde{G}(k)$ is the Fourier transformed "influence function" (please see the reference [111] for more explanations), $\overleftarrow{FFT}[.]$ and $\overrightarrow{FFT}[.]$ are the back and forward fast fourier transform operators.

The equation 27 is common for all the mesh Ewald methods. The various methods differ in the choice of the charge assignment function $W(x)$, the form of the influence function $\tilde{G}$, and the way to evaluate forces from the solution of the Poisson equation [111]. In the mesh Ewald methods employing the direct and back FFT transformations we can calculate the reciprocal Ewald term efficiently with complexity of $O(NlogN)$

4 Results and discussion

4.1 Ion interaction with the carbon nanotube surface in aqueous solutions

The aim of the present study is to understand the basic mechanisms of alkali and halide ions interactions with the CNT's outer surface in water. Recent progress in atomistic computer simulation methods causes a breakthrough in understanding of the molecular effects in the liquid-CNT interfacial region [117, 118, 34, 119]. For example, Mac Kernan and Blau used the Molecular Dynamics (MD) simulations method to explore the mechanisms of SWNT dispersion aggregation in N-methyl-2-pyrrolidone - a highly polar solvent [34]. In this work we are using large-scale fully atomistic MD simulations to reveal the basic molecular mechanisms of ion-CNT interactions in water. We focus on the mechanisms of ion interactions with a CNT, because the CNTs are of primary importance for developing nanoelectronical and biomedical applications of CNTs due to their monomolecular character and extraordinary PL properties [90, 88].

However, in this study we deliberately do not consider the effects of functionalisation because we would like to reveal the mechanisms of selective ion interactions with the unmodified CNT surface, *independently* from the interfering effects of surfactants and cosolvents (which might complicate the general picture). The effects of functionalisation will be considered elsewhere.

There are two main motivations of this study. First, the molecular-scale effects in the CNT-solvent interface layer strongly affect the CNT aggregation and adsorption properties in solution [34, 120]. As ions are known to make significant effects at solute-solvent interfaces [121, 122, 123, 124], the detailed molecular study of ion interactions with CNT surface should have important implications for understanding the molecular mechanisms of CNT aggregation and dispersion in ionic solutions. This should facilitate future developments of drug delivery applications based on CNTs. Biological liquids contain significant amount of salts and that could cause significant effects on CNTs in-vivo. The second reason is to understand the reported effects of ions on the CNT's PL [80, 82, 83], when the nanoscale changes of ion concentrations in the interfacial CNT-solvent region need to be taken into account. The MD simulations method provides the most detailed picture of such molecular scale processes.

4.1.1 Simulation Methods

1) Systems under the investigation.

Molecular Dynamics (MD) simulations were performed with the Gromacs 4.0.4 package [125]. We have simulated a segment of a single-wall carbon nanotube solvated in neat water and in seven different 0.3 M alkali halide water solutions (NaF, NaCl, NaBr, NaI, LiCl, KCl, and CsCl). Additionally, we performed simulations of these solutions without the nanotube.

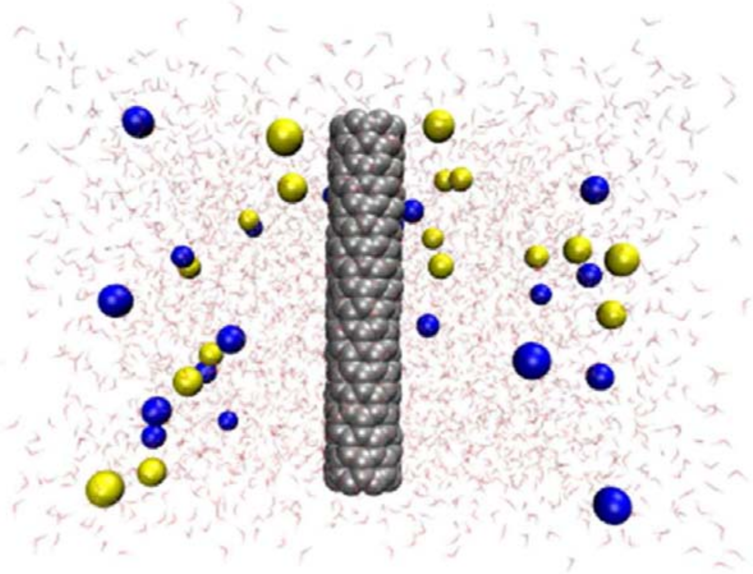

Figure 15: An example simulation box of CNT(7,0) dissolved in 0.3M NaF aqueous solution. Grey balls represent the CNT, blue balls are sodium ions, yellow balls are fluoride ions, water molecules are represented as sticks.

2) Topology and potential parameters.

The 252-carbon segment of SWNT (chirality (7,0), with diameter 0.565 nm) was placed in a periodic rectangular simulation cell ($5.50 \times 5.50 \times 3.92\ nm^3$) and was aligned along the Z axis. To generation teh coordinates of the CNT atoms we used the on-line TubeGen 3.3 tool [126]. We used cubic periodic boundary conditions, where the CNT was treated as a “periodic molecule”. The positions of CNT atoms were restrained to the initial values by harmonic potential with $1000\ kJ \cdot mol^{-1} \cdot nm^{-2}$ force constant in each direction.

Nonbonded interaction parameters for the CNT carbon corresponded to the benzene OPLS-AA (all-atom optimized molecular potential for liquid simulation)[127] carbon (opls_145 in Gromacs notation), the partial charges were set to zero. The equilibrium values for the structural parameters of the bonded interactions (bond lengths, angles, dihedral angles) were taken from the initially generated structure of the CNT, while the force constants for the bond and angle harmonic potentials and the Fourier coefficients for dihedral angles were adopted from the OPLS-AA force field [127]. The nonbonded interactions in the systems were pair-wise additive. The Lennard-Jones coefficients for atoms of different kinds were obtained as a geometric mean value of the parameters of two corresponding particles:

$$\begin{aligned} \varepsilon_{ij} &= \sqrt{\varepsilon_{ii} \cdot \varepsilon_{jj}} \\ \sigma_{ij} &= \sqrt{\sigma_{ii} \cdot \sigma_{jj}} \end{aligned} \tag{28}$$

where i and j indicate type of particle.

We used two different sets of parameters describing the structure and interaction potentials for water molecules and ions. For the first set, we took the model parameters from the following references: the TIP4P water model [128], Åqvist's Na^+ and Li^+ cations [129], F^- and Cl^- [130], Br^- [131], I^- [132] (Table 1). In the present work we refer to this set of potential parameters as the **Jorgensen set**. For the second set, we took the model parameters from the following references: the TIP4Pew water model [133] and the Joung and Cheatham's parameters for ions [134]. We refer to this set of potential parameters as the **Cheatham set** (see Table 1).

3) Molecular Dynamics algorithms details.

We used the leap-frog integrator [135] with 0.001 *ps* integration time step. For the Lennard-Jones potential we used 1.00 *nm* cut-off radius with shifting potential method. The neighbor list for the nonbonded interactions was updated each 10 integration steps. For accurate evaluation of the long range Coulomb interactions we used the Particle Mesh Ewald method [112] with 1.10 *nm* cut-off radius for the real space sum. We used the 0.12 nm spacing for the mesh in the real space and cubic *B*-splines to map the charges on the mesh.

For the NVT-ensemble (canonical ensemble) simulations we used the Nose-Hoover [136, 137] thermostat with the reference temperature of 300K and the relaxation time of 0.1 *ps*. For the NPT-ensemble (isothermo-isobaric ensemble) simulations we used the Berendsen thermostat and also the Berendsen barostat [138]. In this case the system was coupled to an external pressure of 0.1013 *MPa* with the relaxation time of 0.5 *ps*. For the systems containing CNT, we employed a semi-isotropic barostat which could change the size of the simulation cell only in the directions perpendicular to the periodic CNT molecule. For the bulk solvent systems we used the isotropic barostat.

4) Systems preparation and collection of statistics.

a) Jorgensen set:

In the case of the Jorgensen set, we simulated all the systems, except those containing KCl and CsCl solutions. These systems were prepared in the following way. 3617 water molecules were placed around the CNT in the periodic rectangular box. The system was equilibrated during 200 *ps* of the simulation time in the NVT-ensemble and then 300 *ps* of the simulation

Table 1: Potential parameters for some atoms. σ and ε are parameters for the Lennard-Jones potential, q is a partial charge on atom.

	Atom	σ, nm	ε, kJ/mol	**q**, e
The Jorgensen set	F^- [130]	0.2733	3.012480	-1.00000
	Cl^- [130]	0.4417	0.492833	-1.00000
	Br^- [131]	0.4624	0.376560	-1.00000
	I^- [132]	0.5400	0.292880	-1.00000
	Na^+ [129]	0.3330	0.011598	1.00000
	Li^+ [129]	0.2126	0.076479	1.00000
The Cheatham set [134]	F^-	0,4522	0,006595	1.00000
	Cl^-	0.4918	0.048824	-1.00000
	Br^-	0.4932	0.127184	-1.00000
	I^-	0.5260	0.174624	-1.00000
	Li^+	0.1440	0.435379	1.00000
	Na^+	0.2184	0.705214	1.00000
	K^+	0.2833	1.170065	1.00000
	Cs^+	0.3364	1.651407	1.00000
	O_{water}(M site of TIP4P) [128]	0.0315	0.648520	-1.04000
	O_{water}(M site of TIP4Pew) [133]	0.1644	0.680962	-1.04844
	C_{CNT}[127]	0.3550	0.292880	0.00000

time in the NPT-ensemble. The final coordinates were used to generate the systems with the CNT in the saline water solvents. For preparation of 0.3 mol/L salt concentration, 42 water molecules were randomly replaced with 21 ion pairs. Then each system was equilibrated during 200 *ps* of the simulation time in the NVT-ensemble and 300 *ps* of the simulation time in the NPT-ensemble. Then all the systems were simulated in the NVT-ensemble during 30 *ns*. Coordinates of the system were sampled each 0.15 *ps* for the further analysis.

In the simulations of the bulk solvent systems 4079 water molecules were placed into a cubic box with the edge length equal to 5.0 *nm*. The equilibration period took 30 *ps* of the simulation time in the NVT-ensemble and 300 *ps* of the simulation time in the NPT-ensemble. Similar to the systems containing CNT, the resulting coordinates for pure water simulation were taken to prepare the initial coordinates for the salt-water systems (but 23 ion pair replaced water molecules in this case). Each system was equilibrated during 30 *ps* of the simulation time in the NVT-ensemble and 300 *ps* of the simulation time in the NPT-ensemble. The statistics was accumulated during subsequent simulation in the NVT-ensemble during 5 *ns* and the coordinates of the system were sampled each 1.0 *ps* for the further analysis.

b) Cheatham set:

In the case of the Cheatham set we simulated all the systems including those containing KCl and CsCl. We took the final coordinates of the systems after the 30 *ns* simulation for the Jorgensen set as the initial coordinates for the simulations with the Cheatham set of potential parameters. The systems with KCl and CsCl salts were created in a similar way to the systems for the Jorgensen set. For the systems with the solvated CNT the equilibration period was 200 *ps* of the simulation time in the NVT-ensemble and 800 *ps* of the simulation time in the NPT-ensemble, where the box dimensions were sampled each 0.01 *ps*. We took the last 500 *ps* of the NPT-ensemble simulations to average the box dimensions. Then all the systems were simulated in the NVT-ensemble during 30 *ns* where the box dimensions were set to the above-mentioned averaged dimensions. Coordinates of the system were sampled each 0.15 *ps* for the further analysis.

The bulk systems for the Cheatham set were equilibrated during 30 *ps* of the simulation time in the NVT-ensemble and 500 *ps* of the simulation time in the NPT-ensemble. Last 450 *ps* were used to average the box-dimensions. The statistics was accumulated during the subsequent 5 *ns* simulation in the NVT-ensemble and the coordinates of the system were sampled each 1.0 *ps* for the further analysis.

5) Particle-carbon nanotube Radial Density Profiles (RDPs).

1. Calculation details.

We calculated the radial density profiles, averaged over cylindrical shells centered at the axis of the CNT. These profiles were normalized to the bulk densities ρ^0 of the corresponding species. Our normalization procedure included the following steps. Initially we used an average concentration in the simulation box to normalize the RDP curves (see Figure 16a).

However, this normalization is incorrect as we had to normalize the curves with respect to the bulk concentration rather than to the average concentration in the simulation boxes (number of particles/total volume). We note that in the simulation there is a large excluded volume of the CNT, which is not accessible by the solvent. Because of this, the number density of species is underestimated by *g_rdf* and, consequently, although the calculated RDPs become constant at large r values, these constants are larger than 1.

We have to account the excluded volume effect of the CNT. To do that we averaged the values of the radial density profile of water oxygen in the range of r of 1.6 - 2.5 *nm* (see Figure 16b)). Then to obtain the scalling factors we took the values in the -1 power. The scaling factors for the renormalization were 0.975 for TIP4Pew water model and 0.976 for TIP4P model. Scaling the oxygen water density profiles in different systems with these factors makes the curves equal to unity for large r. Assuming that these factors are universal, we rescaled with them all the ion-CNT and water hudrogen-CNT RDPs.

4.1.2 The carbon nanotube hydration shell

Firstly, we analyzed the density distributions of water and ions around the CNT by means of radial density profiles (RDPs) averaged over cylindrical shells centered at the axis of the nanotube. We normalized the RDPs by the bulk concentrations of the molecular species to facilitate the comparison between the different species. In the following analysis, description and interpretation of our results, we will intensively employ the conception of solvation shells around a solute (nanotube in our case) developed in Refs. [95, 139, 140, 141, 142, 143, 101]. Describing the water-CNT interface layer we will use the terms *the first and second CNT hydration shells* (see Figure 17a). In turn, the *first CNT-ion interface shell* indicates the volume around the CNT surface where the ions are in direct contact with the CNT surface. Correspondingly, the *second CNT-ion interface shell* indicates the volume around the CNT surface, where the ions are separated from the surface by one water molecular layer. Discussing the properties of water molecules around ions we will use the term *ion hydration shell* (see Section. 2.1.4).

Figure 17a shows the RDP of water oxygens around the CNT surface in the neat water solution as well as a characteristic simulation snapshot of positions of water molecules in the first

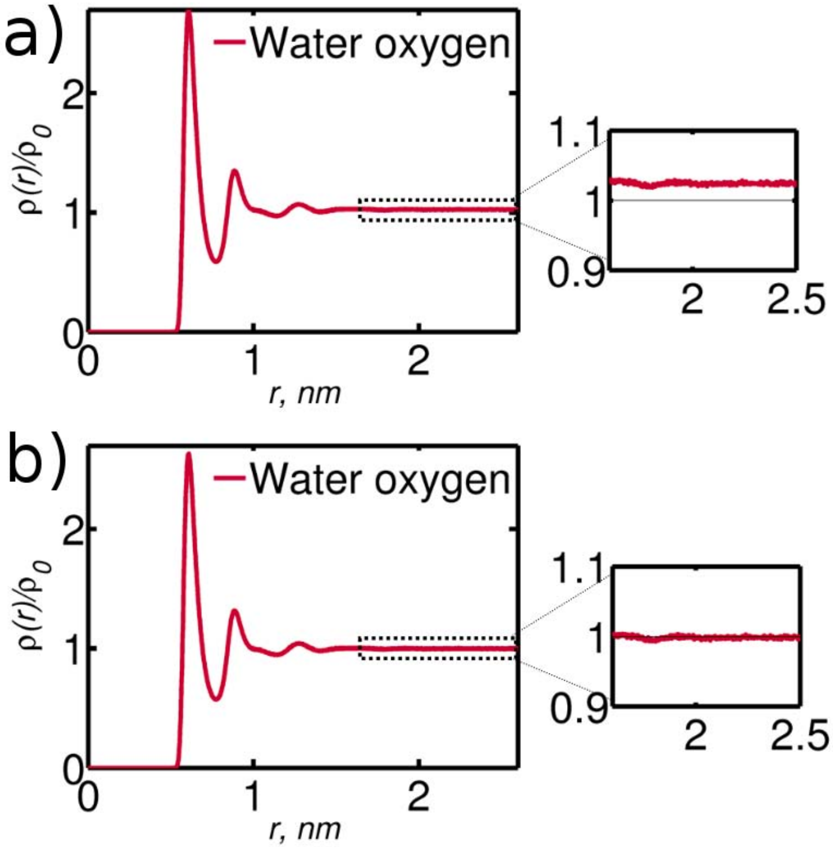

Figure 16: The calculated radial density profile of water oxygen around the CNT center of mass for the CNT in pure water solution: a) normalized RDP with respect to the average density in the volume of the simulation box. Far away from the CNT the curve comes to the constant value that does not equal to unity because of the excluded volume effect of the CNT, b) the same curve as in the case (a), scaled with a factor correcting the excluded volume effect of the nanotube. The data are shown for the TIP4Pew water model.

two hydration shells of CNT. As given in works [117, 118], RDP of water oxygens around the CNT surface (see Figure 17a) shows two significant peaks corresponding to the two distinctive CNT hydration shells around the CNT surface with the second hydration shell being more diffusive than the first one. Similar to the work [117], we found that the preferential orientation of water molecules in the first CNT hydration shell is almost parallel to the CNT surface. This can be seen from the positions of the water molecules in the first CNT hydration shell shown on Figure 17a. The Radial Density Profiles for water oxygen and hydrogen for the system of CNT in pure water are presented in Figure 18. The first peaks on the distributions being closely positioned indicating that the first hydration shell of water molecules around CNT preferentially lay on the CNT surface (the plane connecting centers of hydrogens and oxygen are parallel to the CNT surface).

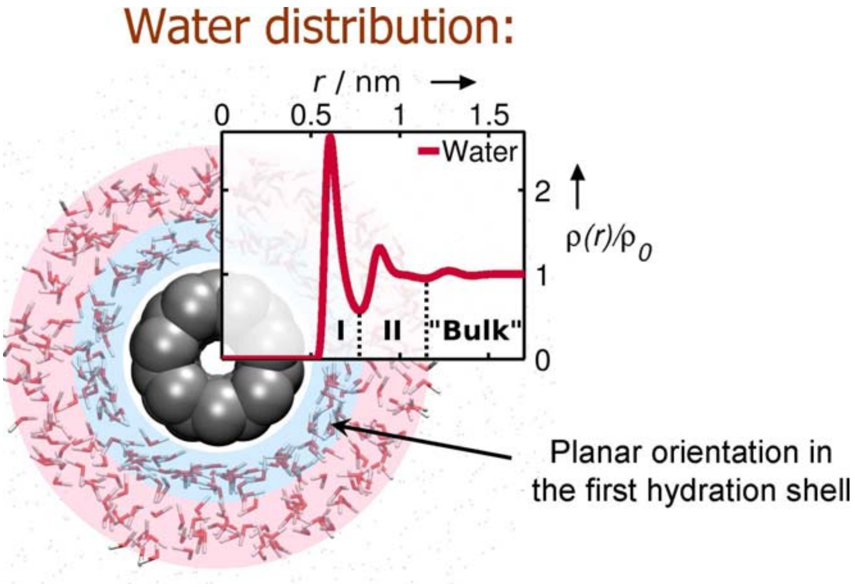

Figure 17: Water molecules distributed around CNT. Colour selections show the first (blue) and second (pink) hydration shells. The CNT-water RDP shows two significant peaks corresponding to the first (I) and second (II) CNT hydration shells.

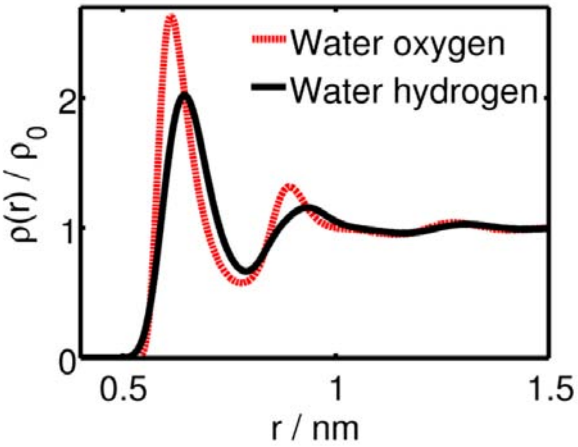

Figure 18: The water oxygen and hydrogen radial density profiles around the carbon nanotube.

4.1.3 Ion distributions around the carbon nanotube

Figure 19 shows the RDPs around the CNT surface and characteristic molecular snapshots for two ions: i) fluoride (Figure 19, left side) as a representative of ‘small’ ions with high surface charge densities, and, ii) iodide (Figure 19, right side) as a representative of ‘large’ ions with low surface charge densities [105]. The distributions of other ions are presented on the Figure 21.

The density profile for fluoride ions on Figure 19 (left side) clearly shows that the fluoride

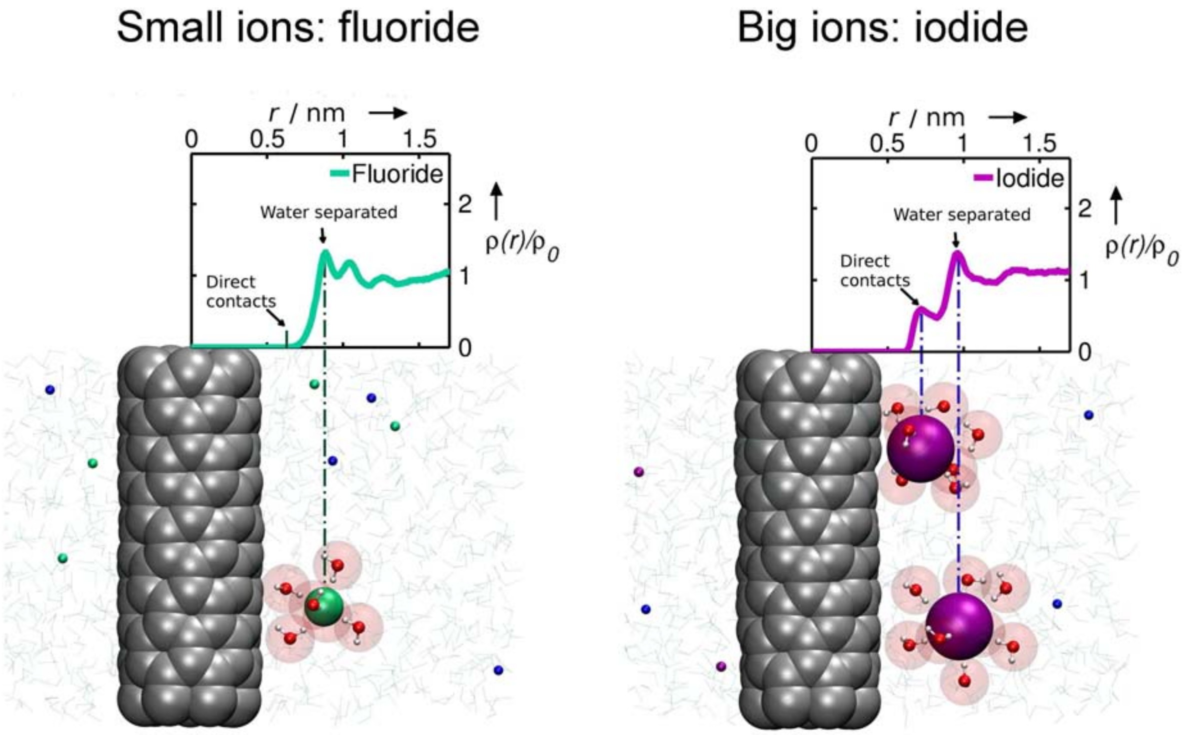

Figure 19: (left side) This picture illustrates the water-separated contacts of fluoride ions with the CNT surface. Small blue and green spheres correspond to the F^- and Na^+ ions. The size of the selected fluoride ion (large green sphere) corresponds to the van-der-Waals (VDW) size of the ion. The water molecules in the first hydration shell of the selected ion are shown by balls and sticks; the VDW spheres of the water oxygens are shown as transparent red spheres. (right size) The overall style of the picture is the same as for the previous one. I^- ions are shown by magenta spheres. Two characteristic positions of the iodide ions close to the CNT surface correspond to the two selective peaks on the CNT-iodide RDP: direct contacts (top ion) and water-separated contacts (bottom ion).

ions practically *do not make direct contacts* with the CNT surface and tend to be separated from the CNT by at least one water layer as illustrated by the molecular picture on Figure 19 (left side). We attribute the slight increase of the ions density comparing to the bulk solution in the second CNT-fluoride interface shell to the attraction of ions to the water in the first CNT hydration shell. We found that the RDP of fluoride ions around the CNT surface is *qualitatively* similar to RDPs of other ions of small size as it is shown on Figure 21.

Contrary to fluorides, the iodides *do make direct contacts* with the CNT surface. As indicated by the CNT-iodide RDP, the concentration of iodides in the first CNT-iodide interface shell is only half less than the bulk concentration of iodides (see Figure 19 (right side)). The two selective peaks on the CNT-iodide RDP indicate a presence of two characteristic positions of the iodide ions close to the CNT surface: *direct contacts* of the iodides with the CNT surface (first peak) and *water-separated* contacts (second peak). We found that the mechanism of interaction of iodides with the CNT surface is *qualitatively* similar to other large ions with low surface charge density (Cs^+ and Br^-) considered in this study (the corresponding data are given in Figure 21).

We note, that an increase of the concentration of the large ions at different metallic surfaces have been observed previously by Spohr et al. [144, 145], Perera and Berkowitz [146]. These findings are in line with our observations.

4.1.4 Ion-carbon nanotube interface shell criteria

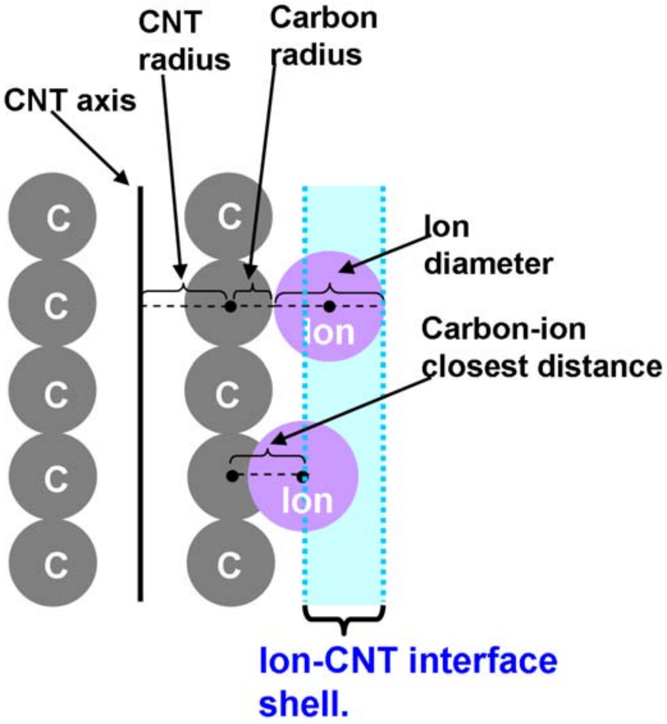

Figure 20: Ion-carbon nanotube interface shell.

To quantify the number of direct contacts of different particles with the CNT surface we introduce the term particle-CNT interface shell. We consider the particles occurring in the first particle interface shell of CNT to be in direct contact with the CNT surface (like water molecules in the first hydration shell of CNT). We stress that it is important to consider different criteria for different particles because of the differences in the particle sizes. In our case the particle-CNT interface shell is the volume between two cylindrical layers around CNT, with the radius of the inner layer being R_I and the radius of the outer layer being R_{II}. The R_I is determined in the

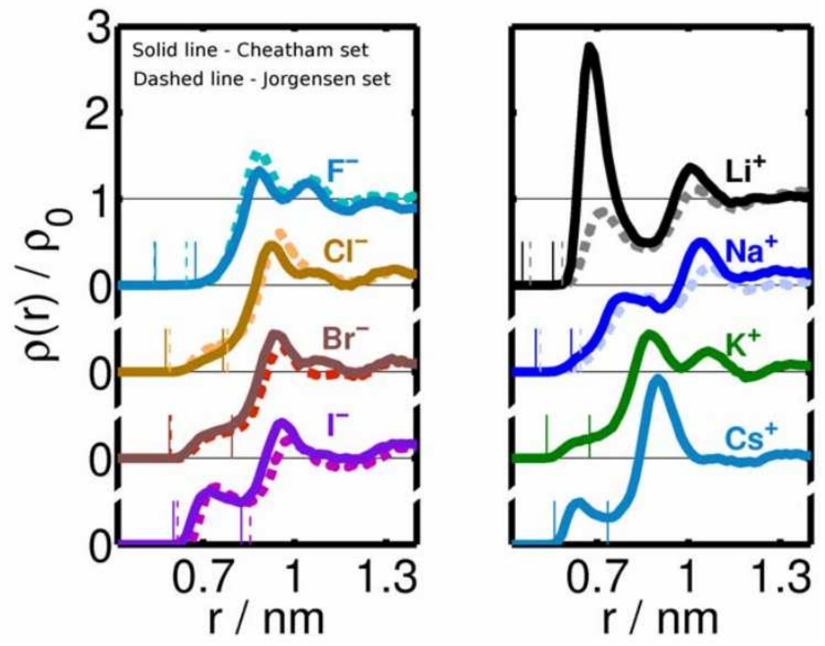

Figure 21: Radial density profiles for ions around carbon nanotube. The thin vertical lines indicate the boundaries of the first CNT-ion interface shell. Solid lines - data for the Cheatham set, dashed lines - data for the Jorgensen set of potential parameters. For the Jorgensen set there are no data for Cs^+ and K^+ ions. Enhanced concentration of Li^+ close to the interface shell is very similar to what was found by Perera and Berkowitz [146].

following way:

$$R_I = R_{CNT} + D_{carbon-ion}$$

where: R_{CNT} is the CNT radius (equals to 0.283 nm), $D_{carbon-ion}$ is the closest ion-carbon distance, in this work it was set to the distance where the interaction energy between carbon atom and the regarding ion equals to 10 k_BT (arbitrary value to define the "hard core" impermeability of the two particles).

For the outer boundary of the particle-CNT interface shell (R_{II}) we chose a usual criteria for the outer boundary of the solvation shell (the position of the first deep minimum on the corresponding radial distribution profile of the solvent species around a solute (see Section 2.1.4). Thus for water the outer boundary of the water-CNT interface shell (R_{II}) would be the position on the first minimum on the water-CNT RDP (see Figure 17). We estimated the positions of the outer boundary of the iodide-CNT and cesium-CNT interface shells also as the positions of the first minima on the corresponding RDPs (see Figures 19 and 21).

For other ions the RDPs do not have the first minimum corresponding to outer boundary of the CNT-ion interface shell (see Figures 19 and 21). Thus, we initially defined the R_{II} for the ions except Cs^+ and I^- to be:

$$R_{II} = R_{CNT} + R_{carbon} + 2R_{ion} \tag{29}$$

where: R_{CNT} is the CNT radius (equals to 0.283 *nm*), R_{carbon} and R_{ion} is Van der Waals radii of the carbon atom and an ion correspondingly, estimated as half the distance where the Lennard-Jones potential of interaction of two particles of the same kind is equal to 1 k_BT.

The described criteria for R_{II} slightly overestimated (by 0.03 *nm*) the outer layer of the first CNT-ion interface shell in the case of Cs^+, where the R_{II} is determined by the position of the first minimum on Cs^+-CNT RDP. Thus, for K^+, Na^+, Li^+ we reduced the radius of the outer layer of the first CNT-ion interface shell (estimated by Eq. 29) by 0.03 *nm* for keeping consistency.

In the case of anions only iodide RDP has a minimum corresponding to the outer layer of the first CNT-ion interface shell. We had to reduce the calculated by Eq. 29 R_{II} by 0.06 *nm* for all anions distributions.

The obtained values of R_{II} were then rounded to the nearest value of the discretized RDPs curves. The interval between the nearest points on a RDP was 0.015 *nm*. The resulting criteria for the Cheatham and Jorgensen sets of ion parameters are presented in Table 2.

4.1.5 Partial dehydration of ions at the carbon nanotube surface

Contacting a surface, ions undergo partial dehydration typically loosing about one water molecule from their hydration shell [146, 144, 148]. Therefore, we assume a possible correlation between the strength of ion-water interactions in the first hydration shell of ions and the concentration of ions in the CNT-water interface layer.

To investigate the partial dehydration of ions we calculated the hydration number of ions as functions of distance from the CNT surface (see Figure 22). From the Figure 22 one can see that the hydration of ions (on examples of Cs^+ and I^-) is significantly perturbed by the CNT surface: the hydration numbers reach their bulk values only at 1.5 *nm* distance from the CNT axis (more than 1 *nm* from the CNT surface). Interestingly, the hydration numbers of ions even slightly increase at r=0.85-0.90 *nm* compared to the values in the bulk. This distance region corresponds to the *water-separated contacts* of the ions with the CNT surface (see Figure 19 (right side) and Figure 21). We attribute this to the fact that the structure of the water hydrogen-bond network at hydrophobic surfaces is disturbed by the surface, resulting in weakening of water-water interactions (number of H-bonds) [149] which makes it easier for the water molecules to interact with the ions increasing their hydration number.

Table 2: The first CNT-ion interface shells of different ions for the Cheatham and Jorgensen sets of potential parameters.

	Ion	**Boundaries of the first CNT-ion interface shell.**		**Concentration in the first CNT-ion interface shell normalized by bulk density.** ρ_{s1}/ρ_0
		R_I	R_{II}	
Cheatham set	F^-	0.543	0.675	0.00
	Cl^-	0.577	0.765	0.10
	Br^-	0.589	0.795	0.20
	I^-	0.603	0.825	0.41
	Li^+	0.455	0.555	0.00
	Na^+	0.499	0.615	0.02
	K^+	0.534	0.675	0.13
	Cs^+	0.560	0.735	0.32
Jorgensen set	F^-	0.540	0.645	0.00
	Cl^-	0.590	0.780	0.20
	Br^-	0.594	0.795	0.20
	I^-	0.616	0.855	0.46
	Li^+	0.481	0.585	0.00
	Na^+	0.514	0.645	0.04

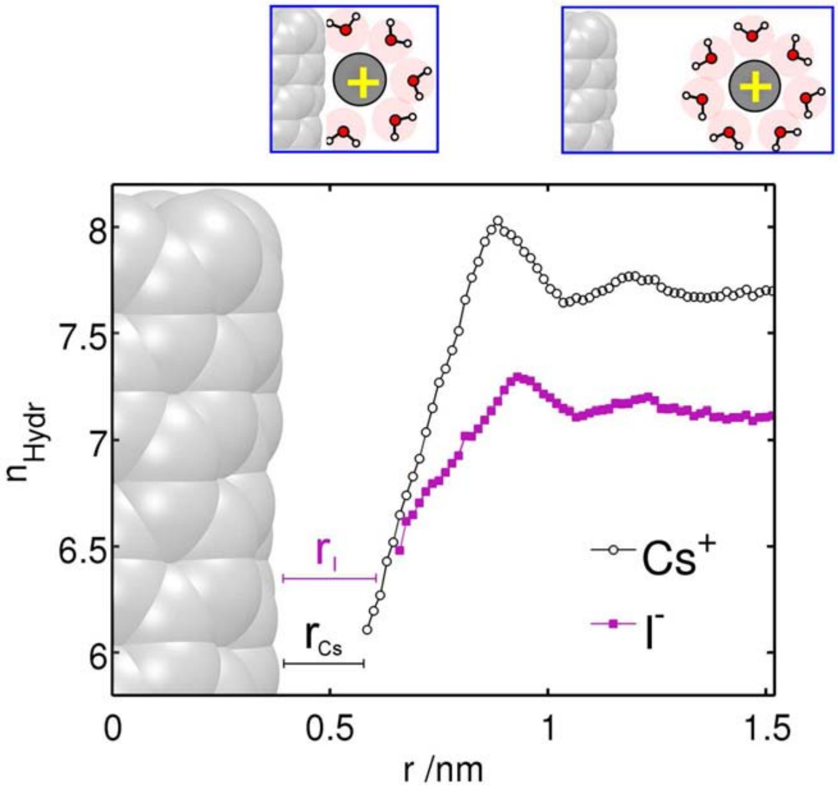

Figure 22: Cs^+ and I^- ion hydration numbers as a function of distance from the CNT. Decreasing the distances lower than 0.85-0.90 *nm* (ions dive into the the CNT first hydration shell) results in a gradual decreasing of the hydration number of ions. Similar functions were calculated for different ions at a solid surface by Spohr [147] and Perera, Berkowitz [146].

Decreasing the distances lower than 0.85-0.90 *nm* (ions dive into the the CNT first hydration shell) results in a gradual decreasing of the hydration number of ions (see Figure 22). The closer an ion to the CNT surface the smaller is its hydration number. This clearly indicates that ions become partially desolvated forming direct contacts with the CNT surface. The ion partial desolvation at the CNT surface happens because of the steric restraints caused by the surface. Indeed, the hydration shell of ions simply starts to overlap with the CNT surface, and thus effectively the volume of the hydration shell decreases upon approaching the surface.

We have estimated the number of water molecules an ion releases when it attaches to the CNT surface. This was estimated as the difference between the average hydration number of ions in the bulk solution (see Table 3) and the average hydration number of ions in the CNT-ion interface shell. We present the results on the Figure 23. The figure shows that to approach the CNT surface cations have to release 1-2 water molecules from their hydration shells, but anions release only 0-1 water molecules. This clearly indicates asymmetry of anion and cation interactions with the CNT surface in aqueous dispersions. Indeed, cesium cation releases in

Table 3: Hydration numbers of ions for the Cheatham and Jorgensen sets of potential parameters. The hydration number of ions are estimated as the average number of water oxygen atoms within the distance of the first hydration shell of ions (position of the first minima on the corresponding ion-water oxygen radial distribution functions).

Ion	**Jorgensen set**	**Cheatham set**	**Experimental**[141]
F^-	6.2	6.0	6.0
Cl^-	6.7	6.5	5.9 - 8.5
Br^-	7.0	6.8	4.2 - 8.9
I^-	7.3	7.1	6.0 - 8.9
Li^+	3.6	3.8	4.0 - 6.0
Na^+	5.5	5.7	4.0 - 8.0
K^+	-	6.5	6.0 - 8.0
Cs^+	-	7.7	6.0 - 8.0

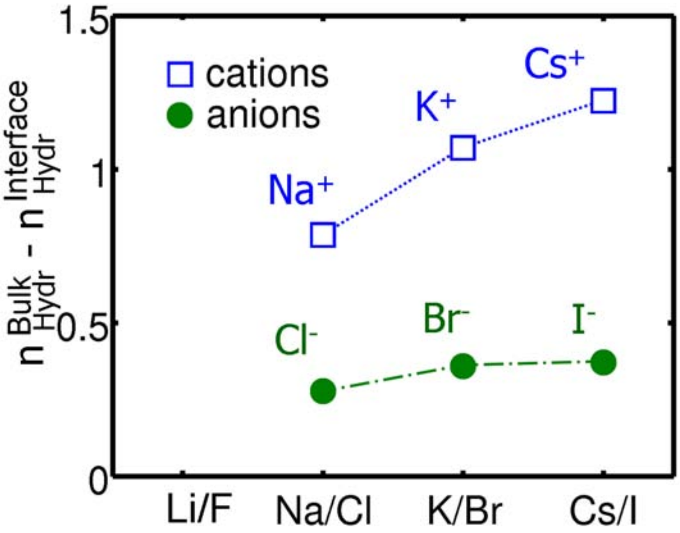

Figure 23: The number of water molecules an ion releases from its hydration shell when it attaches to the carbon nanotube surface. For Li^+ and F^- no direct contacts were observed during the 30 ns simulation time.

average about 1.3 water molecules from its hydration shell, while Cl^- being of similar size releases in average only about 0.3 water molecules.

We attribute the difference between cations and anons in the number of released water

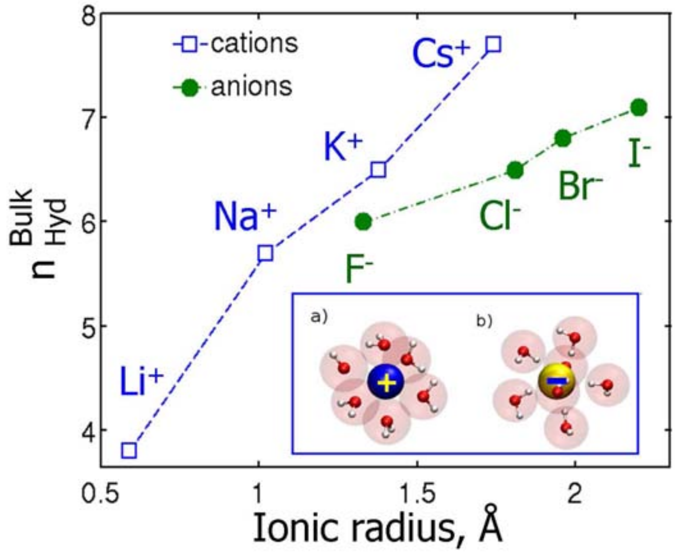

Figure 24: Ion hydration number as a function of ionic radii for the Cheatham set of potential parameters (see Table 1).

molecules upon attaching the CNT surface to the difference in the structure of ions' hydration shells. Cations have much denser hydration shell compared to anions (see Figure 24 and Table 3). Indeed, the hydration number of Cs^+ is about 1.2 water molecules larger than the hydration number of Cl^- despite their similar sizes. Thus around cations the water molecules are denser packed. As a result, attaching to the surface cations must release more molecules from their hydration shell. The sparser hydration shell of anions also suggests that when anions attach the surface an anion not necessarily must release water molecules but rather the water molecules can group in a more compact way around the anion. The later point is supported by the fact that anions are much stronger hydrated than cations (see Section 2.2). This makes the partial dehydration for anions to be much more unfavorable than for cations of the same size. The described asymmetry of the cation and anion hydration shows that the structure of the solvent around the ions has an important role in the process of the ion interactions with the CNT surface. Thus, such effects can not be modeled in the studies with the implicit solvation approaches describing the water solvent as a dielectric continuum media.

4.1.6 Measure of the penalty for partial dehydration

Ion-water potentials of mean force. To understand the role of ion hydration in the mechanism of ion interactions with the CNT surface, we calculated potentials of mean force (PMFs) between ions and water following similar approach used in Ref. [150, 78] for investigation of ion distributions at different surfaces. First, the atom-atom radial distribution functions (RDFs) were calculated with the “g_rdf” program of the Gromacs 4.0.4 package and then the PMFs (in the units of $k_B T$, k_B is Boltzmann’s constant and T is temperature) were found as:

$$PMF(r) = -\ln(g(r)) \tag{30}$$

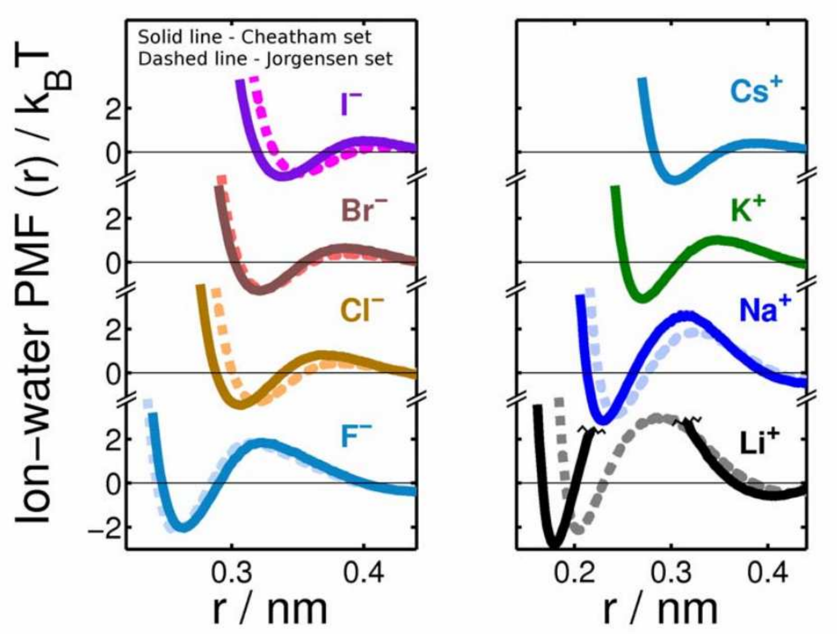

Figure 25: The ion-water PMFs for the two sets of potential parameters. Solid lines - the data for the Cheatham set, dashed lines - data for the Jorgensen set. For the Jorgensen set there are no data for the Cs^+ and K^+ ions.

The resulting PMFs are shown on Figure 25. Ion-water PMFs serve as reaction profiles of one water molecule release from the hydration shell of an ion to bulk solution (see Section 2.1.3).

On Figure 26 we compare the ion-water PMFs to the water-water PMF. The figure shows that the fluorides have a very strong binding affinity to water comparing to the energy of thermal fluctuations, 1 $k_B T$. The fluoride-water binding is also stronger than the water affinity to itself, as the depth of the first minimum of the water-water PMF is less than the one for the fluoride-water PMF. In contrast, large I^- and Cs^+ ions have much less affinity to water and the depth of the first minimum on their ion-water PMF is comparable to the one for the water-water PMF. Thus, these ions can not compete with the water for water molecules and one water molecule can be easily moved away from the hydration shell of these ions.

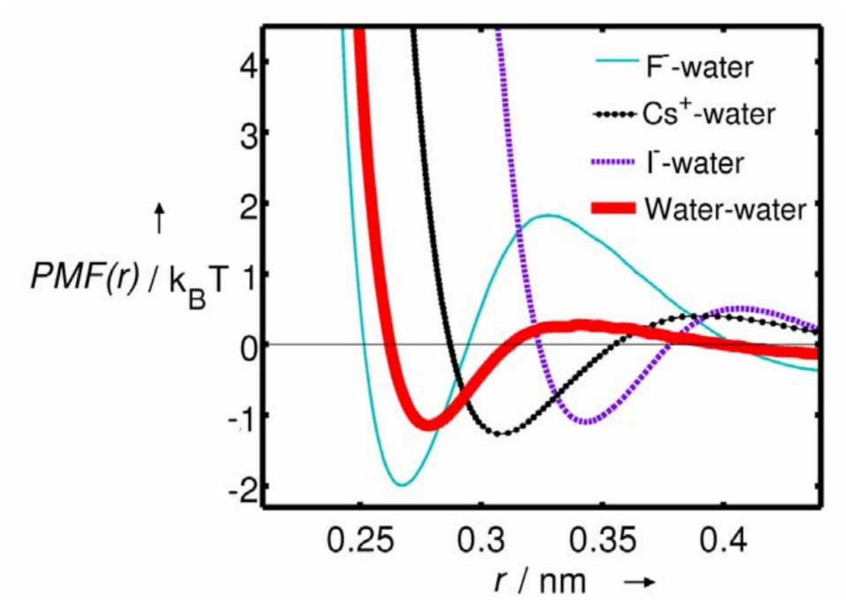

Figure 26: Ion-water PMFs in comparison with the water-water PMF. The free energy to release one water molecule from the ion hydration shell (ΔG^{WR}) can be estimated as the depth of the first minimum on the ion-water PMF.

Free energies of one water molecule release from the ion hydration shell. The PMFs show the change in Gibbs free energy in the process of bringing two selected particles from infinite separation to the selected distance from each other [94]. Thus, using the ion-water PMFs given in Figure 25 we can estimate the free energy to release one water molecule from the hydration shell of an ion (ΔG^{WR}) as the depth of the first minimum on the ion-water oxygen PMF [151, 78]. We use the value ΔG^{WR} as *a measure of the penalty for partial desolvation* of an ion. Our estimations of ΔG^{WR} are consistent with the available experimental data [152, 153, 154] (see Table 4).

4.1.7 Ions concentration in the carbon nanotube-ion interface shell

To quantify the number of direct contacts we calculated the average concentrations of ions in the the first CNT-ion interface shell. These concentrations were then normalized by the bulk concentration of the species (see Figure 27, first row). The bulk concentrations were calculated in the following way. For the systems containing CNT, the numbers of ions were divided by the volumes of the simulation boxes. Then the effect of the CNT excluded volume on the concentration of ions was corrected by dividing the calculated concentrations by the same scaling factors (about 0.98) as we previously used for corrections of the normalized RDP values (see Section 4.1.1).

Table 4: Free energies of one water molecule release from the first hydration shell of ions, ΔG^{WR} ($k_B T$ units).

Ion	External sources[a]	Our data[b]
F^-	2.0 [152]	2.0
Cl^-	1.1 [152]	1.5
Br^-	1.1 [152]	1.3
I^-	0.5 [152]	1.1
Li^+	(2.3 [155]; 2.1 [156]; 2.2 [156]; 2.6 [156])[c]	2.8
Na^+	1.8 [153]	2.2
K^+	1.7 [153]	1.7
Cs^+	1.1 [154][d]	1.3

[a] Data from the external sources were calculated in the following way. For each ion we estimated the value of the first maximum of the corresponding ion-water oxygen radial distribution function from the published plots. The minimum value of the corresponding PMF was found as natural logarithm of the maximum value of this RDF. We took the RDFs for the most diluted ionic systems we could find;

[b] We provide here our simulations data with the set of potential parameters taken from Ref. [134];

[c] The experimental publications provide either only the total distribution functions of lithium in water [157] or the published radial distribution functions are too noisy [158]. We took the data from the molecular dynamics simulations with different sets of potential parameters [156]. The lithium - water oxygen radial distribution function at 0.3 mol/kg concentration of LiCl was taken from Ref. [155] ;

[d] From this source we took the cesium – water oxygen radial distribution function for the 1.5M concentration of CsCl.

Figure 27 illustrates the relationship between the strength of ion hydration described in terms of ΔG^{WR} and the concentration of ions in the CNT-ion interface shell. The figure clearly shows a *negative* correlation between the strength of ion-water interactions and the concentration of ions at the first CNT-ion interface shell: the interfacial region becomes increasingly populated by ions with smaller ΔG^{WR}. Thus, the concentration of strongly hydrated ($\Delta G^{WR} >> 1\ k_BT$) ions such as Li^+, F^- and Na^+ is negligible in the first CNT-ion interface shell. Contrary, there is a significant amount of the weakly hydrated ($\Delta G^{WR} \sim 1\ k_BT$) ions ($Cs^+$, I^-) in the interface area corresponding to direct contacts of ions with the CNT surface (up to 40% of the bulk concentration for iodides). Because of the asymmetry in ion hydration (see Sections 4.1.5) the data for cations and anions are analyzed separately. The general trends for cations and anions are as follows: (i) the larger the size of the ions the larger is the local concentration of the ions in the interface layer; (ii) the smaller the size of the ions the larger is their ΔG^{WR}.

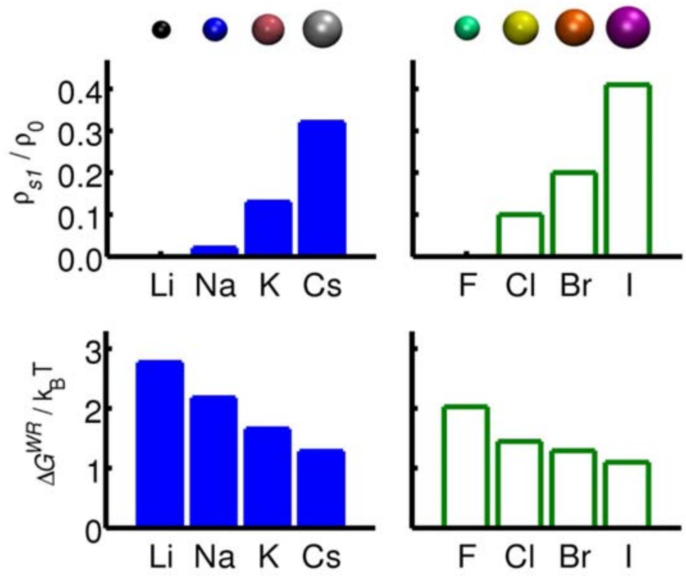

Figure 27: Normalized concentrations of ions in the first CNT-ion interface shells (top) together with the free energy to release one water molecule from the hydration shell of an ion, ΔG^{WR}(bottom). The spheres on the very top of the figure illustrate the relative sizes of the corresponding ions. The data for cations are shown on the left; the data for anions are shown on the right. There is a general trend for all ions: the CNT-ion interfacial region becomes increasingly populated by weakly hydrated ions with lower ΔG^{WR}. Because of the asymmetry hydration (see Sections 4.1.5) the data for cations and anions is presented separately.

4.1.8 Ions residence times at the carbon nanotube-water interface

We found a *positive* correlation between the size of ions and the average residence time $< t_R >$ of ions in the first CNT-ion interface shell. We define $< t_R >$ as the average time for a particle to stay in the first CNT-particle interface shell. During the simulation the instant t_R values for all the particles of certain kind that left the first interface shell were collected in a numerical array. The averaged value $< t_R >$ was obtained via averaging over the array of the instant t_R values.

To correct the artifacts produced by the oscillatory motion of the particles located at the CNT-particle interface shell boundary, we applied two additional parameters for the calculation of the instant residence times t_R: t_{GAP} - the minimum "absence time" of the particle in the CNT-particle interface shell; and t_{min} - the minimum residence time of the particle in the CNT-particle interface shell. t_{GAP} has the following physical meaning: if the particle that left the first CNT-particle interface shell returns back in a period of time less than t_{GAP}, then this particle is considered being not left the interface shell. Similarly, the meaning of t_{min} is: if the particle stays in the first CNT-particle interface shell less than t_{min} then we assume that it did not enter the interface shell. Following the work of Impey et al. [98], we set t_{GAP} to 2 *ps*; and we set t_{min} to 0.5 *ps*.

The boundaries for the first CNT-ion interface shells are presented in the Table 2. The water-CNT interface boundary was set to - 0.778 *nm* - the position of the first minimum on the water oxygen-CNT radial density profile (see Figure 18).

The residence time for the sodium ions located in the first CNT-sodium interface shell did not exceed the minimum value of the residence time t_{min} in the above described criteria. On the Figure 28 the average residence time for Na^+ was set to 0.5 *ps*, showing the upper limit of this value.

We note that the described way to calculate the residence times of particles differs from the conventional method which manipulates with the so-called "residence time correlation function" [159, 98]. The scheme used in this study directly answers the question "how long a particle stays in the CNT-ion interface shell" and thus can be easily understood. We note, however, that the residence times estimated with this method would depend on the two additional parameters t_{GAP} and t_{min}, but in this study we are interested only in the general trends and thus the described method is sufficient.

The average ion residence times in the first CNT-ion interface shell are in the range of $2 \div 9$ *ps*. The $< t_R >$ data for ions and water are presented in Figure 28, showing an increase in $< t_R >$ with the growth of ion size. We note, that the water residence time is about twice higher ($\sim$ 18

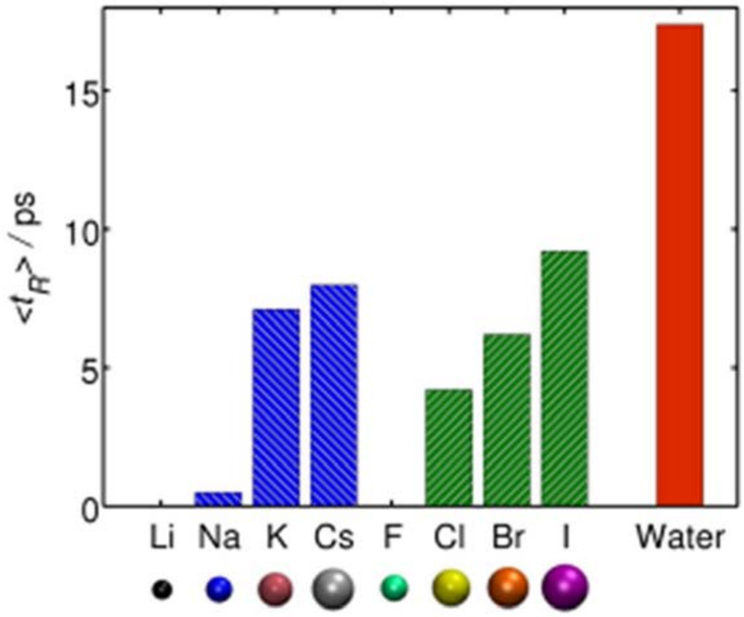

Figure 28: Average residence times, $< t_R >$, of ions and water in their CNT interface shells. The spheres on the bottom of the figure illustrate the relative sizes of the corresponding ions. $< t_R >$ practically equals zero for Li^+ and F^- ions due to the negligible concentration of the ions in the CNT-Li^+ and CNT-F^- interface shells (see Figure 27).

ps) than the maximum residence time for ions (~ 9-10 *ps*). This observation correlates with the significant increase of water density in the first CNT-water interface shell comparing to the bulk density (see Figure 17a).

4.1.9 Discussion of the simulation results in light of experimental data

The observation that the CNT-ion interfacial region becomes increasingly populated by weakly hydrated ions (with smaller ΔG^{WR}) correlates with the experimental observations in Ref. [160] showing that large halogens form complexes with nanotubes in polar solvents. Our findings are consistent with results of other studies on ion interactions with hydrophobic surfaces [121, 122, 123, 124, 161], also showing correlations between the size of ions and the local concentration of ions in the surface layer of water.

Our results can help in understanding the observed correlation between the radii of ions and the strength of ion effects on the CNT photoluminescence quenching in aqueous solutions observed in experimental works [82, 83]. Indeed, weakly hydrated ions (like iodide or cesium) have large probability to lose water molecules from their hydration shell and to approach the CNT surface to form direct contact. The formation of the direct contact is important for the

Dexter mechanism of photoluminescence quenching [162], which "can occur only when the fluorophore and quencher are close enough to allow orbital overlap" [163].

4.1.10 Conclusions

There are the following conclusions from this section:

1. Small ions with high surface charge density (e.g. Li^+, F^-) make *no direct contacts* with the CNT surface. The reason of this is the strong hydration of the ions. As a result, ions unable to approach the CNT surface closer that the size of one water molecule.
2. Large ions with low surface charge density (Cs^+, Br^-, I^-) can make a significant amount of direct contacts with the CNT surface. This is because these ions are weakly hydrated due to their low surface charge. Consequently, their hydration shells can easily lose one water molecule that allows them to make direct contacts with the CNT surface.
3. There is a strong negative correlation between the strength of ion hydration and the probability of a direct CNT-ion contact: the interfacial region becomes increasingly populated by weakly hydrated ions with lower ΔG^{WR}.

We believe that these findings should be interesting for the many scientists working in the field of CNTs dissolution and surface-specific effects in CNTs and will provoke more experimental studies on interfacial ion effects on CNTs. Importantly, our results could help the understanding of the mechanisms of ion effects on CNTs photoluminescence in aqua solution that should help the development of new nanotube-based functional devices by using bottom-up molecular engineering in the liquid phase.

4.2 Ion interaction with the carbon nanotube surface in N-methyl-2-pyrrolidone dispersions

In this section we study the salt (NaI) effects on CNT-NMP dispersions by a combination of fully atomistic molecular simulations. We have chosen N-methyl-2-pyrrolidone (NMP) as an organic solvent because this is one of the most promising solvents for making dispersions of pristine CNMs [31, 32]. Such, it is possible to obtain at least 0.02 mg/mL concentration of CNTs in the bulk NMP solution without any additional dispersing agents and the dispersion may stay stable for weeks [164]. To study the ion effects we use the sodium iodide salt because in contrast to sodium chloride and many other inorganic salts, NaI is soluble in NMP at least up to 0.2M [165].

We note that, an addition of surfactants (e.g. polyvinylpyrrolidone, Triton X-100 etc.) can increase the concentration of the CNTs in the dispersion much further than 0.02 mg/mL [166]. However, we focus on the ion effects in bulk NMP-CNT dispersions to avoid any interference of ion effects on CNTs with possible ion effects on the surfactant molecules.

4.2.1 Simulation details

We performed Molecular Dynamics (MD) simulations of a single-wall CNT with (8,6) chirality dissolved in 0.15M NaI NMP solution to reveal the basic molecular mechanisms of ion interactions with the carbon nanotube surface. Overall, the simulation strategy is the same as in the case of aqueous solutions (see Section 4.1.1).

1) Systems under the investigation.

We performed Molecular Dynamics (MD) simulations using the Gromacs 4.5 MD software package [167]. We simulated a segment of CNT (8,6) of 5.186 nm length solvated in pure NMP (N-methyl-2-pyrrolidone) and 0.15M NaI NMP solution. Additionally we performed simulations of the bulk NaI-NMP solvent.

2) Molecular topology and potential parameters used in the simulations.

Firstly, we generated a molecular simulation topology for a CNT segment consisted of 592 carbon atoms (chirality (8,6) with tubule radius of 0.477 nm). For generation of the CNT topology we used the on-line TubeGen 3.3 tool [126]. Then the CNT was placed in a rectangular simulation box ($7.50 \times 7.50 \times 5.19$ nm^3) and was oriented along the Z axis of the box. We used the rectangular periodic boundary conditions, where the CNT was treated as a “periodic molecule”. The positions of the CNT atoms were restrained to the initial values by harmonic potential with 1000 $kJ \cdot mol^{-1} \cdot nm^{-2}$ force constant in each direction. The set of potential parameters and molecular topology of the CNT was defined the same way as in the Section 4.1.1. But in the present case we have not applied the potentials on the dihedral angles, the absence of dihedral potentials is compensated by the restraining potential. The Lennard-Jones coefficients for atoms of different kinds were obtained as a geometric mean value of the parameters of two corresponding particles (Equation 28).

We employed the fully atomistic OPLS-AA force field [168, 169, 170] which has been thoroughly tested for NMP and similar organic solvents in Refs. [32, 171, 172]. The OPLS-AA potential parameters were assigned to NMP molecule with the use of Shrodinger Maestro software [173]. The parameters were then transformed into the Gromacs topology format, where the Fourier coefficients of the dihedral potential term were transformed into the Ryckaerd-Bellemans type [174]. For sodium iodide, we used the recent set of ion parameters developed consistently with the general framework of the OPLS force field [170]. However, to prevent possible crystallization of the salt during the simulation time we increased the interionic $\sigma_{Na^{+}-I^{-}}$ Lennard-Jones term, estimated by Equation 28 by 0.05 *nm*. We believe that this is reasonable, because the ion potential parameters were parameterized to match properties of the infinitely diluted aqueous solutions where the LJ cross terms (σ_{Na-I} and ϵ_{Na-I}) were not parameterized and were taken estimated according to the general OPLS combining rules (Equation 28).

3) MD algorithms details.

We used the leap-frog integrator with 0.002 *ps* integration time step. For the Lennard-Jones potential we used 1.00 *nm* cut-off radius with shifting potential method. The neighbor list for the nonbonded interactions was updated each 10th integration step. For accurate evaluation of the long range Coulomb interactions we used the Particle Mesh Ewald method with 1.10 *nm* cut-off radius for the real space sum and 0.12 *nm* spacing for the mesh in the real space. The cubic B-splines were used to map the charges on the mesh.

The length of all the bonds with hydrogen atoms were fixed to the force field equilibrium values by the LINCS algorithm [175].

For the NVT-ensemble (canonical ensemble) simulations we used the Berendsen thermostat with the reference temperature of 300K and the relaxation time of 2.0 *ps* in the case of “production run” and 1.0 *ps* in the case of “equilibration run”. For the NPT-ensemble (isothermo-isobaric ensemble) simulations we used the Berendsen thermostat and also the Berendsen barostat. In this case the system was coupled to an external pressure of 0.1013 *MPa* with the relaxation time of 2.0 *ps*.

4) Systems preparation and collection of statistics.

1600 NMP molecules, 27 Na^{+} ions and 27 I^{-} ions were placed inside the simulation box with the help of Packmol program [176]. The initial configuration was firstly optimized by the energy minimization [167], and then the density of the system was equilibrated during a 0.2 *ns* simulation in the NPT-ensemble. We collected statistics over 60 *ns* simulation run in the NVT-ensemble at 300K. Coordinates of the system were sampled each 0.3 *ps* for further analysis.

To analyze molecular mechanisms of ion solvation in NMP, we performed an additional simulation of the NaI solution in bulk NMP (without the CNT) using similar simulation setup to the one described above. The pure NMP-NaI solvent system contained 610 NMP molecules, 18 Na^+ ions and 18 I^- ions. The system was simulated during 100 *ns* of simulation time in NVT-ensemble.

5) Details on the calculation of radial density profiles.

The radial density profiles (RDPs) of different species were calculated and normalized in the same way as in the case of aqueous solutions (see Section 4.1.1). We have chosen a region on each RDP where it reaches a plateau (in our case 2.5 $nm < r < 3.0\ nm$) to correct the RDPs for the excluded volume of the CNT. We averaged the RDPs over this region and correspondingly rescaled the RDPs (divided by the mentioned value). On the Figure 31 of the main text the scaled RDPs are shown. The bulk number density of salt was estimated as the density of the bulk solvent in the cylindrical shell 2.5 $nm < r < 3.0\ nm$, and it was 0.114 $ion\ pairs/nm^3$.

4.2.2 Ion solvation in the bulk NaI – N-methyl-2-pyrrolidone solution

In our simulations we observe that ions dissolved in NMP have distinct solvation shells (See Figure 29). That was expectable, because NMP is a very polar solvent (the dipole moment is about 4.1 Debye) and, therefore, the NMP molecules strongly interact with the dissolved ions due to the electrostatic charge-dipole interactions.

Both of the ion-NMP radial distribution functions show a peak (at r=0.42 and r=0.55 *nm* for Na^+ and I^-, respectively) followed by a hollow (at r=0.50 and r=0.70 *nm* for Na^+ and I^-, respectively), indicating formation of the first solvation shell around the ions [2]. The boundaries of the ion solvation shell were estimated as the region with non-zero ion-NMP radial distribution function ending at the first distinct minimum on the corresponding function. The structures of the solvation shells of the ions are different: the negatively charged NMP oxygen atoms are strongly attracted to the positively charged sodium ions (see the snapshot illustrating typical configuration of NMP molecules around this ion on Figure 29A); from another side, the oxygen atoms are placed outwards the negatively charged iodide ions (see the molecular snapshot on

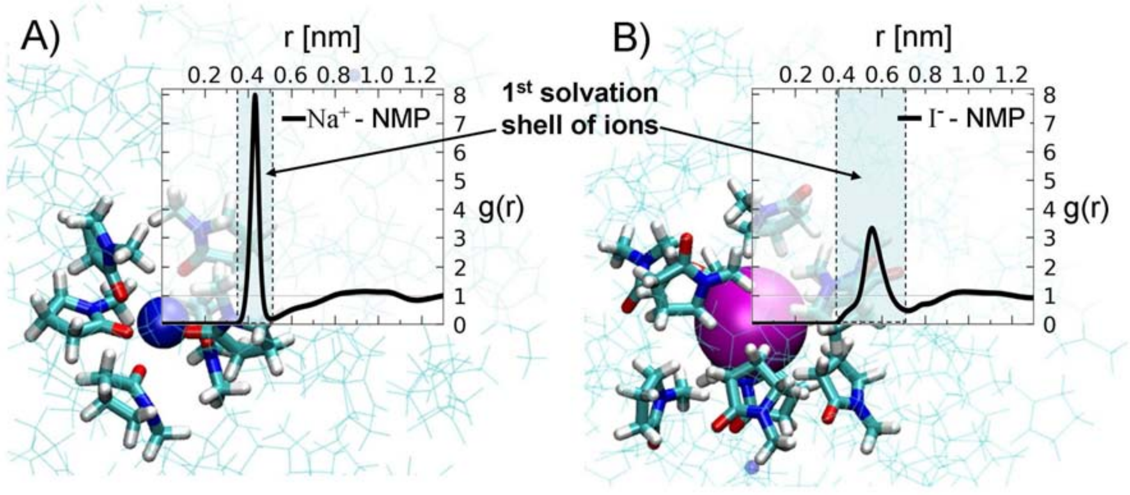

Figure 29: Ion-NMP (center of mass) radial distribution functions, g(r), in NaI-NMP solution combined with corresponding simulation snapshots: A) sodium ion (shown as a blue sphere), B) iodide ion (shown as a magenta sphere). The highly noticeable peaks on the g(r) functions indicate distinct solvation shells around the ions. On the simulation snapshots the NMP molecules in the first solvation shell around the ions are represented by thick sticks. The oxygen atoms in these molecules are colored by red, nitrogens by blue, carbons by cyan and hydrogens by white. Other molecules are shown by thin cyan lines.

Figure 29B). In general, similar to the mechanisms of ion solvation in water [73, 101] there is a strong asymmetry in sodium and iodide solvation in NMP. As illustrated by the high peak on Na^+-NMP g(r) (Figure 29), the sodium ion solvation shell is very dense because the ion is relatively small and, consequently, has a large surface charge density [106]. Therefore, the Na^+ ions strongly coordinate polar solvent molecules around them that resulted in the height of the first peak on Na^+-NMP radial distribution function to be about 8.0. On the other hand, the iodide ion solvation shell is much more diffuse because of the larger size of the I^- ion and, consequently, its smaller surface charge density than of the Na^+ ion [106]. As a result, the height of the first peak on I^--NMP radial distribution function is much smaller than the one on the Na^+-NMP RDF (it is slightly above 3.0). The position of the first maximum on the I^--NMP RDF is also shifted compared to the Na^+-NMP RDF (from 0.42 *nm* to 0.55 *nm*). This is because of two main reasons: (i) I^- (r = 0.220 *nm*) has larger radius compared to Na^+ (r = 0.102 *nm*); (ii) as discussed above, the I^--NMP interactions are weaker than the Na^+-NMP interactions (the ionic radii are taken from Ref. [103] as presented in Ref. [2]).

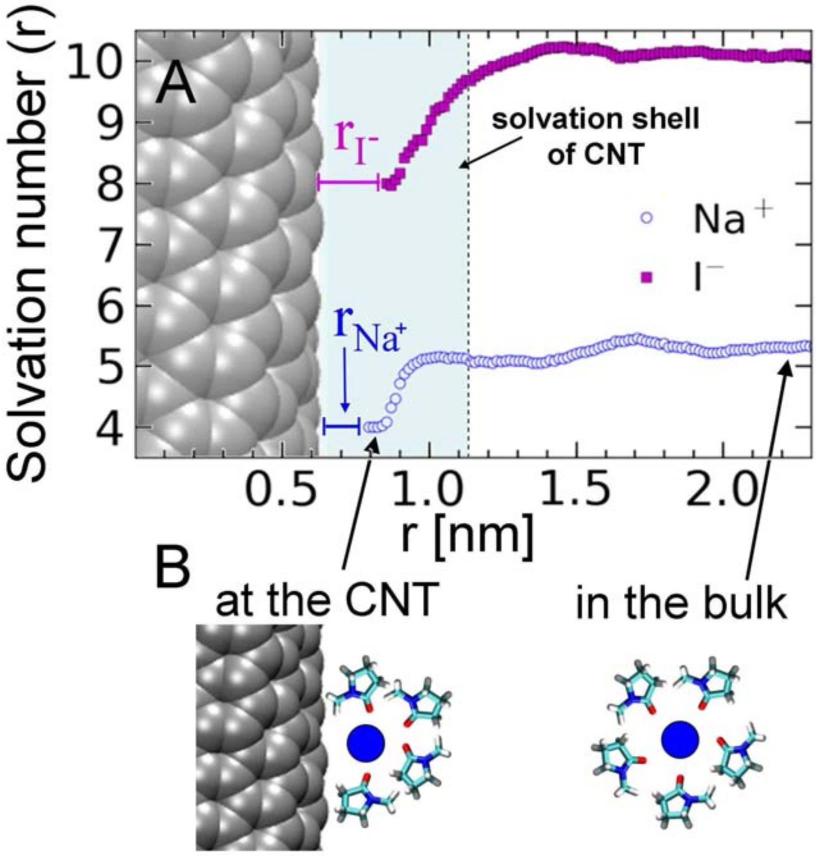

Figure 30: A) Solvation number of ions (the number of NMP molecules in the first solvation shell of the ions) as a function of distance from the CNT. B) Schematic representation of the partial desolvation of the ions upon the direct contact with the CNT surface. Because the iodide ion is larger than the sodium ion it consequently has larger solvation number.

4.2.3 Ions behavior at the carbon nanotube surface in N-methyl-2-pyrrolidone dispersion

Results of our MD simulations indicate two major effects which take place during ion interactions with the CNT surface:

1) Firstly, ions have to become partially desolvated to make direct contacts with the CNT surface (see Figure 30). The partial desolvation of ions at the CNT surface happens because of the steric restraints caused by the surface. The MD simulations show that upon approaching the CNT surface the sodium ions have to release *one* NMP molecule and the iodide ions have to release *two* NMP molecules from their solvation shells (there is a significant decrease of the solvation number of ions at the CNT surface see, see Figure 30 A). The partial desolvation of ions also means that the strong ion-NMP dipole interactions (discussed above) are substituted by the much weaker Van-der-Waals interactions of ions with the non-polar CNT surface. That leads

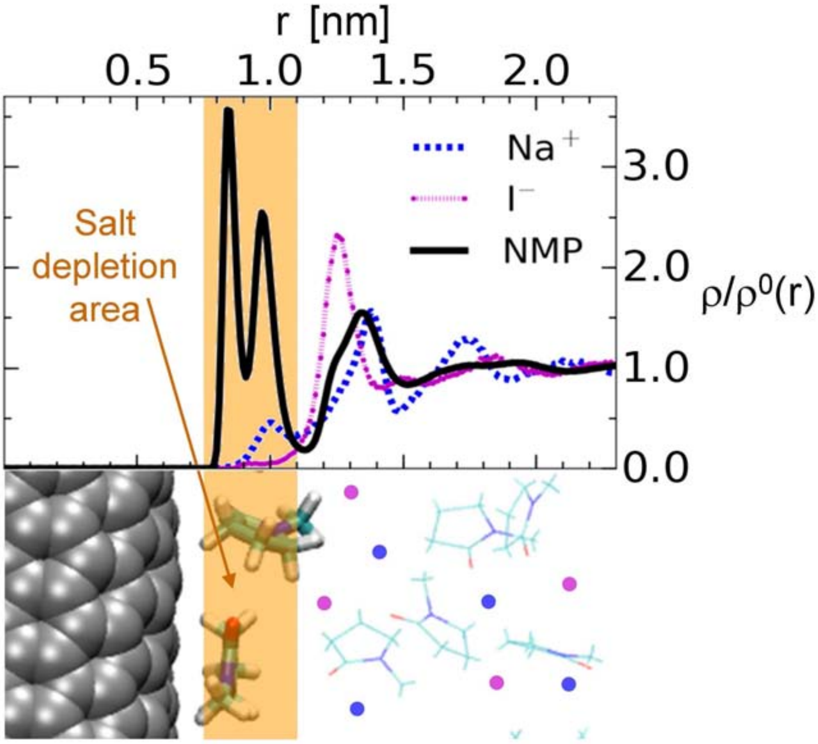

Figure 31: Radial density profiles of ions and NMP molecules (center of mass) around the CNT. There is a distinct salt depletion area at the CNT surface (marked by the beige color): a region with enhanced concentration of NMP molecules but with much lower concentration of ions than in the bulk. The simulation snapshot represents the NMP molecules in the first solvation shell of CNT (shown by thick sticks) preferentially having two different orientations, flat and perpendicular to the surface. These two preferential orientations correspond to the two distinct peaks on the NMP radial density profile. The NMP molecules outside the first solvation shell are represented as thin lines. The colored circles schematically show ions (Na$^+$ by blue and I$^-$ by magenta) in the solution.

to large energy costs for partial desolvation of ions (so-called desolvation penalty [177]) and, overall, makes the direct contacts of ions with the CNT surface to be energetically unfavorable.

2) Secondly, to approach the CNT surface, ions have to squeeze through a very dense layer of NMP molecules in the first CNT solvation shell (see Figure 31). Contrary to water, NMP is known to interact strongly with the surface of carbon nanomaterials [32]. The dense CNT solvation shell in NMP corresponds to a broad region on the CNT-NMP radial density profile with two distinct high peaks in the vicinity of the CNT surface (see Figure 31). This NMP enrichment area is followed by a deep hollow at about r = 1.1 *nm* (see Figure 31). Thus, during the formation of ion-CNT direct contacts, not only the ions have to become partially

desolvated (as shown on Figure 30), but also the CNT has to release some NMP molecules from its solvation shell. This further increases the energetic barrier for the formation of ion-CNT direct contacts.

To conclude, the energetic penalties in the processes of partial desolvation of ions and partial desolvation of CNT can not be compensated by the weak Van-der-Waals interactions of the ions with the non-polar CNT surface. As a result, ions prefer to stay in the bulk of the NMP solution rather than close to the CNT surface. This leads to a formation of ion *depletion area* around the non-polar CNT surface, where the concentration of ions is significantly lower than in the bulk solution (Figure 31). Geometrically, the *depletion area* roughly corresponds to the CNT solvation shell. The *depletion area* thickness is about 0.35 *nm*, which is about the width of one NMP molecule. Ions can attach to the CNT solvation shell beyond the *depletion area*, where there is even enhanced concentration of iodides nearby the boundary of the CNT solvation shell (Figure 31, area around $r \approx 1.1$ *nm*). The sodium ions can occasionally enter the CNT solvation shell (there is small but non-zero peak on the Na^+-CNT radial density profile at $r \approx 1.0$ *nm*, see Figure 31), while in the case of the iodide ions it happens very rare (I^--CNT radial density profile is almost zero at shorter distances to the CNT than $r \approx 1.1$ *nm*, see Figure 31).

To understand the main mechanisms of changes in Na^+ and I^- solvation upon approaching the CNT surfaces we analyzed the solvation number (the average number of NMP molecules in the first solvation shell of the ions) as a function of distance between the corresponding ion and the CNT surface (see Figure 30). As illustrated by this figure, the difference in the solvation strength of Na^+ and I^- results in different mechanisms of their penetration into the CNT solvation shell. Na^+ is strongly solvated, and therefore, it keeps its solvation number unchanged until it comes very close to the CNT surface (see Figure 30A). The Na^+ ions become (abruptly) partially desolvated only at the very vicinity of the CNT surface (Figure 30A, $r < 1.0$ *nm*) when this is absolutely unavoidable because of the steric constraints posed by the CNT surface. On the other hand, the iodide ion is much weaker solvated in NMP compared to Na^+. As a result, the I^- ions gradually loose NMP molecules from their solvation shell (starting from $r \approx 1.5$ *nm*) diving into the CNT solvation shell (see Figure 30A).

4.2.4 Comparison to aqueous solutions

Here we also would like to briefly compare the proposed mechanisms of ion interactions with the CNT surface in NMP solution to the previously discussed results on molecular simulations of ion-CNT interactions in aqueous solutions as well as ion interactions with other non-polar surfaces [178, 161]. It is shown in Ref. [161] that the probability of a direct ion contact with the CNT surface strongly correlates with the strength of ion hydration. The less hydrated is the ion the bigger is its concentration at the CNT interface, see Section 4.1, [179]. Such, the simulations in Ref. [179] show that the concentration of iodide at the CNT surface in aqueous solution is about 40% of its bulk concentration, while the interface concentration of sodium ions is practically zero. This is apparently not the case for NMP solutions, despite the fact that the strength of the ion solvation in NMP as well as the strength of ion solvation in aqueous solutions decreases from sodium to iodide. There are almost negligible concentrations of both Na^+ and I^- ions in the ion-CNT interface shell (see Figure 31). In NMP both sodium and iodide ions are depleted from the CNT surface. We attribute this to the fact that the CNT surface can be much easier dehydrated in water, than desolvated in NMP. The dense CNT solvation shell in the NMP solution prevents ions to come close to the surface, while in aqueous solutions ions do not have such a barrier.

On Figure 32A one can see that the CNT surface is much stronger solvated in NMP, compared to its hydration in water. In the NMP solution, there is a dense solvation shell around CNT which is represented by a broad region on the NMP radial density profile that consists of two distinct high peaks. In contrary, the water radial density profile has a much smaller height of the first peak and much less deep hollow, showing that the CNT hydration shell is much more diffuse compares to the NMP solvation shell. Thus, partial dehydration of CNT surface in water is much easier than the partial desolvation of CNT in NMP, where the barrier is large. The barrier of a solvent molecule exchange between the 1^{st} solvation shell and the rest of solution is more than 1 k_BT higher in the NMP solution compared to the aqueous solution (Figure 32B).

4.2.5 Thermodynamics of ion depletion at the carbon nanotube surface

To quantify the effect of the salt depletion area on the solvation thermodynamics of CNTs in CNT-NMP dispersions, we employ the Gibbs-Duhem relation (as described in Ref. [161]) and an approach based on the Kirkwood-Buff (KB) theory of solutions [180] as discussed in Ref. [181, 182, 183]. In general, within the framework of the KB theory of solution, the change in the chemical potential of a solute molecule (S) dissolved in a solvent (V), upon addition of a cosolvent (X) is written as [161]:

$$d\mu_S = -\Gamma_{SX} \cdot d\mu_X, \tag{31}$$

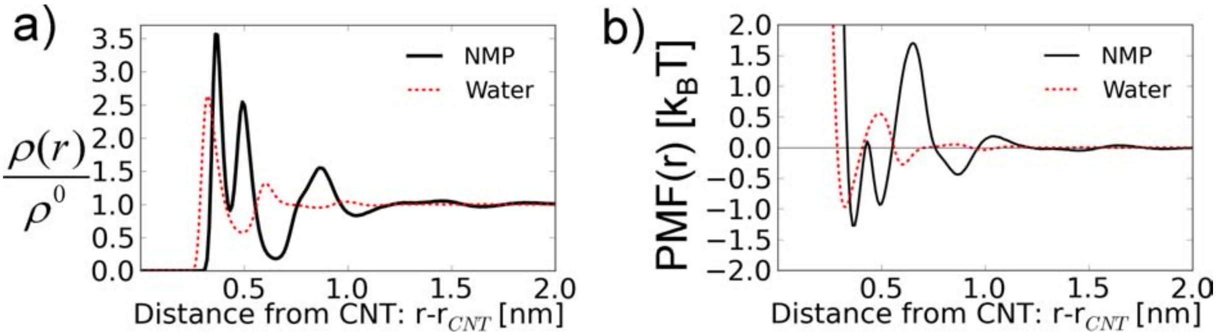

Figure 32: a) Radial density profiles of water (TIP4Pew model) and NMP (OPLS-AA parameters) around the CNT(7,0) and CNT(8.6) correspondingly. One can see that the CNT surface is much more strongly solvated in NMP, rather than hydrated in water. b) Potential of mean force of water (TIP4Pew model) and NMP (OPLS-AA parameters) around a CNT. One can see a high barrier of 2.6 k_BT preventing a free exchange of NMP molecules between the solvation shell of the CNT and the rest of solution. Contrary, in the aqueous solution the barrier of water exchange is only 1.5 k_BT. The PMFs were estimated as negative natural logarithms of the corresponding radial density profiles.

where $d\mu_S$ is the change in the chemical potential of solute, $d\mu_X$ is change of chemical potential of the co-solvent, Γ_{SX} is the solute - co-solvent preferential interaction coefficient (deficit or excess of the number of co-solvent molecules around a solute molecule, compared to the same volume of the bulk solution).

We substitute the differentials with the finite differences, and get the expression which can be used in our calculations:

$$\Delta\mu_S \approx -\Gamma_{SX} \cdot \Delta\mu_X \tag{32}$$

The solute - co-solvent preferential interaction coefficient can be calculated within the Kirkwood-Buff theory of solutions [181, 184]:

$$\Gamma_{SX} = -\left(\frac{\partial\mu_S}{\partial\mu_X}\right)_{T,P,n_2} = \rho_X\left(G_{SX} - G_{SV}\right) \tag{33}$$

where ρ_X is the number density of species X, G_{SX} and G_{SV} are Kirkwood-Buff (KB) integrals for species S and X, S and V respectively.

Initially the KB integral for any particles (let call them A and B) was defined via a molecule-molecule radial distribution function $g_{AB}(r)$ [94]. A straightforward generalization for molecule-molecule pair correlation function ($g_{AB}(\mathbf{r})$) defined in 3D coordinate space would be (following

Reference [184]):

$$G_{AB} = \int_V (g_{AB}(\mathbf{r}) - 1)\, d\mathbf{r} \tag{34}$$

where V defines the whole “phase volume” of the $\mathbf{r}$ coordinate.

Because CNT (S) has spherical symmetry, we rewrite the KB integral (Equation 34) in cylindrical coordinates through the radial density profile $\frac{\rho_{SX}(r)}{\rho_X^0}$:

$$G_{SX} = \int_0^{\infty} \left(\frac{\rho_{SX}(r)}{\rho_X^0} - 1 \right) 2\pi r \cdot dr \tag{35}$$

where $\rho_{SX}(r)$ is the number density of particles X as a function of the distance r from the axis of cylindrical symmetry of CNT (S), ρ_X^0 is the number density of cosolvent X in bulk solution, the integration is performed in cylindrical coordinates, $2\pi r \cdot dr$ is the volume of cylindrical segment (the length of the cylinder is implied to be 1 nm).

Changing of the letter X to the letter V in Equation 35 would give the expression for the KB integral of solvent around CNT. Thus, the solute – co-solvent preferential interaction coefficient can be calculated via the radial density profiles of the corresponding species in the solution:

$$\Gamma_{SX} = \rho_X^0 \int_0^{\infty} \left(\frac{\rho_{SX}(r)}{\rho_X^0} - \frac{\rho_{SV}(r)}{\rho_V^0} \right) 2\pi r \cdot dr, \tag{36}$$

where $\left\{\rho_X^0, \rho_V^0\right\}$ are the number density of particles X and V correspondingly in the bulk solution, $\{\rho_{SX}(r), \rho_{SV}(r)\}$ are the densities of particles X and V as a function of the distance r from the axis of cylindrical symmetry of CNT (denoted by the index S).

Following the works (Ref. [185]) we applied the Kirkwood-Buff theory for estimating the preferential interaction coefficient of the NaI salt as a cosolvent around CNT. There is a peculiarity in the Kirkwood-buff theory dealing with the electrolyte solutions [94]. The KB theory is developed for open systems. But in an open system, one can not consider ions of the dissociated salt as independent components, because of the electro neutrality condition. Thus an additional restriction must be applied and the KB theory cannot be used in a straightforward way. Kusalik and Patey described a rigorous way how to overcome the problem manipulating with the KB theory equations in reciprocal (Fourier) space [186]. Chitra et al. [185] showed that these results of Kusalik and Patey are equivalent to the following “physical picture”: considering ions as indistinguishable particles. Thus in this study we consider the indistinguishable ions as a co-solvent. Following the work of [161] we estimated the RDP of the “indistinguishable ions“

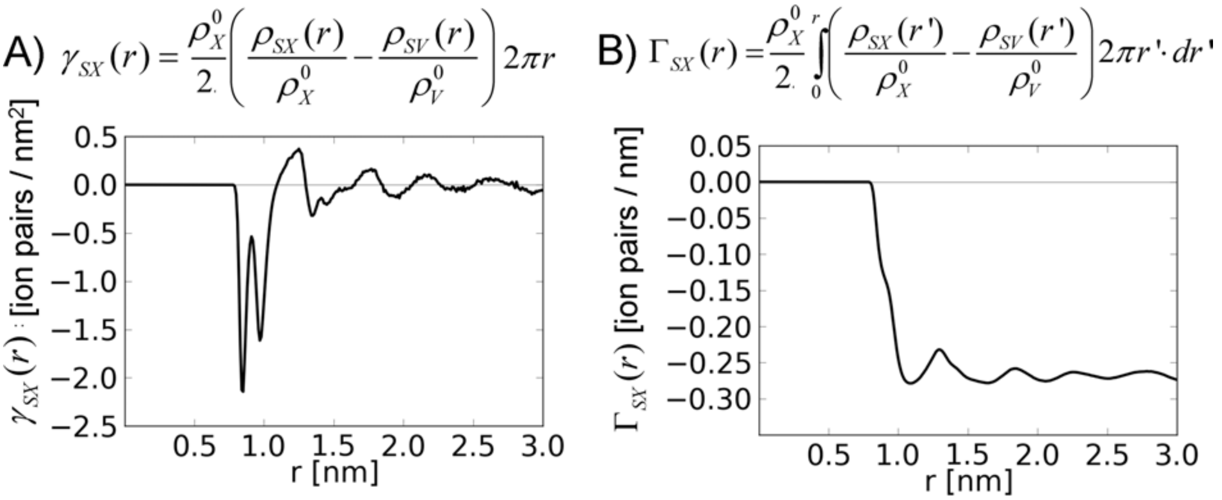

Figure 33: The calculated preferential interaction coefficient of salt for 1 nm of the CNT length. A) Integrand function in Equation 36; B) Preferential interaction coefficient as a function of distance (running integral of Equation 36). Te value of Γ_{SX}, used in further calculations, was set to $\Gamma_{SX} = -0.273$ *ion pairs / nm of CNT length.* We consider the "indistinguishable ions" of NaI salt as a co-solvent X, thus to get the dimensions of *ion pair* we divided the ρ_X^0 by two.

as an arithmetic mean of the contributions coming from the sodium and iodide RDPs:

$$\frac{\rho_{SX}(r)}{\rho_X^0} = \frac{1}{2}\left(\frac{\rho_{SNa^+}(r)}{\rho_{Na^+}^0} + \frac{\rho_{SI^-}(r)}{\rho_{I^-}^0}\right) \tag{37}$$

The bulk density of cosolvent ρ_X^0 is the sum of bulk densities of individual ions.

The preferential interaction coefficient evaluated by Equation 36 is illustrated in Figure 33. The changes in the chemical potentials of co-solvent and solvent in the bulk solution are related by the following Gibbs-Duhem equation [161]:

$$d\mu_X = -\frac{x_V}{x_X} \cdot d\mu_V \tag{38}$$

$$\Delta\mu_X \approx -\frac{x_V}{x_X} \cdot \Delta\mu_V \tag{39}$$

where x_X and x_V is the mole fraction of species X and V in bulk solution.

Change of the chemical potential of solvent upon the co-solvent addition can be written as [161]:

$$\Delta\mu_V = k_B T \ln(a_V) \tag{40}$$

where k_B is the Boltzmann constant, T is temperature, a_V is the activity of the solvent.

Since in our case we have a diluted solution (0.15M), we may assume that the activity of the solvent is equal to the mole fraction of solvent: $a_V \approx x_V$. Considering cosolvent as indistinguishable ions we can estimate the mole fraction of solvent: $x_V = \frac{1600}{1600+27\cdot 2}$. Thus, the change of the chemical potential of solvent upon the co-solvent addition can be estimated: $\Delta\mu_V / k_B T \approx \ln(x_V) = -0.0332\ k_B T$. Following the Equation 39: $\Delta\mu_X \approx -\frac{1600}{2\cdot 27} \cdot (-0.0332) = 0.984\ k_B T$.

The calculations using the Equation 32 show that the increase of the CNT surface free energy by addition of the NaI salt into CNT-NMP dispersion is about 0.09 $k_B T$ per nm^2 of the CNT surface at 300K. Note, the final value calculated by the Equation 32, is then normalized by the surface of the CNT of 1 nm length ($S = 2\pi r_{CNT}$, where the radius of (8,6) CNT $r_{CNT} = 0.478\ nm$). The value is positive indicating an increase of the CNT solvophobicity upon the salt addition. Analyzing the described expressions, we can estimate how an increase of salt concentration would affect the thermodynamic stability of the CNT-NMP dispersions. The combination of the above mentioned formulas gives the following relation of $\Delta\mu_S$ and the salt concentration x_X:

$$\Delta\mu_S \approx -\Gamma_{SX} \cdot \Delta\mu_X \approx \Gamma_{SX} \cdot \frac{x_V}{x_X} \cdot \Delta\mu_V \approx \Gamma_{SX} \cdot \frac{x_V}{x_X} \cdot k_B T \ln(x_V) \approx \Gamma_{SX} \cdot \frac{1 - x_X}{x_X} \cdot k_B T \ln(1 - x_X) \quad (41)$$

Assuming that the particle radial density profiles do not change much with the increase of salt concentration (for little salt concentrations this is a reasonable approximation), we may assume that the integral in Equation 36 is constant and that the preferential interaction coefficient is proportional to the salt concentration, so $\Gamma_{SX} \approx C \cdot x_X$, where the C is a *negative* (C<0) constant (see above), x_X is the mole fraction of salt in NMP. For small salt concentrations used in our experiments (1-10 mM) we also may assume $\ln(1 - x_X) \approx -x_X$ and $(1 - x_X) \approx 1$. We get the following relation:

$$\Delta\mu_S \approx C \cdot k_B T \cdot (-x_X) \quad (42)$$

Minding the *negative* constant C, we may conclude that with the increase of the salt concentration, $\Delta\mu_S$ increases (becomes more positive), and, therefore, the CNT becomes more solvophobic.

The results of our simulations and simple analysis of thermodynamic relations reveal that an increase of the salt concentration increases the CNT solvophobicity in CNT-NMP dispersions. This originates from the formation of the ion depletion area around CNTs, and that in turn results in an increase of the free energy of CNTs in NMP dispersions. These thermodynamic changes should make the CNT-NMP dispersions less stable with the increase of the salt concentration. That means that CNTs can easier interact with each other forming CNT aggregates and bundles, decreasing the total CNT surface exposed to the salt NMP solutions. We refer to this effect as “salting out” of CNTs from CNT-NMP dispersions.

We think that the mechanism of “salting out” of CNTs from NMP dispersions resulted from the analysis of the simulation data in the current work has a similar origin to the well known “salting out” effects in aqueous solutions, which are widely used in biotechnology for coagulation and separation of biomolecules from aqueous solutions as well as for protein crystallization [178].

4.2.6 Discussion of the simulation results in light of experimental data

To verify the general trends predicted by the simulations, our colleagues in Aston university performed a series of experiments on the salting out of CNTs from CNT-NMP dispersions. The CNTs (SWeNt CG100, Lot # 000-0012) were dispersed in neat N-methy-2-pyrrolidone (NMP; spectrophotometric grade, ≥ 99%, Sigma-Aldrich) via ultrasonication (20 *KHz*, 200W, 1 *hour*) with Nanoruptor sonicator (Diagenode). The dispersion was subjected to ultracentrifugation (2.5 *hours*; $17^{o}C$; 47 000 *RPM*) using MLS 50 swinging bucket rotor in the Optima Max XP ultracentrifuge (Beckman Coulter). The resulting CNT dispersion was divided on 5 samples which we number as sample 0, 1, 2, 3 and 4 correspondingly. The sample 0 was used as a control sample (without salt). Four different salt concentrations were put (0.1, 0.5, 1 and 10 mM) into the other samples. The final concentrations of the salt in the samples were prepared as follows. Predefined amount of concentrated salt (NaI; ACS reagent, ≥ 99.5; Sigma-Aldrich) solution in NMP was added to each sample with a calibrated micropipette. All samples were exposed to shaking at 300 *rpm* for 10 *min*. Due to the small volume of the added drops of the concentrated salt solution we did not take the dilution into account. The final salt concentrations were 0.1, 0.5, 1 and 10 mM that correspond to the samples 1, 2, 3, and 4.

We note that in the simulations we used higher concentrations of salts than in our experiments to make the simulations feasible (at lower salt concentrations it is difficult to collect enough statistics). However, we think that the main molecular mechanisms of ion interactions with the nanotube surface remain the same (at least *qualitatively*) also at lower concentrations used in our experiments.

The changes in the CNT dispersions in response to addition of different amounts of salt were investigated by using PhotoLuminescence (PL) spectroscopy and optical absorption spectroscopy as well as by visual inspection of the samples. We use PL spectroscopy as a tool for monitoring the presence of isolated SWNTs and their small bundles in the dispersions [88, 90].

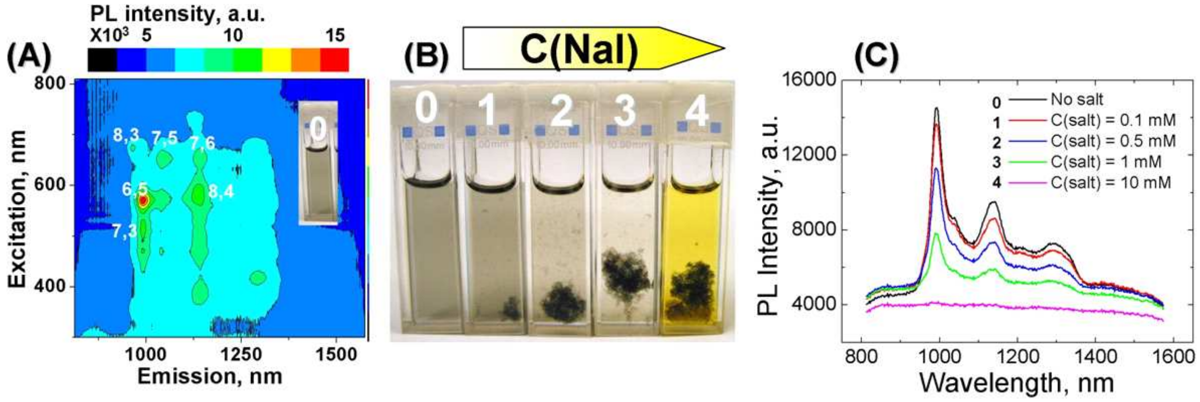

Figure 34: (A) PL map of the control sample (a stable CNT-NMP dispersion); (B) the control sample and samples with salt (NaI) addition aged for 5 hours. 0 - control (no salt), 1 - 0.1 mM; 2 - 0.5 mM; 3 - 1 mM; 4 - 10mM of NaI; (C) PL spectra of the control sample and samples with salt (NaI) addition at excitation wavelength 570 nm.

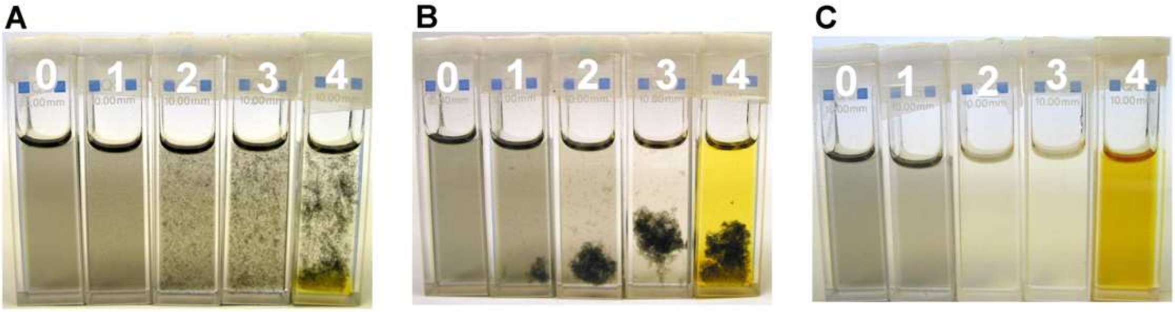

Figure 35: Photographs of the samples containing the CNT-NMP dispersions with different amounts of added salts: A) 15 minutes upon the salt addition; B) 5 hours upon the salt addition; C) samples after ultracentrifugation.

We assume that the concentration of nanotubes within the sample correlates with the intensity of the PL bands and optical absorbance for the corresponding nanotube chiralities. That allows us to make quantitative analysis of the changes in the dispersions upon additions of salt.

Different quantity of inorganic salt (NaI) were added to CNT dispersion in NMP. After 15 min upon the salt addition we observed formation of CNT bundles (see Figures 34B, 35). The quantity of the bundles increases with the increase of the salt concentration. The formed bundles stay insoluble in time and can be removed from the dispersion.

The PL spectra of the control CNT-NMP dispersion presented on Figure 34A. A significant drop in the PL intensity upon the salt addition indicates a decrease of the CNTs concentration in dispersions [88, 90] (Figure 34C). At salt concentrations of 0.1mM and 0.5mM a certain

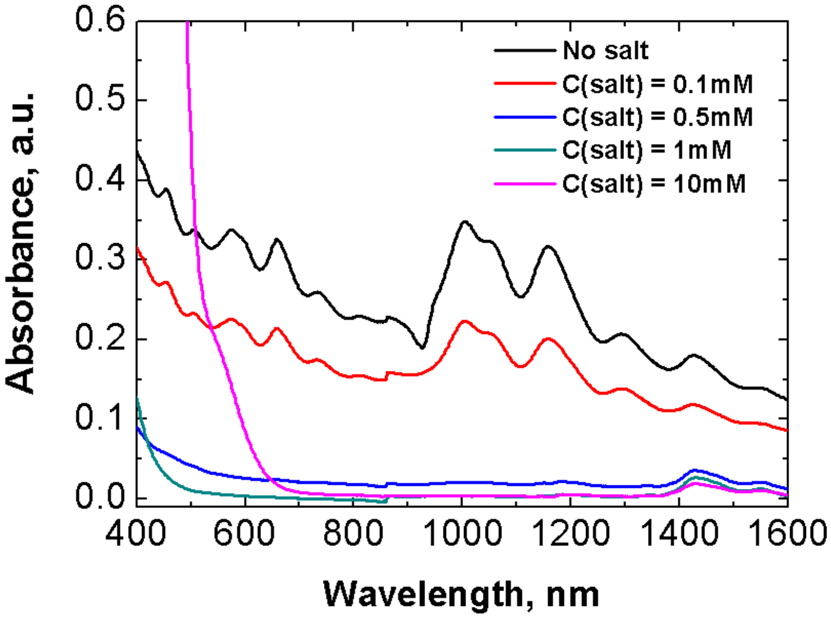

Figure 36: Absorption spectra of the CNT-NMP dispersions with different salt concentrations after an additional centrifugation. The centrifugation removes big CNT bundles from dispersion. For NaI concentrations above 0.5mM the spectra show practical absence of CNTs in the dispersions after the additional centrifugation that corresponds to complete "salting out" of CNTs from dispersions (note: the high increase of the intensity of the 10 mM spectra in the area of 400-700 *nm* is caused by the high concentration of NaI, not by CNTs).

concentration of CNTs remains in the dispersion. However, the concentrations higher than 1mM apparently lead to complete precipitation of all CNTs in the dispersion. We note that in the case of the control “no salt” sample (0) the additional centrifugation almost does not affect the PL intensity. This is a clear illustration that the decrease in the PL intensity for other samples is caused by the addition of salt, rather than aging of the dispersions.

The experiments show that the concentration of the CNTs in the dispersion can be regulated by the quantity of added salts. Indeed, there is a monotonic drop in the PL intensity with the increase of the salt concentration (Figure 34C).

Absorption spectroscopy allows determining the overall concentration of CNT in dispersion. We used this method to support our PL data. Absorption spectroscopy measurements show the same general trend: the intensity drops with the increase of the salt concentration (see Figure 36).

The experimental data clearly show that it is possible to “salt out” carbon nanotubes from their NMP dispersions. The “salting out” effect is observed already at very small concentrations of NaI salt (range of mM). The degree of CNT aggregation monotonically increases with the increase of the salt concentration, indicating an enhancement of the CNT solvophobicity in the CNT-NMP dispersions. Thus, the conclusions coming from the computer simulation and general physico-chemical principles of salt effects discussed in the paper are confirmed by direct experiments on the CNT precipitation by salts.

4.2.7 Conclusions

The analysis of the simulation and experimental data on sodium iodide salt effects on CNT dispersions in NMP results in the following conclusions:

1. To make the direct contacts with the CNT surface in CNT-NMP dispersion, ions have to become partially desolvated. The partial desolvation is energetically unfavorable because of the strong ion-solvent interactions in highly polar NMP solution.

2. The CNT itself has a very distinct and dense solvation shell in the NMP solution, and that adds an additional barrier for ions to come close to the CNT surface.

3. As a result of the unfavorable interactions of ions with the CNT surface, a salt depletion area is formed around the CNT, where the concentration of ions is much less than in the bulk solution. The width of the salt depletion area corresponds to the width of the first solvation shell of CNT in NMP.

4. The preferential depletion of ions from the CNT-NMP interface results in increase of the solvophobicity of the CNTs in the CNT-NMP dispersions with the increase of the salt concentration. As a consequence, the CNT-NMP dispersions become thermodynamically less stable at higher concentrations of salts.

5. The increase of the CNT solvophobicity upon the salt addition was confirmed by direct experiments in a collaboration with our colleagues in Aston university. Different amounts of NaI salt were added to the prepared CNT dispersions in neat NMP and the precipitation of the CNTs was observed. The degree of the precipitation increased with the increase of salt concentration, which is in line with the results of the theoretical and simulation part of the study.

We believe that the revealed mechanisms of the ion interaction with the CNT surface in non-aqueous (NMP) dispersions should bring new insights on salt effects on nanotubes in non-aqueous solutions [187]. We show that the ‘salting out’ effect leads to an efficient safe and inexpensive method of regulating the CNT concentration in non-aqueous dispersions. We hope that the results of the paper can be useful for rational development of new methods for processing of liquid dispersions of carbon nanomaterials based on the “salting out” effect in non-aqueous media.

4.3 Interaction of molecular ions with the carbon "nanoonion" surface in organic salt/acetonitrile solutions

In this section we study basic mechanisms of CNT interactions with two organic electrolytes: tetraethylammonium tetrafluoroborate (TEA-BF_4) and tetrabutylammonium tetrafluoroborate (TBA-BF_4) dissolved in acetonitrile (AN).

The tetraethylammonium salt solution in AN is widely used as electrolyte in electrical double layer capacitors (EDLC) [36]. In the EDLC the energy is stored due to the compensation of the potential on the electrode by the formation of the electric double layer (EDL). Such capacitors have several advantages compared to batteries: 1) the absence of redox reactions makes the EDLC stable for a much larger number of the charge-discharge cycles, 2) charging and discharging performs with high rates. Disadvantage is that the capacitance of EDLC is still by order lower than the capacitance of the Li-ion batteries [36].

There are two main ways to improve the performance of the EDLC. The first one is to adjust the properties of the electrolyte. The electrolyte for EDLC should be non-viscous, possess high conductivity, be stable up to high voltages, should allow the formation of the effective EDL to compensate the potential on the electrodes. The use of AN as a solvent for the EDLC electrolyte is convenient, because AN does not decompose up to relatively high voltages, while aqueous electrolytes have a very narrow electrochemical window of 1.2 V [37]. Tetraalkylammonium BF_4 salts are well soluble in AN, which allows to have electrolyte with large number of dissolved ions. The tetraethylammonium salt solution in AN as electrolytes in EDLC are well studied both experimentally [36] and theoretically [188]. It would be interesting to investigate how the change of the length of the alkyl chains of the tetralkylammonium ions affect the structure of the EDL.

The second way to improve the performance of the EDLC is to optimize the material for the capacitor electrodes [36]. Recently, it has been shown that the onion-like carbons (carbon "nanoonions", CNOs) are superior to commonly used carbon materials for capacitive performance of the EDLC [5, 36]. This phenomena is attributed to the fact that, for the same surface area, there are not many small pores in the structure of the CNO, where the electrolyte can be trapped [5] causing the diffusion limitations for ions. But still only limited information is available about the ion interactions with the CNO surfaces in aqueous or organic electrolytes [5, 36]. Thus, insights on the molecular level effects at the CNO surfaces at different surface charge densities would be very beneficial for rational design and optimization of new materials for the EDLC.

4.3.1 Simulation details

Systems under the investigation Molecular Dynamics (MD) simulations were performed with Gromacs 4.5.1-4.5.3 package [167]. As a model of a carbon "nanoonion" we took three carbon fullerenes of different size: C720, C320, C60 (the numbers represent the number of carbon atoms in the fullerenes). The diameter of the model "nanoonion" was about 2.5 nm (see Figure 1).

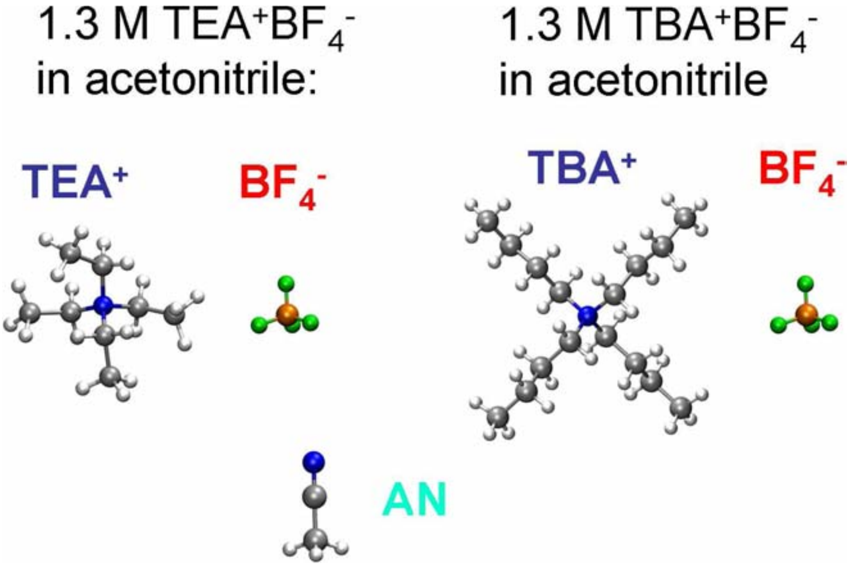

Figure 37: Electrolytes for the carbon "nanoonion" simulations.

The "nanoonion" was solvated in acetonitrile (AN) which contained a dissolved organic salt: tetraethylammonium (TEA) or tetrabutylammonium (TBA) tetrafluoroborate (BF_4) with molar concentration of 1.3 M (see Figure 37). We have performed simulations with different surface charge densities on the model carbon "nanoonion": 0, 0.5 and -0.5 e/nm^2 (0.5 e/nm^2 corresponds to 3.1 C/cm^2).

Topology and potential parameters. The initial structures of the fullerenes were taken from the the M. Yoshida database of the Nanotube Modeler (JCrystalSoft). The positions of the "nanoonion" atoms were restrained to the initial values by harmonic potential with 1000 $kJ\ mol^{-1}\ nm^{-2}$ force constant in each direction. Nonbonded interaction parameters for "nanoonion" carbon corresponded to the benzene OPLS-AA (all-atom optimized molecular potential for liquid simulation) carbon (opls_145 in Gromacs notation) [127]. For the simulation with the 0.00 e/nm^2 surface charge density on "nanoonion" the partial charges on carbon atoms were set to zero. For the simulation with the 0.5 and -0.5 e/nm^2 surface charge densities the partial charges on carbon atoms belonging to the outer surface of the "nanoonion" (fullerene C720)

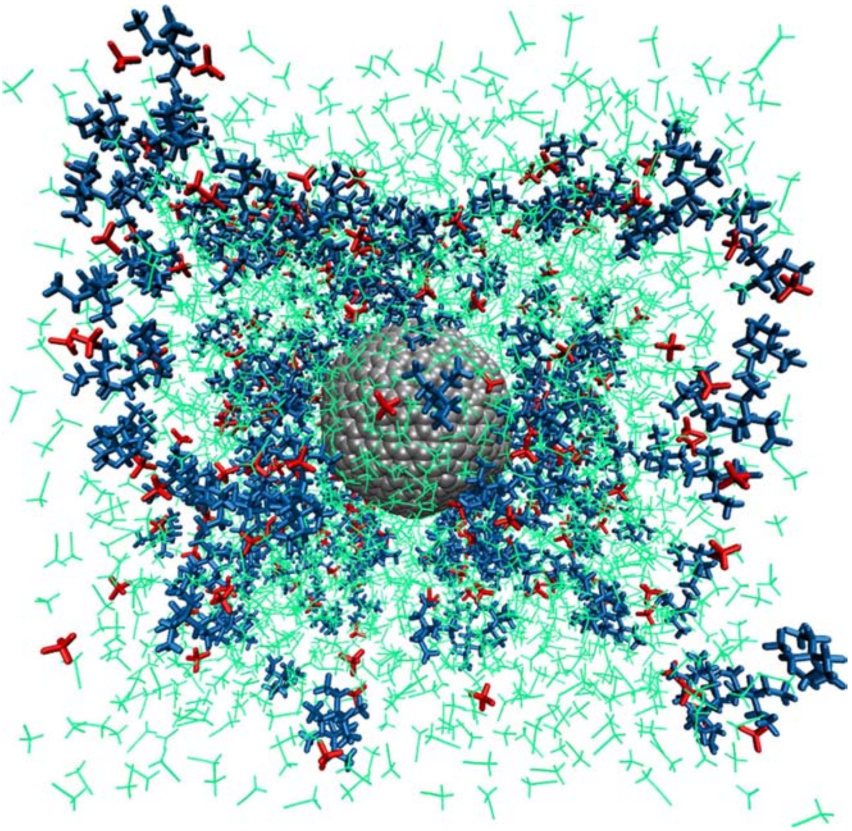

Figure 38: An example simulation box. The "nanoonion" is represented by grey balls, acetonitrile by green sticks, TEA$^+$ by blue and BF$_4^-$ by red thick sticks. The simulation box size is 6.9 x 6.8 x 6.9 nm.

were set to 0.015 *e* and -0.015 *e* respectively. The equilibrium values for the structural parameters of the bonded interactions (bond lengths, angles) were taken from the initial values in the corresponding structures, while the force constants for the bond and angle harmonic potentials were adopted from the OPLS-AA force field.

The OPLS-AA potential parameters [169, 127] were assigned to AN, TEA$^+$, TBA$^+$ and BF$_4^-$ molecule (molecular ions) with the use of the Maestro software [173].

MD algorithms details. We used the leap-frog integrator with 0.002 ps integration time step. For the Lennard-Jones potential we used 1.00 nm cut-off radius. The neighbor list for the nonbonded interactions was updated each integration step (since it was found that the neighbor list update might not work correctly in some versions of the Gromacs software). For accurate evaluation of the long range Coulomb interactions we used the Particle Mesh Ewald method [112]. For the systems with the non-zero surface charge density in the "nanoonion" we used the uniform background charge distribution of the opposite sign to compensate the non-zero charge of the system.

For the NVT-ensemble (canonical ensemble) simulations we used the "v-rescale" thermostat [189, 174] with the reference temperature of 300K and the relaxation time of 2.0 ps in the case of "productive run" and 1.0 ps in the case of "equilibration run". For the NPT-ensemble (isothermo-isobaric ensemble) simulations we used the Berendsen barostat [138]. In this case the system was coupled to an external pressure of 0.1013 MPa with the relaxation time of 1.0 ps.

Systems preparation and collection of statistics. Initial configurations for the MD simulations were generated with the PackMol program [176]. 2400 AN molecules, 244 TEA^+ and 244 BF_4^- ions (1720 AN molecules, 244 TBA^+ and 244 BF_4^- ions) were distributed in 7.5 x 7.4 x 7.4 nm^3 box. The "nanoonion" was placed in the center of the simulation box. The initial configurations were optimized with the energy minimization simulations, equilibrated with 50 ps of the simulation time in NVT ensemble, then 1 ns of simulation time in NPT ensemble. The production run was performed in the NVT-ensemble for at least 37 ns. Coordinates of the system were sampled each 0.2 ps for the further analysis.

4.3.2 Structure of the carbon "nanoonion" interface shell

Figure 39 shows the distributions of molecular ions around the "nanoonion". For neutral "nanoonion" (σ=0.0 e/nm^2) there is a slight preferential adsorption of the molecular cations against anions for both electrolyte solutions (see Figure 39a). The TBA^+ and TEA^+ molecular cations are much bigger than the BF_4^- species and possess long non-polar alkyl groups, which are more likely to adsorb on the non-polar carbon "nanoonion" surface than the small highly charged anions.

At the neutral carbon "nanoonion" surface the adsorption of the TBA^+ ions is stronger compared to the TEA^+ ones: on the corresponding "nanoonion" - TBA^+ g(r) there are three peaks, against one peak on the "nanoonion" - TEA^+ g(r). This happens because the TBA^+ ions contain lengthier non-polar alkyl chains than the TEA^+ ions. The non-polar alkyl chains as well as the non-charged carbon "nanoonion" surface should be able to release easily the polar acetonitrile molecules from their solvation shells and, thus, to form direct contacts.

In turn, at the negatively charged carbon "nanoonion" surface the adsorption of molecular cations on the surface is stronger in the TEA^+-BF_4^- solution rather than in the TBA^+-BF_4^- solution (see Figure 39, second column). Indeed, the first peak on the TEA^+-"nanoonion" distribution function is higher and wider than the first peak on the TBA^+-"nanoonion" distribution function. We attribute this to the fact that the TBA^+ ions are much bigger than the TEA^+ ions

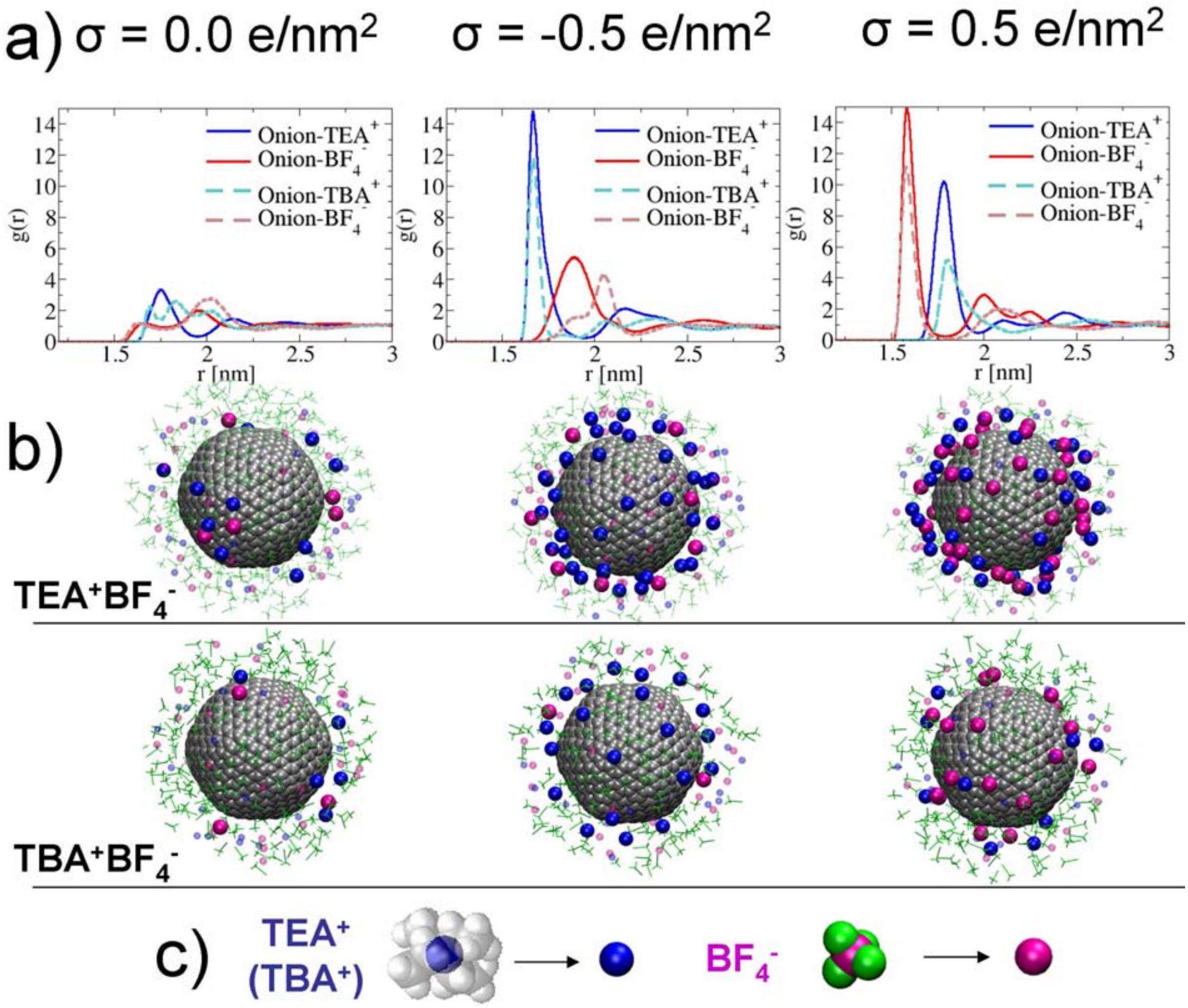

Figure 39: a) Distribution of particles around the carbon "nanoonions" for the three surface charge densities and two electrolytes (solvents): 1.3 M TEA$^+$-BF$_4^-$ and TBA$^+$-BF$_4^-$, both in acetonitrile; the distributions are calculated as center of mass - center of mass distributions of the corresponding molecular species. b) Snapshots from the corresponding simulations. Notation: molecular cations and anions are represented as blue and magenta spheres, respectively. Acetonitrile molecules are green lines. Only those molecules in the simulation boxes are represented which are within 1.0 nm from the "nanoonion" surface. Molecular ions which are within the range of 0.6 - 1.0 nm from the "nanoonion" surface are shown as transparent colored small balls, and which are within 0.6 nm from the "nanoonion" surface are represented as big opaque colored balls. c) Illustration of the used notations.

(see Figure 37) and as a result much less of them can occupy the same surface area of the "nanoonion".

Because of the relatively high concentration of organic salts (C=1.3 M) the interionic correlations of ions must be very strong, and can not be neglected in the description of the system.

Indeed, bulk solution cation-anion radial distribution functions (Figure 40) indicate that a strong pairing of ions in the solution occur: the first peak on the corresponding g(r)'s is relatively high. (Note: because of the interionic correlations the mean field models, like Debye-Hückel one, would fail to reproduce the properties of the system, thus, the use of the more computationally demanding Molecular Dynamics method is justified).

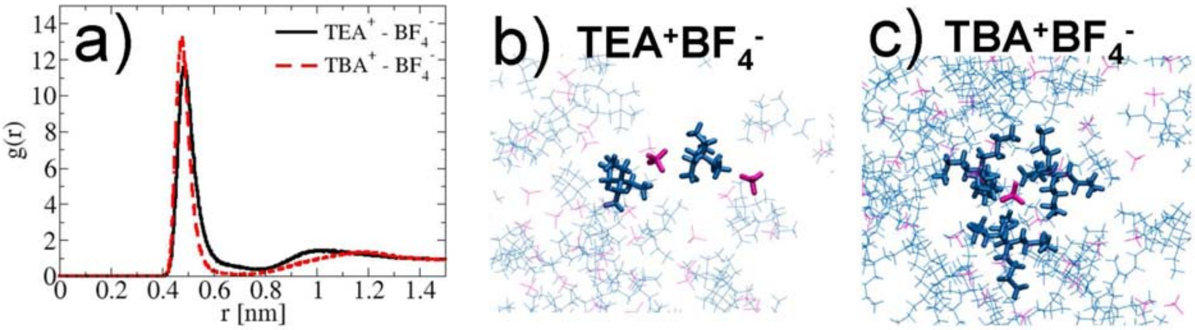

Figure 40: a) Distribution of particles in bulk solutions; b) Snapshot of the 1.3 M TEA$^+$BF$_4^-$ - acetonitrile solution simulation. Molecular cations are represented as blue, anions as magenta lines, acetonitrile is not visualized; c) The same as b), but for 1.3 M TBA$^+$BF$_4^-$ - acetonitrile solution.

The ion pairing is reflected in the ions distributions around the carbon "nanoonion" (Figure 40a), σ=0.0 e/nm^2). There is a peak on the "nanoonion"-anion g(r) after the first peak on the "nanoonion"-cation g(r) showing that the cations adsorbed on the "nanoonion" surface attract a large number of the molecular anions. The same picture, but more pronounced, can be seen on the particle distributions around negatively and positively charged "nanoonions" (see Figure 40a). For σ=-0.5 e/nm^2 there is a diffuse layer of the BF$_4^-$ ions attracted by the adsorbed molecular cations (there is a broad peak on the "nanoonion"-BF$_4^-$ g(r)). For σ=0.5 e/nm^2 the layer of the cations attracted by the adsorbed BF$_4^-$ ions is much more narrow.

For σ = 0.5 e/nm^2 the adsorption of BF$_4^-$ on the carbon "nanoonion" surface is stronger in the case of the TEA$^+$-BF$_4^-$ solution. Adsorbing to the surface BF$_4^-$ ions repel each other because they possess the same charge. But, since there is always a counterion close to the BF$_4^-$, the repulsion is decreased (screened out), especially when the counterion is placed somewhere in between two BF$_4^-$ ions (Figure 40b), as a result more BF$_4^-$ ions can come close to the surface. The screening of the electrostatic repulsion between BF$_4^-$ ions is more efficient by TEA$^+$ cations than by TBA$^+$, because the later have much bigger excluded volume and can not easily be places between BF$_4^-$ anions. As a result the adsorption of BF$_4^-$ ions at the positively charged surface is stronger for the TEA$^+$-BF$_4^-$ solution rather than for the TBA$^+$-BF$_4^-$ solution.

4.3.3 Conclusions

The main conclusion from this sections are:

1. In the case of the neutral carbon "nanoonion" surface, the increase of the non-polar alkyl chains of the tetraalkylammonium ions leads to an increase of the molecular cation adsorption on the carbon "nanoonion" surface.

   In turn, at high negative surface charge densities on the carbon "nanoonion" surface the concentration of the tetra*ethyl*ammonium ions is higher than the concentration of tetra*butyl*ammonium ions, which is attributed to the stronger sterical constraints for molecular packing of the tetra*butyl*ammonium ions.

2. The results indicate that the preferential adsorption of molecular ions at the CNM surface can be governed by varying the structure of molecular ions and/or applying an external electrostatic field.

3. The electrical double layer is not one-layer thick. The first layer of the ions in EDL attracts the large number of counterions. This results in the ion-counterion concentration "waves" around the carbon "nanoonions" in the organic electrolytes. Similar effects are described by Kornyshev, Fedorov et al. in Refs. [40, 62, 63].

4.4 Interaction of molecular ions with the carbon nanotube surface in room temperature ionic liquids/acetonitrile mixtures

In this section we study basic mechanisms of CNT interactions with several different TFSI-based (bis(trifluoromethylsulfonyl)imide) - based room temperature ionic liquids (RTILs) in their mixtures with acetonitrile (AN). To understand the effects of the cation molecular geometry on the properties of the interface structure in the RTIL systems, we investigate a set of three RTILs with the same anion (TFSI) but with different cations, namely, EMIm (1-ethyl-3-methylimidazolium), BMIm (1-butyl-3-methylimidazolium) and OMIm (1-octyl-3- methylimidazolium). The cations have identical charged methylimidazolium 'head' but different nonpolar alkyl 'tails' where the length of the tail increases from EMIm to OMIm.

We focus on the following questions:

- What is the interfacial structure of RTIL-AN mixture at the *neutral* CNT surface?
- How does the interfacial structure change at the *positively* charged CNT surface?
- How does the interfacial structure change at the *negatively* charged CNT surface?
- Does the length of the cation alkyl tails affect the interfacial RTIL-AN structure and preferential orientation of the RTIL ions at the CNT surface?
- What is the role of acetonitrile solvent in these interfacial effects?

We note, that in this study we would like to focus on the interface effects at the *outer* surface of CNT. In this study we use a CNT with (6,6) chirality which has a narrow pore. Taking into account the molecular volume of the investigated ions (see Table 5) we assume that the probability to find an ion inside the CNT pore is low and we can neglect these effects in this particular case. Investigation of molecular mechanisms of RTIL interactions with the *internal* surface of subnanometer CNT pores will be considered elsewhere.

4.4.1 Simulation details

We performed Molecular Dynamics (MD) simulations of CNT with (6,6) chirality dissolved in several mixtures of RTILs with AN: EMIm-TFSI, BMIm-TFSI and OMIm-TFSI RTILs (see Figure 41). The RTIL molar concentrations in all RTIL-AN mixtures were 2 mol/L. To understand the role of AN solvent on the studied interfacial effects we performed an additional simulation of the CNT dissolved in neat EMIm-TFSI. In our simulations we employed the fully

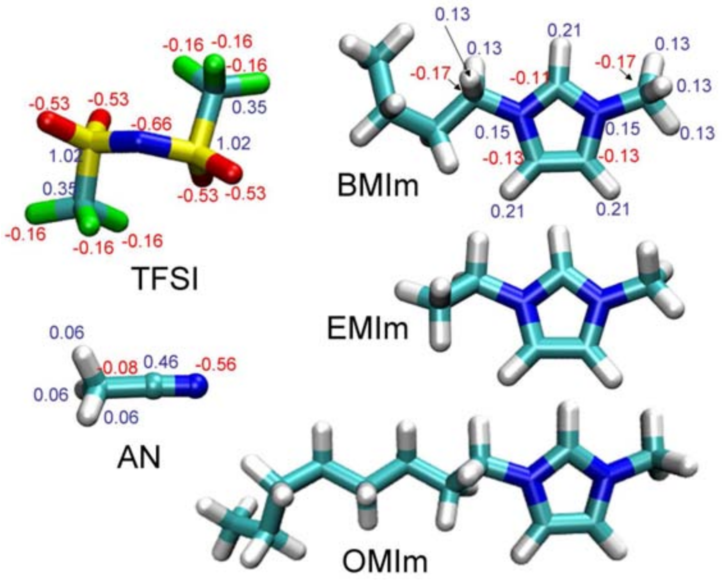

Figure 41: Sketch representation of the molecular species considered in the study. Cyan color – carbon atoms, white color – hydrogen atoms, blue color – nitrogen atoms, green color – fluorine atoms, yellow color – sulfur atoms, red color – oxygen atoms. Numbers at the atoms show the corresponding atomic partial charges in *e* units: the numbers highlighted by the blue color show positive partial charges and the numbers highlighted by the red color show negative partial charges.

atomistic OPLS-AA force field [168, 169], with partial charges and dihedral angles potential parameters developed by Lopes et al. [190, 191]. We used the Gromacs 4.5 software [167].

We used the TubeGen program to generate coordinates of the CNT atoms [126]. A segment of CNT with length of 3.94 *nm* was placed in a rectangular box and was oriented along the Z axis. Then, the RTIL molecular ions and AN molecules were randomly placed inside the simulation boxes with the help of Packmol program [176]. We provide the resulting number of molecular species in the simulation boxes in Table 5 (the numbers are shown for the zero CNT surface charge). The simulation boxes contained 200 ion pairs (and additional molecular ions for neutralization of the CNT surface charge, if applicable) for the systems of CNT dissolved in 2M RTIL solution in AN. The number of AN molecules were adjusted in such a way that the volume of the simulation box after the equilibration in NPT-ensemble differed not more than 3% from system to system. The resulting volumes of the systems were in the range: 6.21-6.23×6.21-6.23×3.94 nm^3. The three systems containing CNT in neat EMIm-TFSI ionic liquid after equilibration in NPT ensemble had volumes in the range 6.16-6.26×6.15-6.26×3.94 nm^3 and contained 340 ion pairs.

All the systems were investigated at different CNT surface charge densities: σ=-0.5, 0.0,

+0.5 e/nm^2. Similar to Ref. [65], in the simulations of the charged CNT surface the non-zero charge on the carbon nanotube was neutralized by addition of an extra number of cations (negatively charged surface) or anions (positively charged surface): in our case we used 5 extra ions for systems with σ=-/+0.5 e/nm^2.

The generated initial molecular configuration were optimized by the energy minimization algorithm implemented in Gromacs [167]. Then the systems were equilibrated in the NPT-ensemble at T=343.15K and P=1 *bar* until the density becomes constant (it took at least 0.3 *ns* and up to 1.2 *ns* of the simulation time). After the NPT simulations we fixed the geometry of the simulation boxes and heated the systems up to 1000-1500K and then annealed the final configurations during 2 *ns* simulation time with gradual decrease of temperature from 1000-1500K to 343.15K. Starting from the resulting configurations we then performed production 30 *ns* simulations for each system in the NVT ensemble at 343.15K to collect statistics. During the production runs we stored the atomic coordinates of the systems each 0.3 *ps* for further analysis.

Other simulation details were similar to those describes previously in Section 4.2.1.

To facilitate the analysis of the excluded volume effects on the formation of the interfacial structures we calculated the volumes of cavities of molecular ions and AN molecule dissolved in AN with the help of Gaussian03 software [192]. The geometries of the species were optimized at the B3LYP/6-31g(d,p) level of theory. In the quantum mechanics calculations we used the Self Consistent Isodensity Polarizable Continuum Model (SCI-PCM) [193] to model the acetonitrile solvent.

Table 5: Numbers of the molecular species in the simulation boxes of the studied systems. The numbers are shown for the simulations of the neutral CNT surface.

	N (RTIL ion pairs)	N (AN)
2M AN EMIm-TFSI	200	600
Neat EMIm-TFSI	340	-
2M AN BMIm-TFSI	200	480
2M AN OMIm-TFSI	200	250

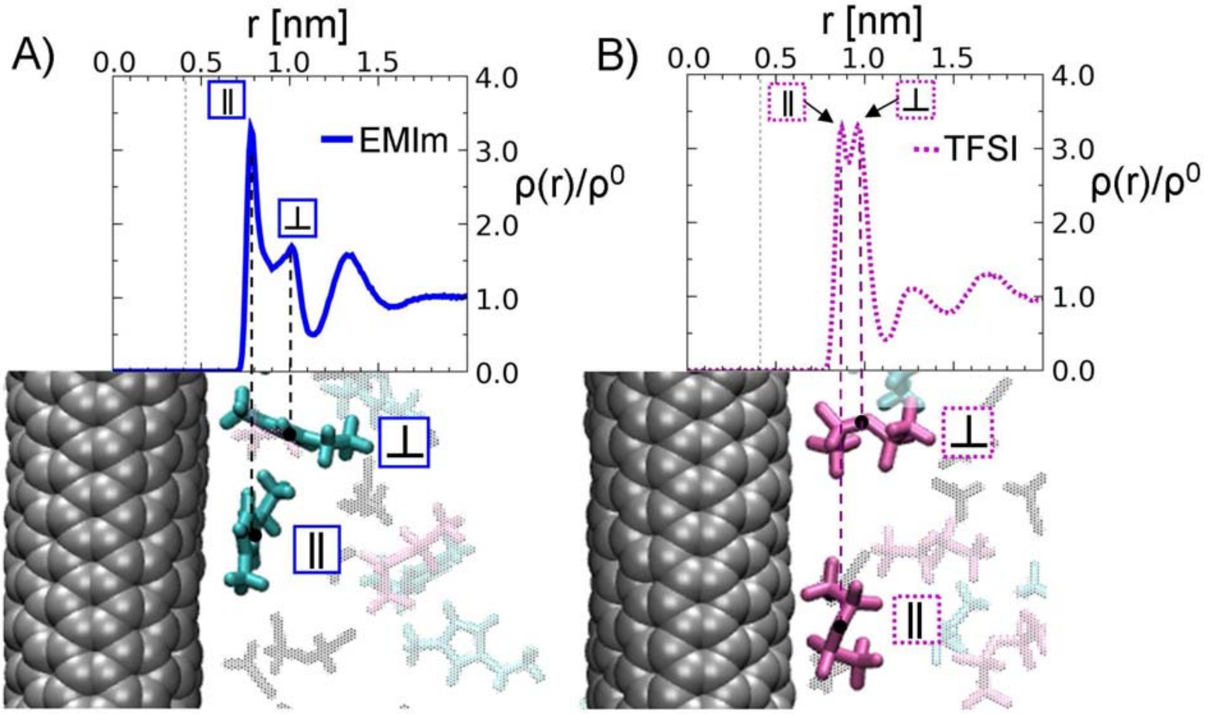

Figure 42: Radial density profiles of EMIm and TFSI molecular ions around CNT in 2M AN EMIm-TFSI solution at the neutral CNT surface. The asymmetry of ion geometry (shape, size etc., see Figure 41) results in a complicated molecular structure of the electrolyte at the CNT surface. Molecular snapshots represent orientations of the molecules consistent with the peaks on the corresponding RDPs. For simplicity, the whole molecules of EMIm ions are represented by the cyan color, TFSI ions - by the magenta color, AN molecules - by the black color.

4.4.2 Neutral carbon nanotube surface

Firstly, we analyzed density distributions of the molecular ions around non-charged carbon nanotube in 2M AN EMIm-TFSI solution. We present the radial density profiles (RDPs) of EMIm and TFSI molecular ions on Figure 42. All RDPs were calculated for the centers of mass of the molecules. The pronounced peaks on the RDPs show that both EMIm and TFSI ions form distinct solvation shells around the CNT (see Figure 42).

EMIm cations tend to lay parallel to the surface: there is a strong peak on the EMIm RDP around CNT at r=0.75 *nm* (marked as ||). We consider the vector connecting the α-carbons at the imidazolium ring as a “molecular vector” of the imidazolium-based cations and thus the angle between this “molecular vector” and the CNT surface determines orientation of molecular cations at the surface (see Figure 43). The second peak (at r=1.0 *nm*) corresponds to a perpendicular orientation of the EMIm cations to the surface ($\perp$). However, the density peak for cations with perpendicular orientation is less pronounced compared to the || orientation.

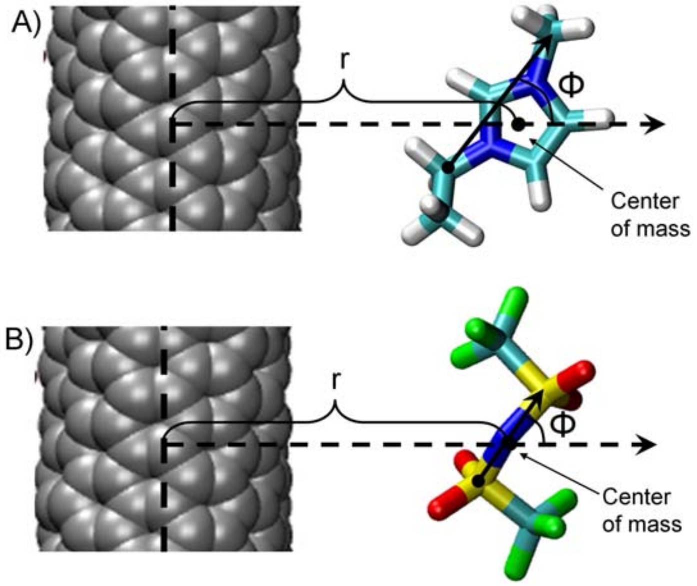

Figure 43: Orientation of molecular ions around CNT. Φ is the angle between “molecular vector” and a vector connecting the CNT axis and center of mass of the molecular ion (this vector is perpendicular to CNT axis). A) EMIm orientation around CNT. We define the molecular vector to be the vector connecting the alpha carbon atom at the imidazolium ring of the longer alkyl chain to the alpha carbon atom of the methyl group at the imidazolium ring. The same criteria are applied to other molecular cations: BMIm and OMIm. B) TFSI orientation around CNT. We define the molecular vector to be the vector connecting two sulphur atoms. Due to the symmetry of the TFSI ions the direction of the vector is chosen arbitrary.

Overall, there is an enrichment of EMIm cations in the region from r=0.75 to 1.0 *nm* from the CNT axis (the relative density here is about 1.5 the bulk density). This region corresponds to all intermediate orientations in between the two characteristic ones: || and ⊥. The hollow at about 1.1 *nm* indicates the boundary of the first EMIm solvation shell around the CNT. We note, that the EMIm cations form also at least one more solvation shell around the CNT as indicated by the distinct peak at r=1.3 *nm*.

The first TFSI solvation shell around CNT is narrower compared to the EMIm solvation shell (Figure 42B). TFSI ions may be thought as dumbbell particles where each bead consists of a CF_3-SO_2 group. We consider the line connecting the centers of sulphur atoms as the “molecular vector“ of the TFSI anions. TFSI ions (dumbbells) orient in 2 different ways around CNT: parallel (||) and perpendicular to CNT surface (⊥). This is indicated by the ’fine structure’ of the first large peak on the TFSI RDP that has two small peaks (see Figure 42B). However, we note that due to internal flexibility of TFSI anions, the ”parallel“ to the surface orientation of TFSI dumbbells includes a variety of slightly non-parallel to the surface orientations of the chosen ”molecular vector” of TFSI (sulphur-sulphur vector) (see, for instance, the molecular picture of the || orientation on Figure 42B: the CF_3-SO_2 groups are twisted one with respect another). In this study for simplicity we consider all these orientations as ”parallel“ to the surface orientations of TFSI ions.

The parallel (||) and perpendicular (⊥) orientations of TFSI are almost equally probable (the heights of the small peaks are similar, Figire 42B). The second solvation shell is not as pronounced as for the EMIm distribution (the height of the peak at r=1.3 *nm* is around 1.1). However, there is an evident third solvation shell of TFSI around CNT (peak at r=1.7 *nm*), presumably due to the attraction of TFSI molecular ions to the second solvation shell of EMIm around CNT (at r=1.3 *nm*, see Figure 42A).

4.4.3 Changes in the interfacial structures in response to the external field

In this section we describe the changes in the double layer in 2M AN EMIm-TFSI electrolyte upon charging the CNT surface. The RDPs for different surface charge densities on CNT (σ=-0.5, 0.0, +0.5 e/nm^2) are presented on Figure 44, first row.

σ=-0.5 e/nm^2**.** As expected, negatively charged CNT strongly attracts EMIm cations: there is a high peak on the corresponding RDP (see Figure 44). At the negatively charged surface the EMIm cations orient parallel to the surface (|| EMIm orientation). The perpendicular orientation to the surface (⊥ EMIm) becomes unfavorable. The second shell of EMIm ions around CNT (at r=1.35 *nm*) does not change much compared to the system with neutral CNT.

The distributions of TFSI anions at the negatively charged CNT surface change considerably compared to the neutral CNT. The CNT-TFSI RDP shows only one peak at r=1.0 *nm* compared to the two peaks at r=0.9 and 1.0 *nm* in the case of neutral CNT. This peak corresponds to a layer of TFSI anions with preferential parallel orientation to the first dense layer of EMIm cations (see Figure 47 and Table 9 for more justification).

We note, that acetonitrile is not substituted by the cations adsorbed to the negatively charge surface. There is even a little enhancement of AN concentration compared to the system with neutral CNT (see Figure 45). This can be explained by the strong interactions of AN (having strong dipole moment) with the charged surface. Overall, there is an enrichment of the density of the RTIL-AN solvent at the negatively charged surface.

The polarization of the electrolyte spreads up to 2-2.5 *nm* from the CNT axis (about 2-3 solvation shells of CNT). The range of polarization remains the same for all the three surface

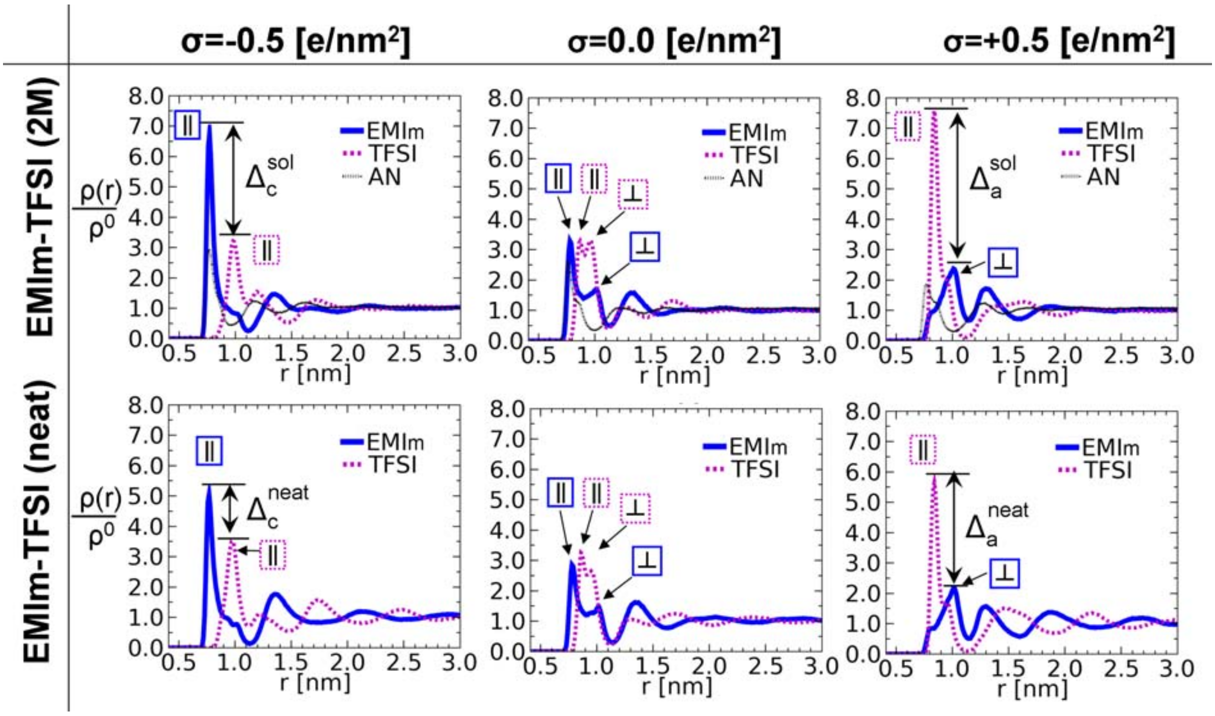

Figure 44: Fisrt row: radial density profiles of EMIm, TFSI and AN around CNT in 2M AN EMIm-TFSI solution for three surface charge densities on CNT: σ =-0.5, 0.0, +0.5 e/nm^2. There is an asymmetry of molecular ions response to the potential created by charged CNT. The potential causes structural changes in the interfacial region. Second row: radial density profiles of EMIm, TFSI around CNT in neat EMIm-TFSI solution for the three surface charge densities on CNT.

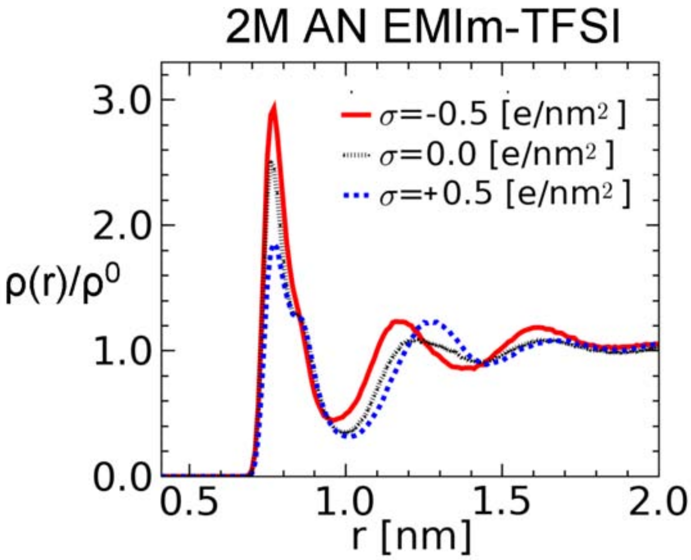

Figure 45: Radial density profiles of AN around CNT in 2M AN EMIm-TFSI electrolyte at different surface charge densities on the CNT.

charge densities.

σ=+0.5 e/nm^2. The positively charged CNT surface attracts TFSI anions, which prefer to lay parallel to the surface (|| TFSI orientation). In turn, the EMIm ions become preferentially oriented perpendicular to the surface (⊥ EMIm orientation). For cations, parallel orientation to the surface (|| EMIm orientation) becomes unfavorable (the height of the first peak on the RDP decreased more than 3.5 times).

We note, that the number of AN molecules at the anode surface drops down compared to the system with neutral CNT (see Figure 45). This is presumably due to the excluded volume effects because the anode interfacial region becomes occupied by the bulky TFSI anions. Indeed, the TFSI anions are about 1.4 times larger than EMIm cations and about 2.9 times larger than AN molecules (see Table 6). Thus, accommodation of large number of TFSI anions at the surface results in transfer of considerable amount of AN molecules from the CNT interface to the bulk solution.

Table 6: Volumes of solute cavities in acetonitrile

	V Å^3
AN	77.12
TFSI	224.39
EMIm	157.66
BMIm	203.03
OMIm	323.18

4.4.4 Effects of acetonitrile solvent on the electric double layer

In this section we compare the structures of the double layer in 2M AN EMIm-TFSI electrolyte and neat EMIm-TFSI ionic liquid to see whether the acetonitrile solvent makes an effect on the interfacial structures at the neutral and charged CNT surfaces. The RDPs of the molecular species for neat EMIm-TFSI at different surface charge densities on the CNT surface (σ=-0.5, 0.0, +0.5 [e/nm^2]) are presented in Figure 44, second row.

In neat EMIm-TFSI ionic liquid the polarization of the electrolyte spreads deap into the bulk of the neat IL for more than 2.5 nm. There are at least two to three solvation layers at the electrodes.

σ=0.0 [e/nm^2]. The structures of the interfacial regions at the neutral CNT for the neat IL and its mixture with AN are almost identical: addition of AN has minor effect on the RDPs of molecular ions (see Figure 44, second column). This indicates that the interface structure is determined mainly by the CNT-ion interactions and ion-ion interactions.

σ=-0.5 [e/nm^2]. At the negatively charged CNT the number of parallel oriented EMIm ions (|| EMIm orientation) and TFSI ions (|| TFSI orientation) increased, whereas only few ions oriented perpendicular to the surface are left (see the Supporting Information for more details). The peak which corresponds to the || TFSI orientation in the first layer is pushed away from the surface by 0.1 nm. Also, in contrast to the solution in AN, the amplitude of the second and subsequent layers is increased, indicating that the surface charge enhances the layering structure of the interfacial ionic liquid. Addition of AN decreases the number of TFSI ions near the dense layer of EMIm cations attached to the surface (see the change in the peak height differences (Δ_c^{sol} and Δ_c^{neat}) on Figure 44, first column). However, we note, that there are no changes in the peak positions in the neat RTIL and 2M RTIL-AN RDPs.

σ=+0.5 [e/nm^2]. The positively charged CNT surface has similar effect on the neat EMIm-TFSI as on its mixture with AN. Parallel orientation for EMIm ions (|| EMIm orientation) becomes unfavorable. But unlike in the AN solution, again the second and subsequent solvation layer peaks (r > 1.2 nm) increase in their amplitude, indicating the strengthening of the layering pattern. AN has similar effect on the double layer as at the negatively charged CNT. AN increases the difference between the relative number of the TFSI anions at the surface and the number of the EMIm cations attracted to the first layer of the TFSI anions (see the change in the peak height differences (Δ_a^{sol} and Δ_a^{neat}) on Figure 44, first column). Similar to the negatively charged surface, AN does not change the structural organization of the double layer (the peak positions remain the same in the neat RTIL as well as in the RTIL-AN mixture).

That observation suggests that AN affects the interionic correlations making them less strong (presumably due to the high polarity of AN), but does not lead to the structural reorganization of the double layer.

4.4.5 Molecular ion orientations at the carbon nanotube surface

Because of the complicated shape of molecular ions their distributions around CNT can not be resolved only by means of RDPs of the center of mass of molecular ions in contrast to the spherically symmetric alkali halide ions. Orientation of molecules also has to be taken into account. We resolved molecular orientations as the function of distance from the CNT by means of 2D orientational distribution plots (see below). Orientation distributions were calculated with the *g_sorient* program of Gromacs 4.5 suite, which was modified to be able to handle cylindrical symmetry of CNTs and to be able to resolve the orientation probability density as a function of distance.

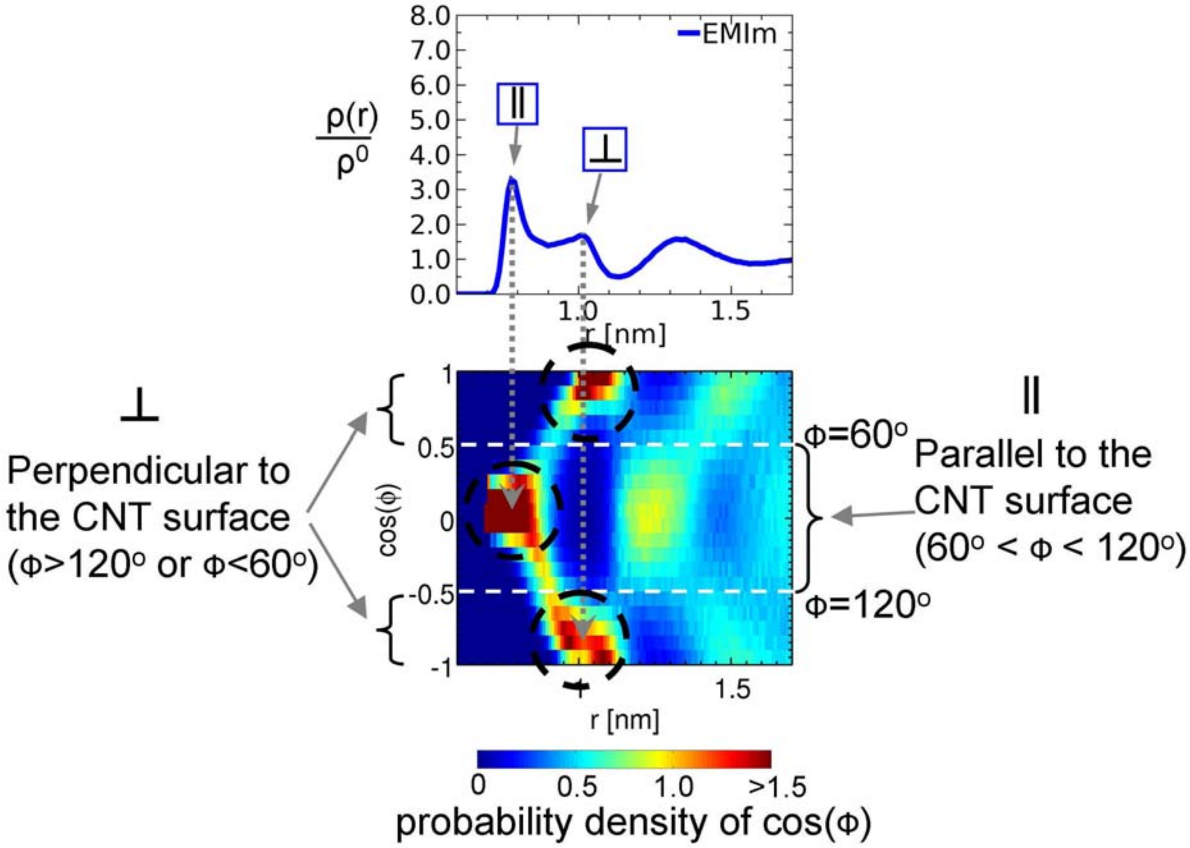

Figure 46: Radial Density Profile of EMIm (top) and orientation (cos(Φ)) probability density of EMIm as the function of distance (bottom) for 2M EMIm-TFSI in AN at σ=0.0 e/nm^2. Gray arrows indicate the correspondence of peaks on the RDPs to the peaks on the orientation probability density map. Random distribution of molecular orientations would have the probability density of 0.5 for all values of cos(Φ) from -1 to 1 (the integral of the probability density at certain r is unity). The 2D map (bottom) shows for each r the probability density to find a molecular ion at certain orientation around CNT (more specifically, at certain value of cos(Φ), see Figure 43). See text for more explanations.

Molecular ion orientation at the carbon nanotube surface. Definitions To quantify the molecular orientations we define a vector which is rigidly bound to a particular molecule (see Figure 43). An example orientation distribution is shown on the Figure 46. The 2D map (Figure 46 bottom) shows for each r the probability density to find a molecular ion at certain orientation around CNT (more specifically, at certain value of cos(Φ), see Figure 43). Mapping the peaks on the RDP and the peaks on the 2D map of the ion orientation we can understand ions in which orientation make a major contribution to the corresponding peak on the RDP. As one can see, there are two peaks on the EMIm RDP (top graph) for $r < 1.13$ *nm*. The first peak (at $r = 0.8$ *nm*, cos(Φ) of about 0) on the 2D orientation map (marked by dashed black circle) shows that the first peak on RDP is formed by EMIm ions which are parallel to the CNT surface (lay on the surface). The peaks at $r = 1.0$ *nm*, cos(Φ) of about 1 and -1 (marked by dashed black circles) indicate that the second peak on RDP is formed by EMIm ions which are perpendicular to the CNT surface. Here and after we use the following criteria: if $-0.5<\cos(\Phi)<0.5$ ($60^o < \Phi < 120^o$) then we assume that molecular ion is parallel to the CNT surface, otherwise the ion is perpendicular to the CNT surface (the criteria are marked by white dashed lines on the 2D orientation map). In the case of random orientation distribution such criteria would give equal probabilities to find a molecule in parallel and perpendicular orientations to the CNT surface. Zero probability densities for all values of cos(Φ) at small r indicate that no molecules were observed at these distances during the whole simulation time.

Two dimensional orientation maps of molecular ions at the carbon nanotube surface

Table 7: Cation Radial Density Profiles (first rows) and orientation probability densities as the functions of distance (second rows) for all studied systems: A) 2M EMIm-TFSI in AN solution, B) 2M BMIm-TFSI in AN solution, C) 2M OMIm-TFSI in AN solution, D) neat EMIm-TFSI ionic liquid. Gray arrows indicate the correspondence of peaks on the RDPs to the peaks on the orientation distributions. The signs || or ⊥ indicate that the peaks on a RDP (at which they are placed) are formed by molecular ions oriented parallel or perpendicular to the CNT surface, respectively.

System	Distributions of molecular cations
A) EMIm-TFSI (2M)	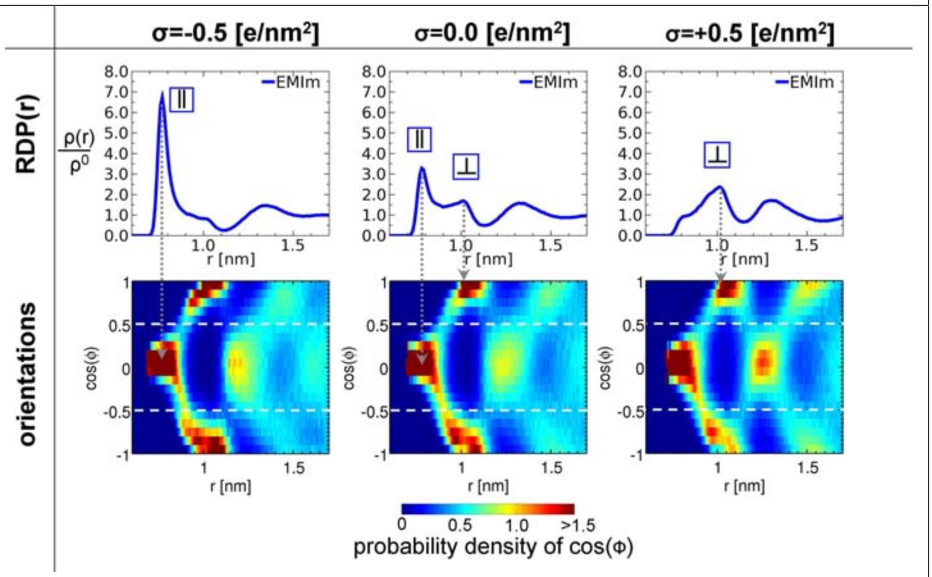

Continued on next page

B) BMIm-TFSI (2M)	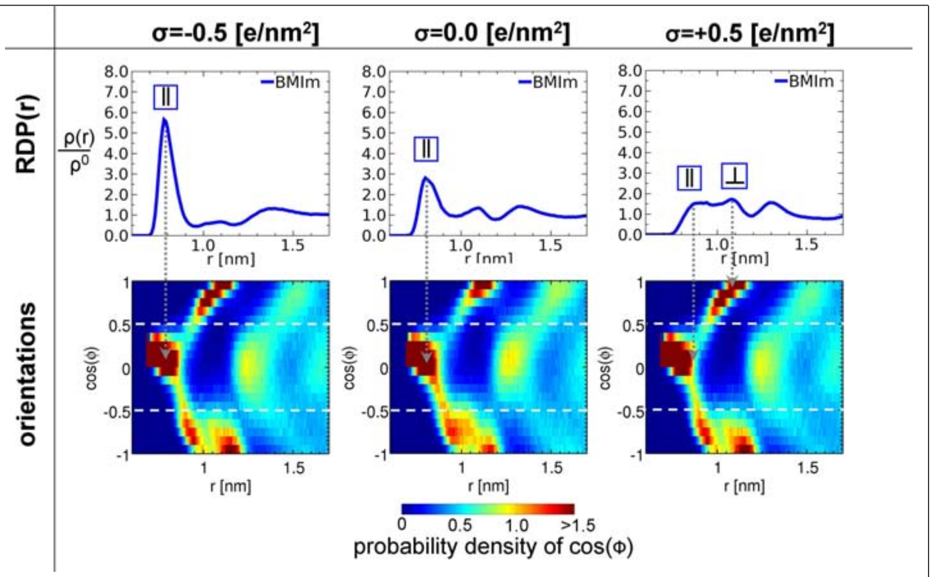
C) OMIm-TFSI (2M)	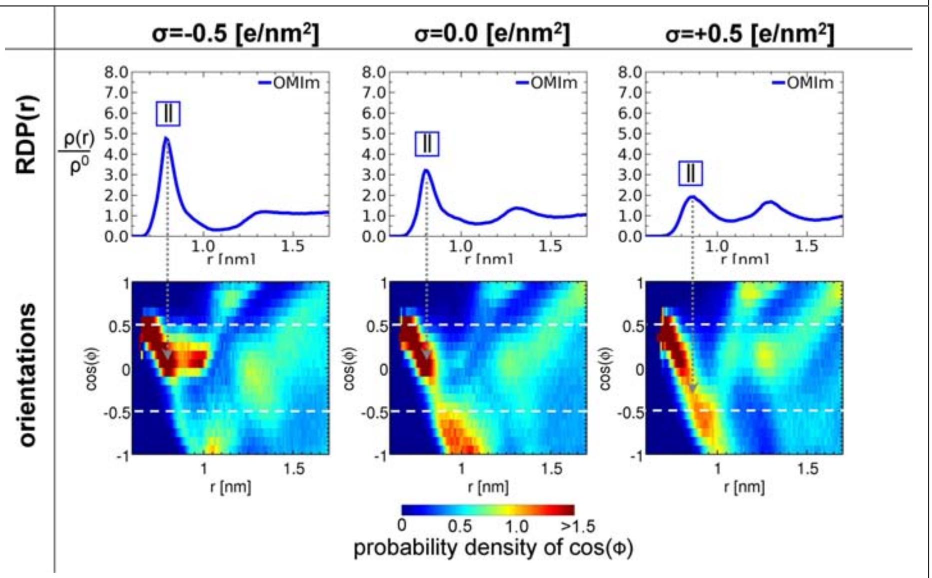
D) EMIm-TFSI (neat)	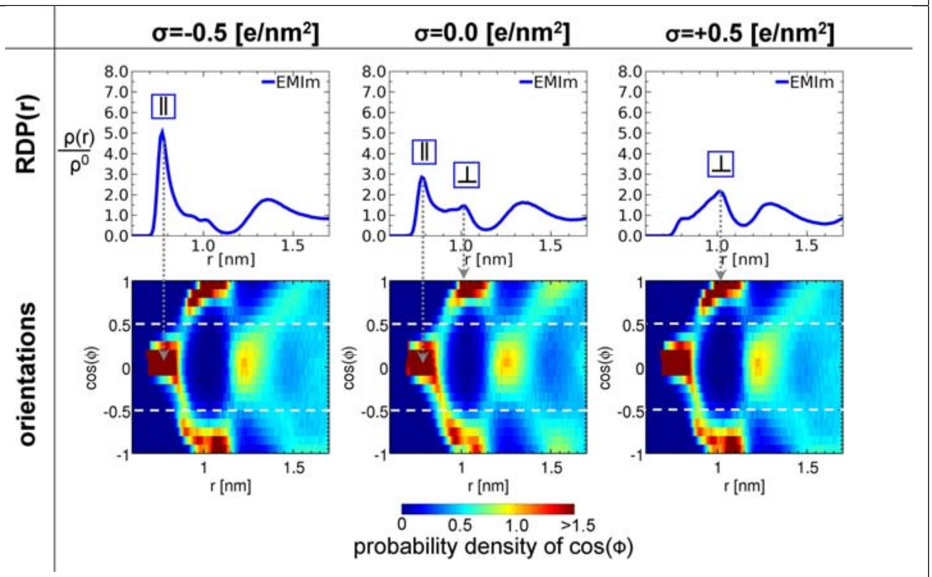

Table 8: TFSI Anion Radial Density Profiles (first rows) and orientation probability densities as the functions of distance (second rows) for all studied systems: A) 2M EMIm-TFSI in AN solution, B) 2M BMIm-TFSI in AN solution, C) 2M OMIm-TFSI in AN solution, D) neat EMIm-TFSI ionic liquid. Gray arrows indicate the correspondence of peaks on the RDPs to the peaks on the orientation distributions. The signs || or ⊥ indicate that the peaks on a RDP (at which they are placed) are formed by molecular ions oriented parallel or perpendicular to the CNT surface, respectively.

System	Distributions of molecular anions
A) EMIm-TFSI (2M)	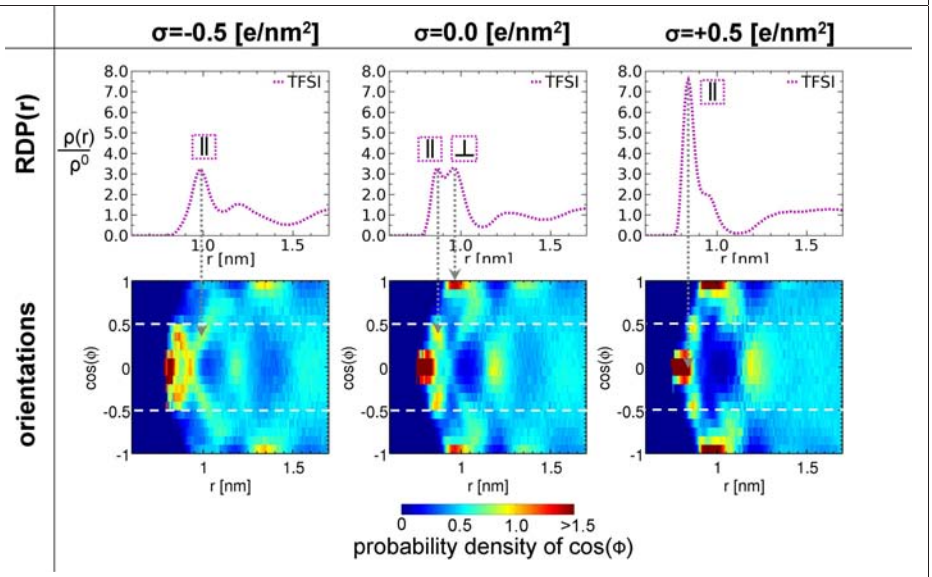
B) BMIm-TFSI (2M)	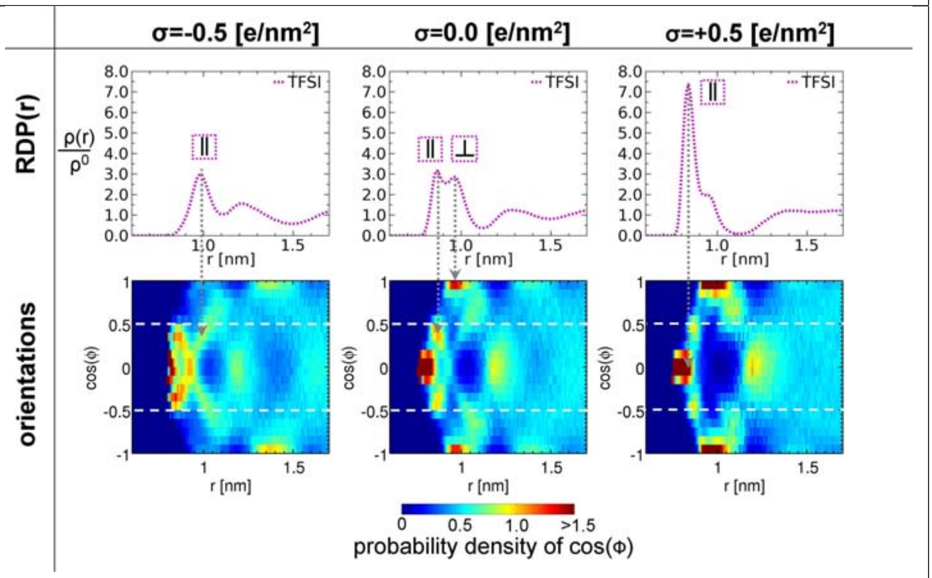

Continued on next page

C) OMIm-TFSI (2M)	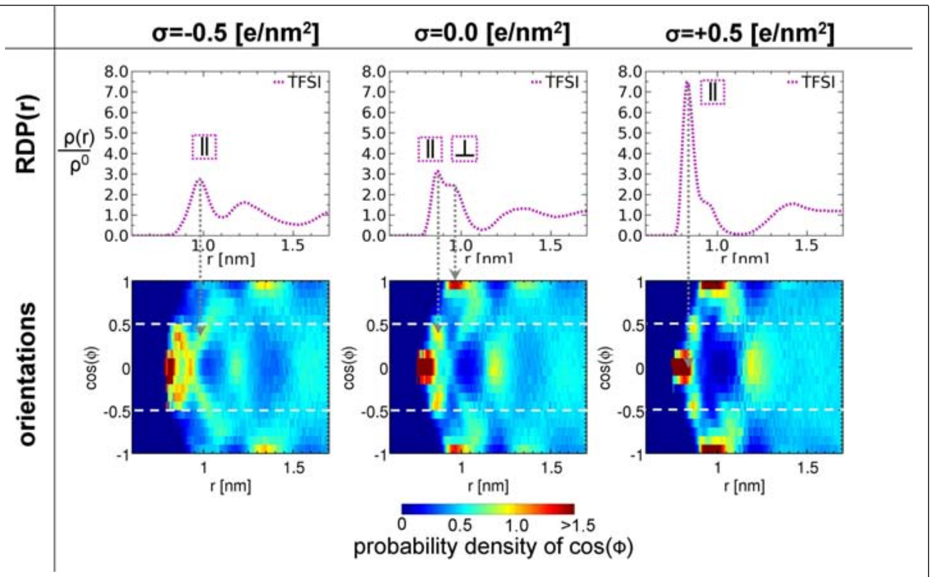
D) EMIm-TFSI (neat)	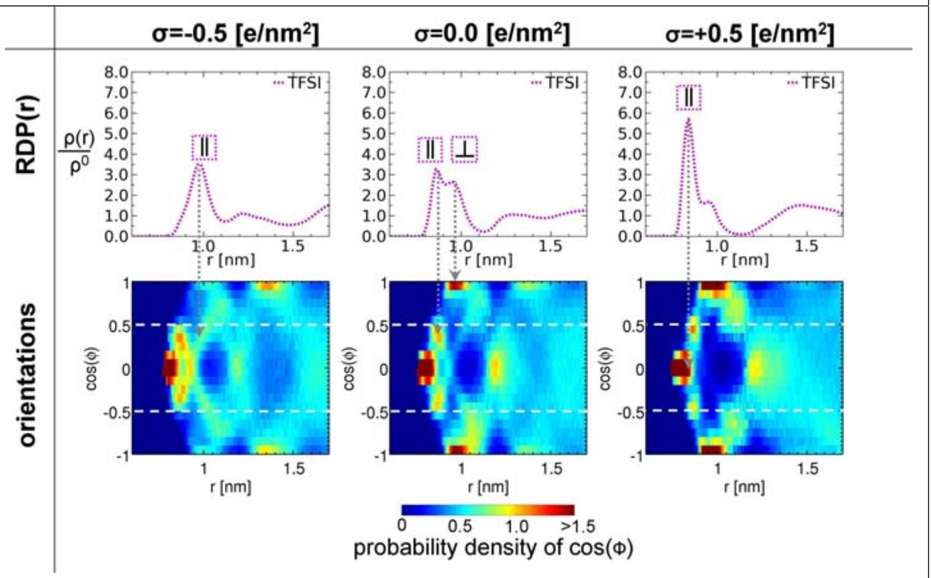

Number of molecular ions oriented parallel and perpendicular to the carbon nanotube surface We estimated the numbers of molecular ions oriented parallel and perpendicular to the CNT surface in the CNT solvation shell per 1 nm of the CNT length. We defined the boundary for the CNT solvation shell to be the position of the first deep minimum on the EMIm center of mass RDP in 2M EMIm-TFSI in AN solution at $\sigma=0.0\ e/nm^2$. The boundary is $r = 1.13\ nm$. We calculated the average number of particles at a certain distance r around CNT in the following way:

$$n_{\Delta r=0.01nm}(r) = \rho^0 \cdot \frac{\rho(r)}{\rho^0} \cdot 2\pi r \cdot \Delta r \tag{43}$$

where $\rho^0$is the bulk density of the corresponding particles, $\frac{\rho(r)}{\rho^0}$is the RDP of the corresponding particles, $n_{\Delta r=0.01nm}(r)$ is the average number of particles at a certain distance r in the cylindrical

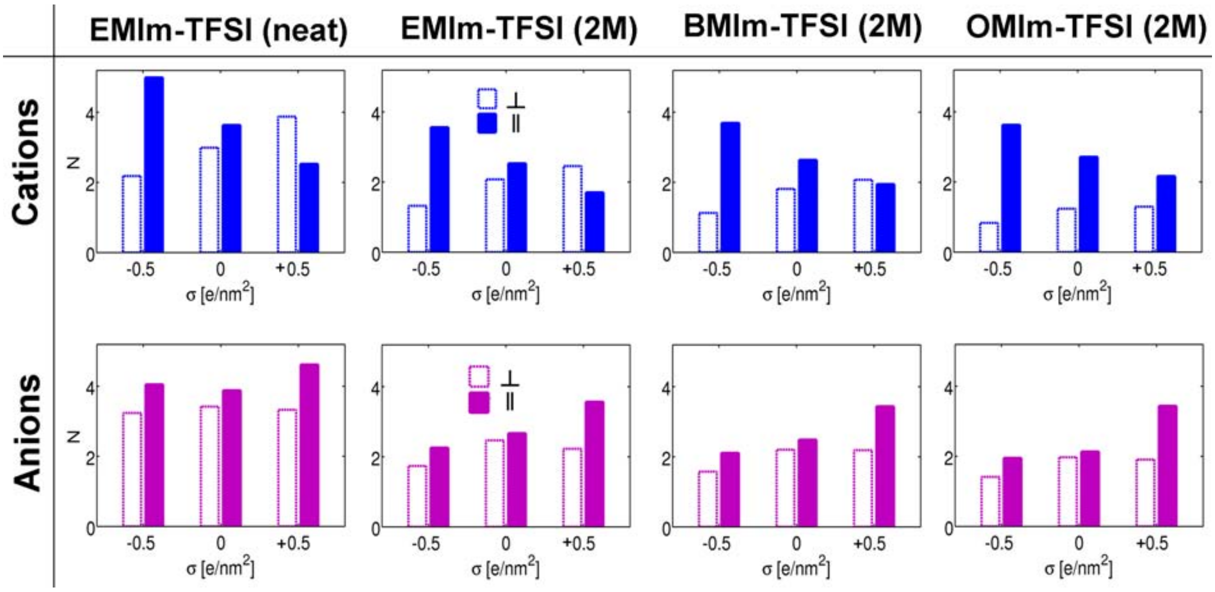

Figure 47: Number of molecular cations (first row) and anions (second row) oriented parallel (||, filled bars) and oriented perpendicular (⊥, empty bars) to the CNT surface in the first solvation shell of CNT (0<r<1.13 *nm*) for different surface charge densities in all the studied systems (columns 1-4). The numbers are given per 1 nm of the CNT length.

volume segment with the difference between radii of smaller and larger cylinders of Δr (in our case Δr =0.01 *nm*). Here we imply the length of the CNT segment to be 1 *nm*.

From 2D orientation maps for each distance r we estimated the probability to find a particle in a parallel to the surface orientation (by integrating the cos(Φ) probability density at this r over the interval -0.5<cos(Φ)<0.5) and to find a particle in a perpendicular to the surface orientation (by integrating the cos(Φ) probability density at this r over the intervals 0.5<cos(Φ)<1.0 and -1.0<cos(Φ)<-0.5). The discretization of the functions on the r coordinate was the same as for the RDPs: Δr =0.01 *nm*.

Then we multiplied the number of particles at certain distance r by the probabilities to find a molecule at the same r in a parallel to the surface orientation and in a perpendicular to the surface orientation. We integrated the obtained functions over the interval $0<r<1.13$ *nm* to estimate the number of particles oriented parallel and perpendicular to the CNT surface in the CNT solvation shell per 1 *nm* of the CNT length. We illustrate the resulting values on the Figure 47.

Table 9: Ratio of the number of molecular cation (anions) oriented parallel and the number of molecular cations (anions) oriented perpendicular to the CNT surface in the solvation shell of CNT for different surface charge densities in all the studied systems. To analyze the table we define a threshold: if the number of ions in one orientation is larger more than 25% than the number of ions in another orientation then we assume that the former orientation is preferable, otherwise both of them are equally probable. Thus, if the ratio is more than 1.250 then the particles are preferably oriented *parallel* to the CNT surface, if the ratio is less than 1/1.250=0.800 then the particles are preferably oriented *perpendicular* to the CNT surface, if the ratio is more than 0.800 and less than 1.250 then both orientations are equally probable. We present the results on the Figure 5 of the main text. The table reveals the following conclusions. 1) An increase of the non-polar tail length increases propensity of imidazolium-based cations to lay parallel to the surface. 2) At the cathode TFSI anions and cations are oriented mainly parallel to the surface. 3) At the anode the TFSI anions are oriented preferentially parallel to the surface, however the preferential orientations of cations depend on the length of non-polar tails. EMIm cations are preferentially oriented perpendicular to the surface, BMIm are in both parallel and perpendicular orientations, OMIm are preferentially oriented parallel to the surface. 4) An addition of acetonitrile into EMIm-TFSI ionic liquid does not *qualitatively* change the preferential orientations of molecular ions.

Molecular ion	**System**	σ=-0.5 e/nm^2	σ=0.0 e/nm^2	σ=0.5 e/nm^2
Cations	EMIm-TFSI (neat)	2.287	1.214	0.652
	EMIm-TFSI (2M)	2.703	1.219	0.694
	BMIm-TFSI (2M)	3.289	1.457	0.940
	OMIm-TFSI (2M)	4.352	2.202	1.676
TFSI anions	EMIm-TFSI (neat)	1.252	1.135	1.388
	EMIm-TFSI (2M)	1.303	1.081	1.604
	BMIm-TFSI (2M)	1.336	1.130	1.570
	OMIm-TFSI (2M)	1.383	1.085	1.807

4.4.6 Effects of the length of the cation alkyl chain on the structure of the electrical double layer

To understand the role of the cation molecular geometry on the interfacial structure and on the molecular orientation at the CNT surface we analyzed simulation results for AN mixtures with

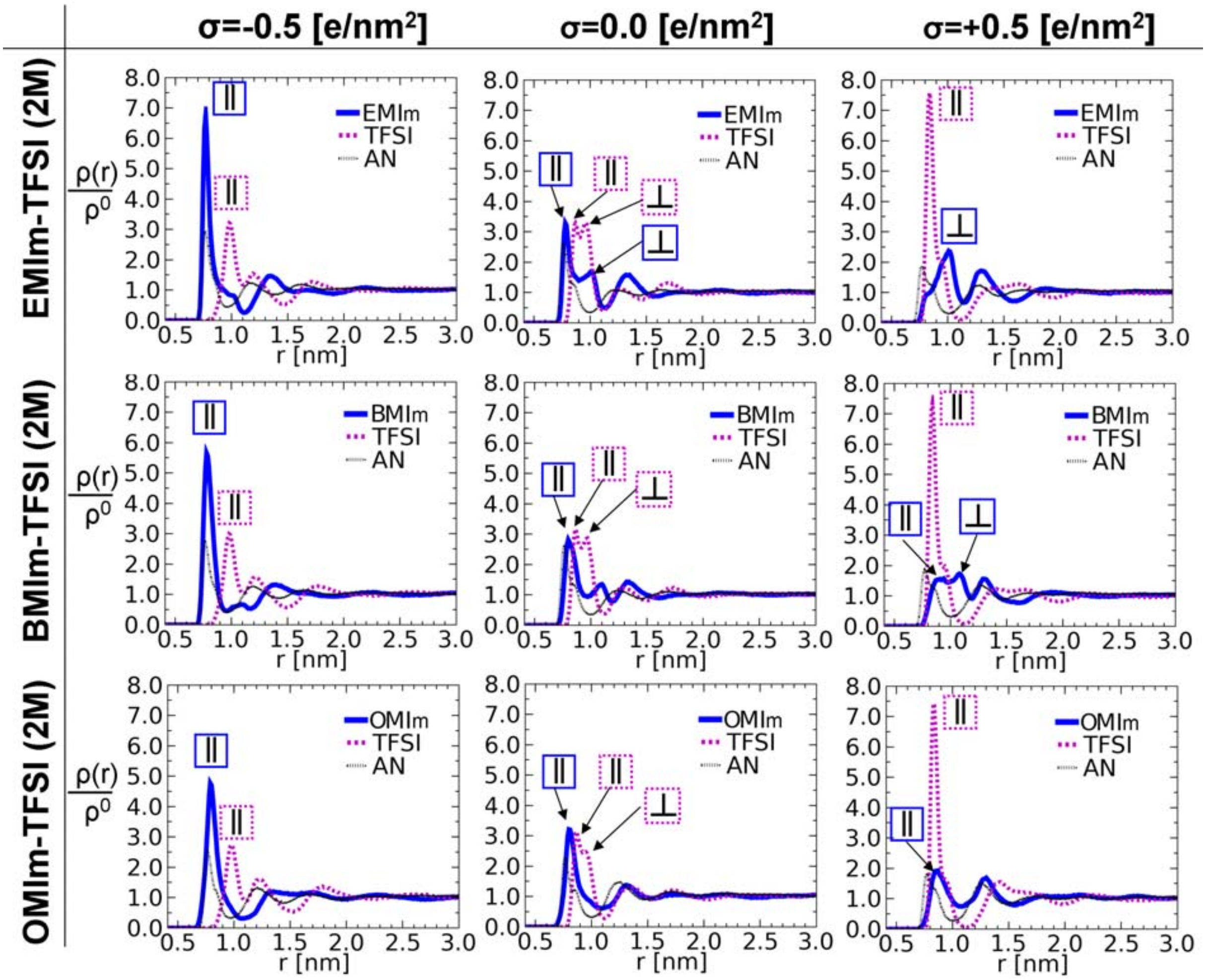

Figure 48: First row: radial density profiles of EMIm, TFSI and AN around CNT in 2M AN EMIm-TFSI solution for three surface charge densities on CNT: σ =-0.5, 0.0, +0.5 e/nm^2. Second row: radial density profiles of BMIm, TFSI and AN around CNT in 2M AN BMIm-TFSI solution for three surface charge densities on CNT: σ =-0.5, 0.0, +0.5 e/nm^2. Third row: radial density profiles of OMIm, TFSI and AN around CNT in 2M AN OMIm-TFSI solution for three surface charge densities on CNT: σ =-0.5, 0.0, +0.5 e/nm^2. The length of the cation alkyl chain does not make significant effects on the orientation of the RTIL molecules at the cathode. However, it affects the structure of the interfacial layer at the neutral interface: the tendency for cations to lay parallel to the CNT surface increases with increase of the length of the 'tail'. In addition, the length of the 'tail' affects the orientation of the cations in the double layer at the anode. For the EMIm system with the shortest 'tail', the EMIm cations form a second layer after the first dense layer of TFSI anions and they are preferentially oriented perpendicular to the surface. However, with an increase of the 'tail' the concentration of the cations in the first layer increases and they tend to be oriented parallel to the surface.

RTILs varying the length of the cation alkyl chains. Figure 48 shows the RDPs of molecular species at the charged and neutral CNT surfaces for EMIm-TFSI, BMIm-TFSI and OMIm-TFSI mixtures with AN. We also analyzed the preferential orientation of the molecules in the interfacial layers that reveal themselves in the RDP peaks. The preferential orientations assigned to the peaks are shown by the || and ⊥ symbols on Figure 48.

σ=-0.5 e/nm^2**.** The length of the cation alkyl chain does not make significant effects on the orientation of the RTIL molecules at the CNT cathode. The RDPs and orientations of RTIL ions do not change *qualitatively* for different cations. However, the height of the first peak on the CNT-cation RDP decreases with lengthening of the alkyl chain. We attribute this to the corresponding increase of the excluded volume of the cations (see Table 6) (the larger the volume the more difficult is to ’pack’ the ions to the dense first layer).

σ=0.0 e/nm^2**.** The length of the cation alkyl chain considerably affects the structure of the interfacial layer at the neutral interface: the tendency for cations to lay parallel to the CNT surface increases with an increase of the length of the ’tail’. These observations are in line with the recent experimental findings indicating propensity of non-polar tails to absorb on the neutral RTIL liquid-vacuum interface [52].

σ=+0.5 e/nm^2**.** In addition, the length of the ’tail’ affects the orientation of the cation molecules in the double layer at the positively charged CNT. For the EMIm system with the shortest ’tail’, the EMIm cations form a layer after the first dense layer of TFSI anions and they are preferentially oriented perpendicular to the CNT surface. However, increasing the length of the alkyl chain the concentration of the RTIL cations in the first layer increases (the positions of first TFSI and cation peaks become almost the same) and they tend to be oriented more parallel to the surface.

4.4.7 Correlations with the experimental data

Atkin et al. [54] published an atomic force microscopy (AFM) study of the gold interface solvated in EMIm-TFSI (note, that they name this as 1-ethyl-3-methylimidazolium bis [trifluoromethylsulfonyl] amide, [EMIm]TFSA). They reported several steps in the force curve [54], which coincide well with the observed layered structure in MD simulations of neat EMIm-TFSI at carbon nanotube surface in this study (see Figure 44). There is no pronounced third solvation layer of CNT in our study, as it is indicated by the AFM at the gold surface. We attribute the "weaker" layering pattern in our simulations to the differences in temperatures: temperature in the simulations was about 70°C, while "all force curves were acquired continuously at room temperature (22 °C)" for the AFM measurements [54].

There are some experimental studies on the orientation of IL molecules on the liquid - vacuum interface, see for example [52, 67, 68]. For the liquid - solid interface these data are difficult to obtain. Nakajima et al. [67] investigated the liquid - vacuum interface of different 1-alkyl-3-methylimidazolium – TFSI ionic liquids using the high-resolution Rutherford backscattering spectroscopy. They showed that, due to the solvophobic nature, long alkyl chains of cations point away from the bulk liquid to vacuum and therefore stimulate the imidazolium ring to stay perpendicular to the surface. In our simulations on the RTIL-carbon interface we observe an opposite effect: increase of alkyl chains increases the tendency for the imidazolium ring to lay parallel on the surface. We attribute the differences between RTIL-vacuum and RTIL-carbon nanotube interfaces to the strong Van der Waals attraction between the non-polar alkyl chains and carbon nanotube surface. Contrary to the RTIL-vacuum interface, at the RTIL-CNT interlace the alkyl chains of imidazolium-based cations tend to lay parallel on the CNT surface and force the imidazolium rings also to lay flat on the carbon nanotube surface.

Hayes et al. [70] investigated the structure of different ionic liquids (1-ethyl-3-methyl imidazolium tri (pentafluoroethyl) trifluorophosphate and 1-butyl-1 -methylpyrrolidinium (Py) tris (pentafluoroethyl trifluorophosphate) at the charged Au(111) electrode. They showed that IL layering is more pronounced at charged Au(111) surface compared to the neutral surface. They showed that increase of the potential leads to flattening of the tightly bound cation layer, indicating possible reorientation of cations (EMIm and Py) to lay flat on the surface [70]. We observe similar, effects: increase of the potential at the CNT cathode increase significantly the tendency of EMIm cation to lay flat on the surface (see Figure 44).

In this work, we show that applying potential on the CNT electrode or varying the structure of molecular ions one can adjust molecular ion orientations and thus the structure of the CNT-IL interface shell, which supports the experimental observations of Hayes et al. [70].

4.4.8 Conclusions

The analysis of the simulation data results in the following conclusions:

1. There is an enrichment of all molecular components of ionic liquids under study at the CNT surface with formation of several distinct layers even at the non-charged CNT surface.

2. Mixing RTIL with acetonitrile decreases ion-counterion correlations in the electric double layer.

3. Increase of the length of the non-polar cation ’tail’ increases propensity of imidazolium-based cations to lay parallel to the CNT surface.
4. At the CNT cathode TFSI anions and molecular cations are preferentially oriented parallel to the surface.
5. At the CNT anode the TFSI anions are oriented parallel to the surface, however the preferential orientations of cations depend on the length of non-polar tail: EMIm cations are oriented perpendicular to the surface, BMIm are in both parallel and perpendicular orientations, OMIm are oriented parallel to the surface.
6. Applying potential on the CNT electrode or varying the structure of molecular ions one can adjust molecular ion orientations, and thus the structure of the CNT-IL interface shell.

5 Summary

In this thesis we investigated ion interactions with the surfaces of carbon nanomaterials dispersed in different aqueous and non-aqueous solvents: aqueous dispersions, N-methyl-2-pyrrolidone dispersions, organic salt/acetonitrile dispersions and room temperature ionic liquids/acetonitrile dispersions. We used molecular dynamics simulations to understand the molecular-scale mechanisms of ion interactions with the CNM surfaces. We considered carbon nanotube and carbon "nanoonion" structures as representatives of the CNMs. Despite the high diversity of the system compositions studied in the thesis, the main features of ion interactions with CNM surfaces can be rationalized by similar mechanisms. The summary points of the thesis are:

1. Interaction of ions with the CNM surface in dispersions are determined by the interplay of the different particle-particle interactions: ion-solvent, CNM surface-solvent as well as solvent-solvent and ion-CNM surface interactions. The strength of the ion-solvent and CNM-solvent interactions determines the penalty (energy losses) for the partial desolvation of the ion and CNM surface upon the ion-CNM direct contact formation. The solvent-solvent interactions determine the energy gain originating from the solvation of the released solvent molecules upon the partial desolvation of the particles. In turn, the ion-CNM interactions determine the energy gain upon the ion-CNM surface direct contact formation. This last term is negligible comparing to other terms for small alkali halide ions, but becomes more significant for bigger molecular ions. The described scheme brings a physical picture "how to think about" the phenomena of the solvent mediated interactions in solutions. Based on the scheme, in this thesis, we rationalized the process of ion interactions with the CNM surfaces in different systems. We believe that it can be applied for rationalizing many other systems where the solvent mediated particle-particle interactions take place.

2. The ion-solvent interactions play an important role in the process of the ion-surface direct contact formation, since to make direct contacts with the carbon nanomaterial surface, ions have to become partially desolvated. Depending on the strength of ion-solvent interactions, however, the partial desolvation of ions might be energetically favorable or unfavorable:

   a) If the ions are strongly solvated (i.e. the energy of a solvent molecule release from ion's solvation shell is high) then the partial desolvation of ions is energetically unfavorable. In this case the energy gain originating from the solvation of the released solvent molecules does not compensate the energy losses upon the partial desolvation of the ions. As a result, a salt depletion area is formed around the CNM surface, where the concentration of ions is less than in the bulk solution. This leads to "salting out" of CNMs from the dispersions by addition of the salts.

b) In turn, if the ions are weakly solvated (i.e. the energy of a solvent molecule release from ion's solvation shell is low) then the partial desolvation of ions is favorable. In this case the energy gain of the solvation of the released solvent molecules compensates the energy losses upon the partial desolvation of the ions. As a result, there is a preferential adsorption of the ions on the CNM surface. This should lead to "salting in" of CNMs in the dispersions by addition of salts.

3. In this thesis we show that the penalty for partial desolvation of the CNM surface also plays an important role in the process of the ion-CNM surface direct contacts formation. The penalty for the partial desolvation of CNM surface adds an additional energetic “barrier” for ions to come close to the CNM surface. In the case of weakly solvated CNM surfaces (like in aqueous CNT dispersions) relatively big ions (like iodides) do form significant amount of direct contacts with the CNM surfaces. In turn, if there is a dense solvation shell at CNM surface (like in the case of CNT dispersions in NMP) the same ions do not enter the solvation shell of CNM and, thus, do not form direct contacts with the CNM surface.

4. In this thesis we showed that in the dispersions of carbon nanotubes in N-methyl-2-pyrrolidone there is a preferential depletion of inorganic ions (Na^+ and I^-) from the CNT-NMP interface due to the high energetic penalties for the partial desolvation of the ions and the CNT surface. The ion depletion from the CNT surface results in the increase of solvophobic interactions between the carbon nanotubes. As a consequence, the CNT-NMP dispersions become thermodynamically less stable at higher concentrations of salts. The increase of the CNT solvophobicity upon the salt addition was confirmed by direct experiments in complementary studies in collaboration with our colleagues from the Aston university.

5. Asymmetry of cation and anion solvation has to be taken into account while rationalizing the interaction of ions with different surfaces. We showed that alkali cations release more water molecules from their hydration shells attaching to the CNT surface in aqueous solutions than anions of a similar size. This is attributed to the fact that, firstly, the hydration

shell of cations is much denser than the hydration shell of anions, and, secondly, to the fact that anions interact much stronger with water molecules compared to cations, and thus due to the hight penalty for partial dehydration, can not lose water molecules from the hydration shells.

6. In this thesis we investigated the effect of the increase of the alkyl chain length of organic salt cations (tetraalkylammonium ions) on the structure of the electrical double layer at neutral and electrified carbon "nanoonion" surfaces in organic salt-acetonitrile solutions. We showed that, in the case of the neutral carbon "nanoonion" surface, the increase of the non-polar alkyl chains of the tetraalkylammonium ions leads to an increase of the molecular cation adsorption on the carbon "nanoonion" surface. In turn, at high negative surface charge densities on the carbon "nanoonion" surface the concentration of the tetra*ethyl*ammonium ions is higher than the concentration of tetra*butyl*ammonium ions, which is attributed to the stronger sterical constraints for molecular packing of the tetra*butyl*ammonium ions. The results indicate that the preferential adsorption of molecular ions at the CNM surface can be governed by varying the structure of molecular ions and/or applying an external electrostatic field.

7. Complex shapes of the molecular ions in room temperature ionic liquids result in different possible orientation of the molecules at the CNM surface in RTIL-acetonitrile mixtures. Such, an increase of the length of the the non-polar "tail" of the imidazolium-based cations increases propensity of the cations to lay parallel on the CNT surface. At the negatively charged CNT surface the TFSI anions and 3-methylimidazolium (MIm)-based molecular cations are preferentially oriented parallel to the surface. At the positively charged CNM surface the TFSI anions are also oriented parallel to the surface, however the preferential orientations of cations depend on the length of the non-polar alkyl "tails": ethyl-MIm cations are oriented perpendicular to the surface, butyl-MIm are in both parallel and perpendicular orientations, octyl-MIm are oriented parallel to the surface. Thus, the preferential orientations of molecular ions at the CNM surface can be governed by varying the structure of molecular ions and/or applying an external electrostatic field.

Outlook.

We believe that the findings of the thesis would be interesting for the many scientists working in the field of solubilization of carbon nanomaterials. We hope that the results can be useful for rational development of new methods for processing liquid dispersions of carbon nanomaterials.

Our results can help in understanding the observed correlation between the radii of ions and the strength of ion effects on the CNT photoluminescence quenching in aqueous solutions observed in experimental works [82, 83]. Indeed, weakly hydrated ions (like iodide or cesium) have large probability to lose water molecules from their hydration shell and to approach the CNT surface to form direct contact. The formation of the direct contact is important for the Dexter mechanism of photoluminescence quenching [162], which "can occur only when the fluorophore and quencher are close enough to allow orbital overlap" [163].

In this work we showed that one can use salt additions to alter the stability of the CNMs dispersions. Such, we predicted the "salting out" of CNTs from the stable CNT dispersions in N-methyl-2-pyrrolidone by addition of the NaI salt. This effect leads to an efficient safe and inexpensive method of regulating the CNT concentration in non-aqueous dispersions. In turn, the concentration of large molecular ions with long alkyl chains (like, tetraalkylammonium and 1-alkyl-3-methylimidazolium cations) could increase at the non-polar surfaces of the carbon nanomaterials, thus suggesting that organic salts comprising these ions might serve as "salting in" agents for CNMs in dispersions.

To increase stability of the CNMs dispersions chemists usually use surfactants, which considerably increase the solubility of CNMs. The surfactant molecules preferentially adsorb on the surface of the CNMs and prevent agglomeration of the dispersed particles. However, there is always a difficulty to remove the bulky polymer surfactant molecules at the end of the process. In the thesis we show that large ions (e.g. ion constituting organic salts or RTILs under this study) also can preferentially adsorb onto the CNM surface and, thus, are potentially good for stabilization of the CNM dispersions. The advantage to use such additions to common solvents instead of surfactants is the ease to remove the additions afterwards (indeed, the RTILs are also liquid solvents at room or slightly elevated temperatures, which could be washed out by an excess of aqueous or organic solvents). We believe that adjusting the strength of the interparticle correlations one can develop an efficient mixed solvent for the pristine carbon nanomaterials. To develop this point far more experimental and theoretical work is required.

One more direction for the future research would be the development of a simplistic model to describe preferential interaction of co-solvents with the surface of nanoobjects. Such model, operating with the effective parameters, like the length of co-solvent alkyl chain, ratio of the polar and non-polar surface area of the molecules, etc. should predict whether the addition of certain co-solvent would lead to stabilization or destabilization of the dispersion. A prerequisite that such model can be developed is that the interaction of ions with CNMs surfaces in different systems studied in the thesis could be rationalized by similar mechanisms. However, the development of such model would require more experimental and computer modelling data.

6 Literature

[1] F. Hofmeister. Zur lehre von der wirkung der salze. *Naunyn-Schmiedeberg's Archives of Pharmacology*, 24(4-5):247–260, 1988.

[2] Yizhak Marcus. *Ion solvation*. John Wiley & Sons, Chichester, UK, 1985.

[3] G. A. Krestov, N. P. Novosyolov, I. S. Perelygin, A. M. Kolker, L. P. Safonova, V. D. Ovchinnikova, and V. N. Trostin, editors. *Ionic solvation*. Ellis Horwood Series in Inorganic Chemistry. Horwood, New York, 1994.

[4] T. Fukushima, A. Kosaka, Y. Ishimura, T. Yamamoto, T. Takigawa, N. Ishii, and T. Aida. Molecular ordering of organic molten salts triggered by single-walled carbon nanotubes. *Science*, 300(5628):2072–2074, June 2003.

[5] C. Portet, G. Yushin, and Y. Gogotsi. Electrochemical performance of carbon onions, nanodiamonds, carbon black and multiwalled nanotubes in electrical double layer capacitors. *Carbon*, 45(13):2511–2518, November 2007.

[6] Y. J. Lee, H. Yi, W. J. Kim, K. Kang, D. S. Yun, M. S. Strano, G. Ceder, and A. M. Belcher. Fabricating genetically engineered high-power lithium-ion batteries using multiple virus genes. *Science*, 324(5930):1051–1055, May 2009.

[7] R. H. Baughman, A. A. Zakhidov, and W. A. de Heer. Carbon nanotubes - the route toward applications. *Science*, 297(5582):787–792, August 2002.

[8] D. Pech, M. Brunet, H. Durou, P. Huang, V. Mochalin, G. Gogotsi, P-L. Taberna, and P. Simon. Ultrahigh-power micrometre-sized supercapacitors based on onion-like carbon. *Nat Nano*, 5(9):651–654, 2010.

[9] B. J. Cox and J. M. Hill. A polyhedral model for carbon nanotubes. *SPIE Newsroom*, 2007, DOI: 10.1117/2.1200702.0806.

[10] D. Tasis, N. Tagmatarchis, A. Bianco, and M. Prato. Chemistry of carbon nanotubes. *Chemical Reviews*, 106(3):1105–1136, March 2006.

[11] T. J. Park, S. Banerjee, T. Hemraj-Benny, and S. S. Wong. Purification strategies and purity visualization techniques for single-walled carbon nanotubes. *Journal of Materials Chemistry*, 16(2):141–154, 2006.

[12] A. R. Boccaccini, J. Cho, J. A. Roether, B. J. C. Thomas, E. J. Minay, and M. S. P. Shaffer. Electrophoretic deposition of carbon nanotubes. *Carbon*, 44(15):3149–3160, December 2006.

[13] D. Mattia and Y. Gogotsi. Review: static and dynamic behavior of liquids inside carbon nanotubes. *Microfluidics and Nanofluidics*, 5(3):289–305, September 2008.

[14] L. Vaisman, H. D. Wagner, and G. Marom. The role of surfactants in dispersion of carbon nanotubes. *Advances in Colloid and Interface Science*, 128:37–46, December 2006.

[15] A. Hirsch. Functionalization of single-walled carbon nanotubes. *Angewandte Chemie-International Edition*, 41(11):1853–1859, 2002.

[16] A. Bianco, K. Kostarelos, C. D. Partidos, and M. Prato. Biomedical applications of functionalised carbon nanotubes. *Chemical Communications*, (5):571–577, 2005.

[17] S. C. Lin and D. Blankschtein. Role of the bile salt surfactant sodium cholate in enhancing the aqueous dispersion stability of single-walled carbon nanotubes: A molecular dynamics simulation study. *Journal of Physical Chemistry B*, 114(47):15616–15625, December 2010.

[18] S. D. Bergin, V. Nicolosi, H. Cathcart, M. Lotya, D. Rickard, Z. Y. Sun, W. J. Blau, and J. N. Coleman. Large populations of individual nanotubes in surfactant-based dispersions without the need for ultracentrifugation. *Journal of Physical Chemistry C*, 112(4):972–977, January 2008.

[19] N. R. Tummala and A. Striolo. Sds surfactants on carbon nanotubes: Aggregate morphology. *Acs Nano*, 3(3):595–602, March 2009.

[20] V. C. Moore, M. S. Strano, E. H. Haroz, R. H. Hauge, R. E. Smalley, J. Schmidt, and Y. Talmon. Individually suspended single-walled carbon nanotubes in various surfactants. *Nano Letters*, 3(10):1379–1382, October 2003.

[21] H. Cathcart, S. Quinn, V. Nicolosi, J. M. Kelly, W. J. Blau, and J. N. Coleman. Spontaneous debundling of single-walled carbon nanotubes in dna-based dispersions. *Journal of Physical Chemistry C*, 111(1):66–74, January 2007.

[22] B. G. Cousins, A. K. Das, R. Sharma, Y. N. Li, J. P. McNamara, I. H. Hillier, I. A. Kinloch, and R. V. Ulijn. Enzyme-activated surfactants for dispersion of carbon nanotubes. *Small*, 5(5):587–590, March 2009.

[23] F. Liang and B. Chen. A review on biomedical applications of single-walled carbon nanotubes. *Current Medicinal Chemistry*, 17(1):10–24, January 2010.

[24] E. Katz and I. Willner. Biomolecule-functionalized carbon nanotubes: Applications in nanobioelectronics. *Chemphyschem*, 5(8):1085–1104, August 2004.

[25] J. Berthier and P. Silberzan. *Microfluidics for Biotechnology*. Artech House, Boston, 2006.

[26] Y. Kim, N. Minami, W. H. Zhu, S. Kazaoui, R. Azumi, and M. Matsumoto. Langmuir-blodgett films of single-wall carbon nanotubes: Layer-by-layer deposition and in-plane orientation of tubes. *Japanese Journal of Applied Physics Part 1 - regular Papers Short Notes & Review Papers*, 42(12):7629–7634, December 2003.

[27] P. Beecher, P. Servati, A. Rozhin, A. Colli, V. Scardaci, S. Pisana, T. Hasan, A. J. Flewitt, J. Robertson, G. W. Hsieh, F. M. Li, A. Nathan, A. C. Ferrari, and W. I. Milne. Ink-jet printing of carbon nanotube thin film transistors. *Journal of Applied Physics*, 102(4):043710, August 2007.

[28] Y. Gogotsi, N. Naguib, and J. A. Libera. In situ chemical experiments in carbon nanotubes. *Chemical Physics Letters*, 365(3-4):354–360, November 2002.

[29] K. D. Ausman, R. Piner, O. Lourie, R. S. Ruoff, and M. Korobov. Organic solvent dispersions of single-walled carbon nanotubes: Toward solutions of pristine nanotubes. *Journal of Physical Chemistry B*, 104(38):8911–8915, September 2000.

[30] S. D. Bergin, Z. Y. Sun, P. Streich, J. Hamilton, and J. N. Coleman. New solvents for nanotubes: Approaching the dispersibility of surfactants. *Journal of Physical Chemistry C*, 114(1):231–237, January 2010.

[31] S. Giordani, S. Bergin, V. Nicolosi, S. Lebedkin, W. J. Blau, and J. N. Coleman. Fabrication of stable dispersions containing up to 70carbon nanotubes in a common organic solvent. *Physica Status Solidi B-basic Solid State Physics*, 243(13):3058–3062, November 2006.

[32] C. J. Shih, S. C. Lin, M. S. Strano, and D. Blankschtein. Understanding the stabilization of liquid-phase-exfoliated graphene in polar solvents: Molecular dynamics simulations and kinetic theory of colloid aggregation. *Journal of the American Chemical Society*, 132(41):14638–14648, October 2010.

[33] J. Wang, D. Fruchtl, Z. Y. Sun, J. N. Coleman, and W. J. Blau. Control of optical limiting of carbon nanotube dispersions by changing solvent parameters. *Journal of Physical Chemistry C*, 114(13):6148–6156, April 2010.

[34] D. Mac Kernan and W. J. Blau. Exploring the mechanisms of carbon-nanotube dispersion aggregation in a highly polar solvent. *Europhysics Letters*, 83(6):66009, September 2008.

[35] M. Armand, F. Endres, D. R. MacFarlane, H. Ohno, and B. Scrosati. Ionic-liquid materials for the electrochemical challenges of the future. *Nature Materials*, 8(8):621–629, August 2009.

[36] P. Simon and Y. Gogotsi. Materials for electrochemical capacitors. *Nature Materials*, 7(11):845–854, November 2008.

[37] G. P. Pandey, S. A. Hashmi, and Y. Kumar. Multiwalled carbon nanotube electrodes for electrical double layer capacitors with ionic liquid based gel polymer electrolytes. *Journal of the Electrochemical Society*, 157(1):A105–A114, 2010.

[38] N. P. Tarasova, Y. V. Smetannikov, and A. A. Zanin. Ionic liquids in the synthesis of nanoobjects. *Russian Chemical Reviews*, 79(6):463–477, 2010.

[39] D.S. Silvester and R.G. Compton. Electrochemistry in Room Temperature Ionic Liquids: A Review and Some Possible Applications. *Zeitschrift fur Physikalische Chemie*, 220(10):1247–1274, 2006.

[40] A. A. Kornyshev. Double-Layer in Ionic Liquids: Paradigm Change? *Journal of Physical Chemistry B*, 111(20):5545–5557, 2007.

[41] V. Lockett, R. Sedev, J. Ralston, M. Horne, and T. Rodopoulos. Differential capacitance of the electrical double layer in imidazolium-based ionic liquids: Influence of potential, cation size, and temperature. *Journal of Physical Chemistry C*, 112(19):7486–7495, 2008.

[42] F. Endres, D. MacFarlane, and A. Abbott, editors. *Electrodeposition from ionic liquids*. Wiley-VCH, 2008.

[43] S. Z. El Abedin, M. Polleth, S. A. Meiss, J. Janek, and F. Endres. Ionic liquids as green electrolytes for the electrodeposition of nanomaterials. *Green Chemistry*, 9(6):549–553, June 2007.

[44] A. Izadi-Najafabadi, S. Yasuda, K. Kobashi, T. Yamada, D. N. Futaba, H. Hatori, M. Yumura, S. Iijima, and K. Hata. Extracting the full potential of single-walled carbon nanotubes as durable supercapacitor electrodes operable at 4 v with high power and energy density. *Advanced Materials*, 22(35):E235–E241, September 2010.

[45] P. Simon and Y. Gogotsi. Charge storage mechanism in nanoporous carbons and its consequence for electrical double layer capacitors. *Philosophical Transactions of the Royal Society A-mathematical Physical and Engineering Sciences*, 368(1923):3457–3467, July 2010.

[46] H. Nakagawa, Y. Fujino, S. Kozono, Y. Katayama, T. Nukuda, H. Sakaebe, H. Matsumoto, and K. Tatsumi. Application of nonflammable electrolyte with room temperature ionic liquids (rtils) for lithium-ion cells. *Journal of Power Sources*, 174(2):1021–1026, December 2007.

[47] R. Lin, P. Huang, J. Segalini, C. Largeot, P. L. Taberna, J. Chmiola, Y. Gogotsi, and P. Simon. Solvent effect on the ion adsorption from ionic liquid electrolyte into subnanometer carbon pores. *Electrochimica Acta*, 54(27):7025–7032, November 2009.

[48] F. Endres. Ionic liquids: Solvents for the electrodeposition of metals and semiconductors. *Chemphyschem*, 3(2):144–154, February 2002.

[49] C. G. Liu, Z. N. Yu, D. Neff, A. Zhamu, and B. Z. Jang. Graphene-based supercapacitor with an ultrahigh energy density. *Nano Letters*, 10(12):4863–4868, December 2010.

[50] D. H. Lin, N. Liu, K. Yang, L. Z. Zhu, Y. Xu, and B. S. Xing. The effect of ionic strength and ph on the stability of tannic acid-facilitated carbon nanotube suspensions. *Carbon*, 47(12):2875–2882, October 2009.

[51] R. Atkin and G. G. Warr. Structure in confined room-temperature ionic liquids. *Journal of Physical Chemistry C*, 111(13):5162–5168, April 2007.

[52] V. Lockett, R. Sedev, S. Harmer, J. Ralston, M. Horne, and T. Rodopoulos. Orientation and mutual location of ions at the surface of ionic liquids. *Physical Chemistry Chemical Physics*, 12(41):13816–13827, 2010.

[53] V. Lockett, R. Sedev, C. Bassell, and J. Ralston. Angle-resolved x-ray photoelectron spectroscopy of the surface of imidazolium ionic liquids. *Physical Chemistry Chemical Physics*, 10(9):1330–1335, 2008.

[54] R. Atkin, S. Z. El Abedin, R. Hayes, L. H. S. Gasparotto, N. Borisenko, and F. Endres. Afm and stm studies on the surface interaction of [bmp]tfsa and (emim]tfsa ionic liquids with au(111). *Journal of Physical Chemistry C*, 113(30):13266–13272, July 2009.

[55] R. Hayes, S. Z. El Abedin, and R. Atkin. Pronounced structure in confined aprotic room-temperature ionic liquids. *Journal of Physical Chemistry B*, 113(20):7049–7052, May 2009.

[56] F. Endres, O. Hofft, N. Borisenko, L. H. Gasparotto, A. Prowald, R. Al-Salman, T. Carstens, R. Atkin, A. Bund, and S. Z. El Abedin. Do solvation layers of ionic liquids influence electrochemical reactions? *Physical Chemistry Chemical Physics*, 12(8):1724–1732, 2010.

[57] M. Druschler, B. Huber, and B. Roling. On capacitive processes at the interface between 1-ethyl-3-methylimidazolium tris(pentafluoroethyl)-trifluorophosphate and au(111). *Journal of Physical Chemistry C*, 115(14):6802–6808, April 2011.

[58] R. M. Lynden-Bell, J. Kohanoff, and M. G. Del Popolo. Simulation of interfaces between room temperature ionic liquids and other liquids. *Faraday Discussions*, 129:57–67, 2005.

[59] C. Pinilla, M.G. Del Po'polo, J. Kohanoff, and R.M. Lynden-Bell. Polarization relaxation in an ionic liquid confined between electrified walls. *Journal of Physical Chemistry B*, 111(18):4877–4884, 2007.

[60] R. M. Lynden-Bell, M. G. Del Popolo, T. G. A. Youngs, J. Kohanoff, C. G. Hanke, J. B. Harper, and C. C. Pinilla. Simulations of ionic liquids, solutions, and surfaces. *Accounts of Chemical Research*, 40:1138–1145, 2007.

[61] L. Yang, B. H. Fishbine, A. Migliori, and L. R. Pratt. Molecular simulation of electric double-layer capacitors based on carbon nanotube forests. *Journal of the American Chemical Society*, 131(34):12373–12376, September 2009.

[62] M. V. Fedorov and A. A. Kornyshev. Ionic liquid near a charged wall: Structure and capacitance of electrical double layer. *Journal of Physical Chemistry B*, 112(38):11868–11872, 2008.

[63] M. V Fedorov, N. Georgi, and A. A. Kornyshev. Double layer in ionic liquids: The nature of the camel shape of capacitance. *Electrochemistry Communications*, 12(2):296–299, 2010.

[64] N. Georgi, A. A. Kornyshev, and M. V. Fedorov. The anatomy of the double layer and capacitance in ionic liquids with anisotropic ions: Electrostriction vs. lattice saturation. *Journal of Electroanalytical Chemistry*, 649(1-2):261–267, 2010.

[65] Y. Shim and H. J. Kim. Nanoporous carbon supercapacitors in an ionic liquid: A computer simulation study. *Acs Nano*, 4(4):2345–2355, April 2010.

[66] J. Vatamanu, O. Borodin, and G. D. Smith. Molecular insights into the potential and temperature dependences of the differential capacitance of a room-temperature ionic liquid at graphite electrodes. *Journal of the American Chemical Society*, 132(42):14825–14833, October 2010.

[67] K. Nakajima, A. Ohno, H. Hashimoto, M. Suzuki, and K. Kimura. Observation of surface structure of 1-alkyl-3-methylimidazolium bis(trifluoromethanesulfonyl)imide using high-resolution rutherford backscattering spectroscopy. *Journal of Chemical Physics*, 133(4):044702, July 2010.

[68] H. Hashimoto, A. Ohno, K. Nakajima, M. Suzuki, H. Tsuji, and K. Kimura. Surface characterization of imidazolium ionic liquids by high-resolution rutherford backscattering spectroscopy and x-ray photoelectron spectroscopy. *Surface Science*, 604(3-4):464–469, February 2010.

[69] R. Atkin, N. Borisenko, M. Druschler, S. Z. El Abedin, F. Endres, R. Hayes, B. Huber, and B. Roling. An in situ stm/afm and impedance spectroscopy study of the extremely pure 1-butyl-1-methylpyrrolidinium tris(pentafluoroethyl) trifluorophosphate/au(111) interface: potential dependent solvation layers and the herringbone reconstruction. *Physical Chemistry Chemical Physics*, 13(15):6849–6857, 2011.

[70] R. Hayes, N. Borisenko, M. K. Tam, P. C. Howlett, F. Endres, and R. Atkin. Double layer structure of ionic liquids at the au(111) electrode interface: An atomic force microscopy investigation. *Journal of Physical Chemistry C*, 115(14):6855–6863, April 2011.

[71] K.D. Collins and M.W. Washabaugh. The Hofmeister effect and the behaviour of water at interfaces. *Quarterly Reviews of Biophysics*, 18(4):323–422, 1985.

[72] K. D. Collins. Ions from the hofmeister series and osmolytes: effects on proteins in solution and in the crystallization process. *Methods*, 34(3):300–311, November 2004.

[73] K. D. Collins. Ion hydration: Implications for cellular function, polyelectrolytes, and protein crystallization. *Biophysical Chemistry*, 119(3):271–281, February 2006.

[74] D. V. Schur, B. P. Tarasov, S. Y. Zaginaichenko, V. K. Pishuk, T. N. Veziroglu, Y. M. Shul'ga, A. G. Dubovoi, N. S. Anikina, A. P. Pomytkin, and A. D. Zolotarenko. The prospects for using of carbon nanomaterials as hydrogen storage systems. *International Journal of Hydrogen Energy*, 27(10):1063–1069, October 2002.

[75] R. Hidalgo-Alvarez, A. Martin, A. Fernandez, D. Bastos, F. Martinez, and F. J. de las Nieves. Electrokinetic properties, colloidal stability and aggregation kinetics of polymer colloids. *Advances in Colloid and Interface Science*, 67:1–118, September 1996.

[76] J. L. Ortega-Vinuesa, A. Martin-Rodriguez, and R. H. Hidalgo-Alvarez. Colloidal stability of polymer colloids with different interfacial properties: Mechanisms. *Journal of Colloid and Interface Science*, 184(1):259–267, December 1996.

[77] S. V. Solomatin, T. K. Bronich, A. Eisenberg, V. A. Kabanov, and A. V. Kabanov. Colloidal stability of aqueous dispersions of block ionomer complexes: Effects of temperature and salt. *Langmuir*, 20(6):2066–2068, March 2004.

[78] M. V. Fedorov, J. M. Goodman, and S. Schumm. To switch or not to switch: The effects of potassium and sodium ions on alpha-poly-l-glutamate conformations in aqueous solutions. *Journal of the American Chemical Society*, 131(31):10854–10856, August 2009.

[79] M. Lund, R. Vacha, and P. Jungwirth. Specific ion binding to macromolecules: Effects of hydrophobicity and ion pairing. *Langmuir*, 24(7):3387–3391, April 2008.

[80] S. Niyogi, S. Boukhalfa, S. B. Chikkannanavar, T. J. McDonald, M. J. Heben, and S. K. Doorn. Selective aggregation of single-walled carbon nanotubes via salt addition. *Journal of the American Chemical Society*, 129(7):1898–1899, February 2007.

[81] S. Niyogi, C. G. Densmore, and S. K. Doom. Electrolyte tuning of surfactant interfacial behavior for enhanced density-based separations of single-walled carbon nanotubes. *Journal of the American Chemical Society*, 131(3):1144–1153, January 2009.

[82] J.J. Brege, C. Gallaway, and A.R. Barron. Fluorescence Quenching of Single-Walled Carbon Nanotubes in SDBS Surfactant Suspension by Metal Ions: Quenching Efficiency as a Function of Metal and Nanotube Identity. *Journal of Physical Chemistry C*, 111:17812–17820, 2007.

[83] J. J. Brege, C. Gallaway, and A. R. Barron. Fluorescence quenching of single-walled carbon nanotubes with transition-metal ions. *Journal of Physical Chemistry C*, 113(11):4270–4276, March 2009.

[84] S. Y. Ju, J. Doll, I. Sharma, and F. Papadimitrakopoulos. Selection of carbon nanotubes with specific chiralities using helical assemblies of flavin mononucleotide. *Nature Nanotechnology*, 3(6):356–362, June 2008.

[85] E. Lu, N. Rodriguez-Hornedo, and R. Suryanarayanan. A rapid thermal method for cocrystal screening. *Crystengcomm*, 10(6):665–668, 2008.

[86] S. M. Bachilo, M. S. Strano, C. Kittrell, R. H. Hauge, R. E. Smalley, and R. B. Weisman. Structure-assigned optical spectra of single-walled carbon nanotubes. *Science*, 298(5602):2361–2366, December 2002.

[87] M. J. O'Connell, S. M. Bachilo, C. B. Huffman, V. C. Moore, M. S. Strano, E. H. Haroz, K. L. Rialon, P. J. Boul, W. H. Noon, C. Kittrell, J. P. Ma, R. H. Hauge, R. B. Weisman, and R. E. Smalley. Band gap fluorescence from individual single-walled carbon nanotubes. *Science*, 297(5581):593–596, July 2002.

[88] P. H. Tan, A. G. Rozhin, T. Hasan, P. Hu, V. Scardaci, W. I. Milne, and A. C. Ferrari. Photoluminescence spectroscopy of carbon nanotube bundles: Evidence for exciton energy transfer. *Physical Review Letters*, 99(13):137402, September 2007.

[89] A. Ahmad, K. Kern, and K. Balasubramanian. Selective enhancement of carbon nanotube photoluminescence by resonant energy transfer. *Chemphyschem*, 10(6):905–909, April 2009.

[90] T. Hasan, Z. P. Sun, F. Q. Wang, F. Bonaccorso, P. H. Tan, A. G. Rozhin, and A. C. Ferrari. Nanotube-polymer composites for ultrafast photonics. *Advanced Materials*, 21(38-39):3874–3899, October 2009.

[91] W. E. Willy, D. R. Mckean, and B. A. Garcia. Conversion of alkyl chlorides to bromides,

selective reactions of mixed bromochloroalkanes, and halogen exchange. *Bulletin of the Chemical Society of Japan*, 49(7):1989–1995, 1976.

[92] G. W. Neilson and N. Skipper. K^+ coordination in aqueous-solution. *Chemical Physics Letters*, 114(1):35–38, 1985.

[93] T. L. Hill. *Statistical Mechanics: Principles and Selected Applications*. Dover Publications, July 1987.

[94] A. Ben-Naim. *Molecular Theory of Solutions*. Oxford University Press, USA, 2006.

[95] O. Ya. Samoilov. A new approach to the study of hydration of ions in aqueous solutions. *Discussions of the Faraday Society*, 24:141–146, 1957.

[96] S. H. Chong and F. Hirata. Ion hydration: Thermodynamic and structural analysis with an integral equation theory of liquids. *Journal of Physical Chemistry B*, 101(16):3209–3220, April 1997.

[97] S. Koneshan, J. C. Rasaiah, R. M. Lynden-Bell, and S. H. Lee. Solvent structure, dynamics, and ion mobility in aqueous solutions at $25^{/circ}$c. *Journal of Physical Chemistry B*, 102(21):4193–4204, May 1998.

[98] R. W. Impey, P. A. Madden, and I. R. Mcdonald. Hydration and mobility of ions in solution. *Journal of Physical Chemistry*, 87(25):5071–5083, 1983.

[99] J. C. Rasaiah and R. M. Lynden-Bell. Computer simulation studies of the structure and dynamics of ions and non-polar solutes in water. *Philosophical Transactions of the Royal Society of London. Series A-Mathematical Physical and Engineering Sciences*, 359(1785):1545–1574, August 2001.

[100] http://www.iupac.org/goldbook/st07102.pdf.

[101] M. V. Fedorov and A. A. Kornyshev. Unravelling the solvent response to neutral and charged solutes. *Molecular Physics*, 105(1):1–16, January 2007.

[102] Y. Marcus. A simple empirical-model describing the thermodynamics of hydration of ions of widely varying charges, sizes, and shapes. *Biophysical Chemistry*, 51(2-3):111–127, August 1994.

[103] R. D. Shannon. Revised effective ionic-radii and systematic studies of interatomic distances in halides and chalcogenides. *Acta Crystallographica Section A*, 32(SEP1):751–767, 1976.

[104] R. M. Lynden-Bell and J. C. Rasaiah. From hydrophobic to hydrophilic behaviour: A simulation study of solvation entropy and free energy of simple solutes. *Journal of Chemical Physics*, 107(6):1981–1991, August 1997.

[105] K. D. Collins, G. W. Neilson, and J. E. Enderby. Ions in water: Characterizing the forces that control chemical processes and biological structure. *Biophysical Chemistry*, 128(2-3):95–104, July 2007.

[106] K. D. Collins. Charge density-dependent strength of hydration and biological structure. *Biophysical Journal*, 72(1):65–76, January 1997.

[107] Werner Kunz. *Specific Ion Effects*. World Scientific Publishing Company, 1 edition, December 2009.

[108] Daan Frenkel and Berend Smit. *Understanding molecular simulation*. Academic Press, 2002.

[109] M. P. Allen and D. J. Tildesley. *Computer Simulation of Liquids*. Oxford University Press; Clarendon Press, 1989.

[110] S. W. Rick and S. J. Stuart. *Reviews in computational chemistry*, volume 18, chapter Potentials and Algorithms for Incorporating Polarizability in Computer Simulations. VCH Publisher, New York, 2002.

[111] M. Deserno and C. Holm. How to mesh up ewald sums. i. a theoretical and numerical comparison of various particle mesh routines. *Journal of Chemical Physics*, 109(18):7678–7693, November 1998.

[112] U. Essmann, L. Perera, M. L. Berkowitz, T. Darden, H. Lee, and L. G. Pedersen. A smooth particle mesh ewald method. *Journal of Chemical Physics*, 103(19):8577–8593, November 1995.

[113] T. Darden, D. York, and L. Pedersen. Particle mesh Ewald: An N log (N) method for Ewald sums in large systems. *Journal of Chemical Physics*, 98:10089–10092, 1993.

[114] M. Deserno and C. Holm. How to mesh up ewald sums. ii. an accurate error estimate for the particle-particle-particle-mesh algorithm. *Journal of Chemical Physics*, 109(18):7694–7701, November 1998.

[115] C. Sagui and T. A. Darden. Molecular dynamics simulations of biomolecules: Long-range electrostatic effects. *Annual Review of Biophysics and Biomolecular Structure*, 28:155–179, 1999.

[116] E. L. Pollock and J. Glosli. Comments on p(3)m, fmm, and the ewald method for large periodic coulombic systems. *Computer Physics Communications*, 95(2-3):93–110, June 1996.

[117] J. H. Walther, R. Jaffe, T. Halicioglu, and P. Koumoutsakos. Carbon nanotubes in water: Structural characteristics and energetics. *Journal of Physical Chemistry B*, 105(41):9980–9987, October 2001.

[118] G. Hummer, J. C. Rasaiah, and J. P. Noworyta. Water conduction through the hydrophobic channel of a carbon nanotube. *Nature*, 414(6860):188–190, November 2001.

[119] J. W. Shen, T. Wu, Q. Wang, Y. Kang, and X. Chen. Adsorption of insulin peptide on charged single-walled carbon nanotubes: Significant role of ordered water molecules. *Chemphyschem*, 10(8):1260–1269, June 2009.

[120] R. J. Chen, S. Bangsaruntip, K. A. Drouvalakis, N. W. S. Kam, M. Shim, Y. M. Li, W. Kim, P. J. Utz, and H. J. Dai. Noncovalent functionalization of carbon nanotubes for highly specific electronic biosensors. *Proceedings of the National Academy of Sciences of the United States of America*, 100(9):4984–4989, April 2003.

[121] W. Kunz. Specific ion effects in liquids, in biological systems, and at interfaces. *Pure and Applied Chemistry*, 78(8):1611–1617, August 2006.

[122] P. Jungwirth and D. J. Tobias. Molecular structure of salt solutions: A new view of the interface with implications for heterogeneous atmospheric chemistry. *Journal of Physical Chemistry B*, 105(43):10468–10472, November 2001.

[123] L. Vrbka, P. Jungwirth, P. Bauduin, D. Touraud, and W. Kunz. Specific ion effects at protein surfaces: A molecular dynamics study of bovine pancreatic trypsin inhibitor and horseradish peroxidase in selected salt solutions. *Journal of Physical Chemistry B*, 110(13):7036–7043, 2006.

[124] M. Lund and P. Jungwirth. Ion specific protein assembly and hydrophobic surface forces. *Physical Review Letters*, 100(25):258105, June 2008.

[125] D. Van der Spoel, E. Lindahl, B. Hess, G. Groenhof, A. E. Mark, and H. J. C. Berendsen. Gromacs: Fast, flexible, and free. *Journal of Computational Chemistry*, 26(16):1701–1718, December 2005.

[126] J. T. Frey and D. J. Doren. Tubegen 3.4. web-interface, 2011.

[127] W. L. Jorgensen and D. L. Severance. Aromatic aromatic interactions - free-energy profiles for the benzene dimer in water, chloroform, and liquid benzene. *Journal of the American Chemical Society*, 112(12):4768–4774, June 1990.

[128] W. L. Jorgensen, J. Chandrasekhar, J. D. Madura, R. W. Impey, and M. L. Klein. Comparison of simple potential functions for simulating liquid water. *Journal of Chemical Physics*, 79(2):926–935, 1983.

[129] J. Aqvist. Ion-water interaction potentials derived from free-energy perturbation simulations. *Journal of Physical Chemistry*, 94(21):8021–8024, October 1990.

[130] J. Chandrasekhar, D. C. Spellmeyer, and W. L. Jorgensen. Energy component analysis for dilute aqueous-solutions of li+, na+, f-, and cl- ions. *Journal of the American Chemical Society*, 106(4):903–910, 1984.

[131] T. P. Lybrand, I. Ghosh, and J. A. Mccammon. Hydration of chloride and bromide anions - determination of relative free-energy by computer-simulation. *Journal of the American Chemical Society*, 107(25):7793–7794, 1985.

[132] N. A. McDonald and W. L. Jorgensen. Development of an all-atom force field for heterocycles. properties of liquid pyrrole, furan, diazoles, and oxazoles. *Journal of Physical Chemistry B*, 102(41):8049–8059, October 1998.

[133] H. W. Horn, W. C. Swope, J. W. Pitera, J. D. Madura, T. J. Dick, G. L. Hura, and T. Head-Gordon. Development of an improved four-site water model for biomolecular simulations: TIP4P-Ew. *Journal of Chemical Physics*, 120(20):9665–9678, May 2004.

[134] I. S. Joung and T. E. Cheatham. Determination of alkali and halide monovalent ion parameters for use in explicitly solvated biomolecular simulations. *Journal of Physical Chemistry B*, 112(30):9020–9041, July 2008.

[135] R. W. Hockney, S. P. Goel, and J. W. Eastwood. Quiet high-resolution computer models of a plasma. *Journal of Computational Physics*, 14(2):148–158, 1974.

[136] S. Nose. A molecular-dynamics method for simulations in the canonical ensemble. *Molecular Physics*, 52(2):255–268, 1984.

[137] W. G. Hoover. Canonical dynamics: Equilibrium phase-space distributions. *Physical Review A*, 31(3):1695–1697, 1985.

[138] H. J. C. Berendsen, J. P. M. Postma, W. F. van Gunsteren, A. Dinola, and J. R. Haak. Molecular dynamics with coupling to an external bath. *Journal of Chemical Physics*, 81(8):3684–3690, 1984.

[139] O. Ia. Samoilov, editor. *Structure of aqueous electrolyte solutions and the hydration of ions*. Consultants Bureau, New York, 1965.

[140] Y. Marcus. The thermodynamics of solvation of ions .2. the enthalpy of hydration at 298.15-k. *Journal of the Chemical Society-faraday Transactions I*, 83:339–349, 1987.

[141] Y. Marcus. Ionic-radii in aqueous-solutions. *Chemical Reviews*, 88(8):1475–1498, December 1988.

[142] N. Matubayasi, L. H. Reed, and R. M. Levy. Thermodynamics of the hydration shell .1. excess energy of a hydrophobic solute. *Journal of Physical Chemistry*, 98(41):10640–10649, October 1994.

[143] N. Matubayasi, E. Gallicchio, and R. M. Levy. On the local and nonlocal components of solvation thermodynamics and their relation to solvation shell models. *Journal of Chemical Physics*, 109(12):4864–4872, September 1998.

[144] E. Spohr, G. Toth, and K. Heinzinger. Structure and dynamics of water and hydrated ions near platinum and, mercury surfaces as studied by md simulations. *Electrochimica Acta*, 41(14):2131–2144, 1996.

[145] E. Spohr. Some recent trends in computer simulations of aqueous double layers. *Electrochimica Acta*, 49(1):23–27, 2003.

[146] L. Perera and M. L. Berkowitz. Free-energy profiles for li+ and i- ions approaching the pt(100) surface - a molecular-dynamics study. *Journal of Physical Chemistry*, 97(51):13803–13806, December 1993.

[147] E. Spohr. Molecular dynamics simulations of water and ion dynamics in the electrochemical double layer. *Solid State Ionics*, 150(1-2):1–12, 2002.

[148] E. Spohr, P. Commer, and A. A. Kornyshev. Enhancing proton mobility in polymer electrolyte membranes: Lessons from molecular dynamics simulations. *Journal of Physical Chemistry B*, 106(41):10560–10569, October 2002.

[149] D. Chandler. Interfaces and the driving force of hydrophobic assembly. *Nature*, 437(7059):640–647, September 2005.

[150] M. Kinoshita and Y. Harano. Potential of mean force between solute atoms in salt solution: Effects due to salt species and relevance to conformational transition of biomolecules. *Bulletin of the Chemical Society of Japan*, 78(8):1431–1441, August 2005.

[151] M.V. Fedorov, J.M. Goodman, and S. Schumm. Solvent effects and hydration of a tripeptide in sodium halide aqueous solutions: an in silico study. *Physical Chemistry Chemical Physics*, 9(40):5423–5435, 2007.

[152] A. K. Soper and K. Weckstrom. Ion solvation and water structure in potassium halide aqueous solutions. *Biophysical Chemistry*, 124(3):180–191, December 2006.

[153] R. Mancinelli, A. Botti, F. Bruni, M. A. Ricci, and A. K. Soper. Perturbation of water structure due to monovalent ions in solution. *Physical Chemistry Chemical Physics*, 9(23):2959–2967, 2007.

[154] V. Mile, L. Pusztai, H. Dominguez, and O. Pizio. Understanding the structure of aqueous cesium chloride solutions by combining diffraction experiments, molecular dynamics simulations, and reverse monte carlo modeling. *Journal of Physical Chemistry B*, 113(31):10760–10769, August 2009.

[155] K. Ibuki and P. A. Bopp. Molecular dynamics simulations of aqueous licl solutions at room temperature through the entire concentration range. *Journal of Molecular Liquids*, 147(1-2):56–63, July 2009.

[156] A. V. Egorov, A. V. Komolkin, V. I. Chizhik, P. V. Yushmanov, A. P. Lyubartsev, and A. Laaksonen. Temperature and concentration effects on li+-ion hydration. a molecular dynamics simulation study. *Journal of Physical Chemistry B*, 107(14):3234–3242, April 2003.

[157] I. Howell and G. W. Neilson. Li+ hydration in concentrated aqueous solution. *Journal of Physics-condensed Matter*, 8(25):4455–4463, June 1996.

[158] I. Harsanyi and L. Pusztai. On the structure of aqueous licl solutions. *Journal of Chemical Physics*, 122(12):124512, March 2005.

[159] S. H. Lee and J. C. Rasaiah. Molecular dynamics simulation of ion mobility. II. Alkali metal and halide ions using the spc/e model for water at $25^{/circ}$c. *Journal of Physical Chemistry*, 100(4):1420–1425, January 1996.

[160] C. Hayakawa, K. Urita, T. Ohba, H. Kanoh, and K. Kaneko. Physico-chemical properties of iodine-adsorbed single-walled carbon nanotubes. *Langmuir*, 25(3):1795–1799, February 2009.

[161] S. Pal and F. Muller-Plathe. Molecular dynamics simulation of aqueous NaF and NaI solutions near a hydrophobic surface. *Journal of Physical Chemistry B*, 109(13):6405–6415, 2005.

[162] D. L. Dexter. A theory of sensitized luminescence in solids. *Journal of Chemical Physics*, 21(5):836–850, 1953.

[163] M. K. Johansson, H. Fidder, D. Dick, and R. M. Cook. Intramolecular dimers: A new strategy to fluorescence quenching in dual-labeled oligonucleotide probes. *Journal of the American Chemical Society*, 124(24):6950–6956, June 2002.

[164] S. Giordani, S. D. Bergin, V. Nicolosi, S. Lebedkin, M. M. Kappes, W. J. Blau, and J. N. Coleman. Debundling of single-walled nanotubes by dilution: Observation of large populations of individual nanotubes in amide solvent dispersions. *Journal of Physical Chemistry B*, 110(32):15708–15718, August 2006.

[165] A. Domard, M. Rinaudo, and C. Terrassin. New method for the quaternization of chitosan. *International Journal of Biological Macromolecules*, 8(2):105–107, April 1986.

[166] T. Hasan, V. Scardaci, P. H. Tan, A. G. Rozhin, W. I. Milne, and A. C. Ferrari. Stabilization and "debundling" of single-wall carbon nanotube dispersions in n-methyl-2-pyrrolidone (nmp) by polyvinylpyrrolidone (pvp). *Journal of Physical Chemistry C*, 111(34):12594–12602, August 2007.

[167] B. Hess, C. Kutzner, D. van der Spoel, and E. Lindahl. Gromacs 4: Algorithms for highly efficient, load-balanced, and scalable molecular simulation. *Journal of Chemical Theory and Computation*, 4(3):435–447, March 2008.

[168] W. L. Jorgensen, D. S. Maxwell, and J. TiradoRives. Development and testing of the opls all-atom force field on conformational energetics and properties of organic liquids. *Journal of the American Chemical Society*, 118(45):11225–11236, November 1996.

[169] M. L. P. Price, D. Ostrovsky, and W. L. Jorgensen. Gas-phase and liquid-state properties of esters, nitriles, and nitro compounds with the opls-aa force field. *Journal of Computational Chemistry*, 22(13):1340–1352, October 2001.

[170] K. P. Jensen and W. L. Jorgensen. Halide, ammonium, and alkali metal ion parameters for modeling aqueous solutions. *Journal of Chemical Theory and Computation*, 2(6):1499–1509, November 2006.

[171] S. Aparicio, R. Alcalde, M. J. Davila, B. Garcia, and J. M. Leal. Measurements and predictive models for the n-methyl-2-pyrrolidone/water/methanol system. *Journal of Physical Chemistry B*, 112(36):11361–11373, September 2008.

[172] S. Aparicio and R. Alcalde. Characterization of two lactones in liquid phase: an experimental and computational approach. *Physical Chemistry Chemical Physics*, 11(30):6455–6467, 2009.

[173] *Maestro 9.1 User Manual*, May 2010.

[174] D. van der Spoel, E. Lindahl, B. Hess, A. R. van Buuren, E. Apol, P. J. Meulenhoff, D. P. Tieleman, A. L. T. M. Sijbers, K. A. Feenstra, R. van Drunen, and H. J. C. Berendsen. *Gromacs User Manual version 4.5*, 2010. GROMACS - Groningen Machine for Chemical Simulations; User Manual.

[175] B. Hess, H. Bekker, H. J. C. Berendsen, and J. G. E. M. Fraaije. Lincs: A linear constraint solver for molecular simulations. *Journal of Computational Chemistry*, 18(12):1463–1472, September 1997.

[176] L. Martinez, R. Andrade, E. G. Birgin, and J. M. Martinez. Packmol: A package for building initial configurations for molecular dynamics simulations. *Journal of Computational Chemistry*, 30(13):2157–2164, October 2009.

[177] R. M. Levy, L. Y. Zhang, E. Gallicchio, and A. K. Felts. On the nonpolar hydration free energy of proteins: Surface area and continuum solvent models for the solute-solvent interaction energy. *Journal of the American Chemical Society*, 125(31):9523–9530, August 2003.

[178] V. A. Parsegian, R. P. Rand, and D. C. Rau. Osmotic stress, crowding, preferential hydration, and binding: A comparison of perspectives. *Proceedings of the National Academy of Sciences of the United States of America*, 97(8):3987–3992, April 2000.

[179] A. I. Frolov, A. G. Rozhin, and M. V. Fedorov. Ion interactions with the carbon nanotube surface in aqueous solutions: Understanding the molecular mechanisms. *ChemPhysChem*, 11(12):2612–2616, 2010.

[180] J. G. Kirkwood and F. P. Buff. The statistical mechanical theory of solutions .1. *Journal of Chemical Physics*, 19(6):774–777, 1951.

[181] S. Shimizu, W. M. McLaren, and N. Matubayasi. The hofmeister series and protein-salt interactions. *Journal of Chemical Physics*, 124(23):234905, June 2006.

[182] J. M. Schurr, D. P. Rangel, and S. R. Aragon. A contribution to the theory of preferential interaction coefficients. *Biophysical Journal*, 89(4):2258 – 2276, 2005.

[183] I. L. Shulgin and E. Ruckenstein. A protein molecule in a mixed solvent: The preferential binding parameter via the kirkwood-buff theory. *Biophysical Journal*, 90(2):704–707, January 2006.

[184] N. Matubayasi, W. Shinoda, and M. Nakahara. Free-energy analysis of the molecular binding into lipid membrane with the method of energy representation. *Journal of Chemical Physics*, 128(19):195107, May 2008.

[185] R. Chitra and P. E. Smith. Preferential interactions of cosolvents with hydrophobic solutes. *Journal of Physical Chemistry B*, 105(46):11513–11522, November 2001.

[186] P. G. Kusalik and G. N. Patey. The thermodynamic properties of electrolyte-solutions - some formal results. *Journal of Chemical Physics*, 86(9):5110–5116, May 1987.

[187] Maxim V. Fedorov, Raz N. Arif, Andrey I. Frolov, Martin Kolar, Anastasia O. Romanova, and Aleksey G. Rozhin. Salting out in organic solvents: a new route to carbon nanotube bundle engineering. *Physical Chemistry Chemical Physics*, 2011.

[188] G. Feng, J. S. Huang, B. G. Sumpter, V. Meunier, and R. Qiao. Structure and dynamics of electrical double layers in organic electrolytes. *Physical Chemistry Chemical Physics*, 12(20):5468–5479, 2010.

[189] Giovanni Bussi, Davide Donadio, and Michele Parrinello. Canonical sampling through velocity rescaling. *The Journal of Chemical Physics*, 126(1):014101, January 2007.

[190] J. N. C. Lopes and A. A. H. Padua. Molecular force field for ionic liquids composed of triflate or bistriflylimide anions. *Journal of Physical Chemistry B*, 108(43):16893–16898, October 2004.

[191] J. N. C. Lopes, J. Deschamps, and A. A. H. Padua. Modeling ionic liquids using a systematic all-atom force field. *Journal of Physical Chemistry B*, 108(6):2038–2047, February 2004.

[192] M. J. Frisch, G. W. Trucks, H. B. Schlegel, G. E. Scuseria, M. A. Robb, J. R. Cheeseman, Montgomery, Jr., J. A., T. Vreven, K. N. Kudin, J. C. Burant, J. M. Millam, S. S. Iyengar, J. Tomasi, V. Barone, B. Mennucci, M. Cossi, G. Scalmani, N. Rega, G. A. Petersson, H. Nakatsuji, M. Hada, M. Ehara, K. Toyota, R. Fukuda, J. Hasegawa, M. Ishida, T. Nakajima, Y. Honda, O. Kitao, H. Nakai, M. Klene, X. Li, J. E. Knox, H. P. Hratchian, J. B. Cross, V. Bakken, C. Adamo, J. Jaramillo, R. Gomperts, R. E. Stratmann, O. Yazyev, A. J. Austin, R. Cammi, C. Pomelli, J. W. Ochterski, P. Y. Ayala, K. Morokuma, G. A. Voth, P. Salvador, J. J. Dannenberg, V. G. Zakrzewski, S. Dapprich, A. D. Daniels, M. C. Strain, O. Farkas, D. K. Malick, A. D. Rabuck, K. Raghavachari, J. B. Foresman, J. V. Ortiz, Q. Cui, A. G. Baboul, S. Clifford, J. Cioslowski, B. B. Stefanov, G. Liu, A. Liashenko, P. Piskorz, I. Komaromi, R. L. Martin, D. J. Fox, T. Keith, M. A. Al-Laham, C. Y. Peng, A. Nanayakkara, M. Challacombe, P. M. W. Gill, B. Johnson, W. Chen, M. W. Wong, C. Gonzalez, and J. A. Pople. *Gaussian 03*. Gaussian, Inc., Wallingford, CT, 2004.

[193] J. B. Foresman, T. A. Keith, K. B. Wiberg, J. Snoonian, and M. J. Frisch. Solvent effects .5. influence of cavity shape, truncation of electrostatics, and electron correlation ab initio reaction field calculations. *Journal of Physical Chemistry*, 100(40):16098–16104, October 1996.

[194] W. Humphrey, A. Dalke, and K. Schulten. VMD: Visual molecular dynamics. *Journal of Molecular Graphics*, 14(1):33–38, February 1996.

7 Appendix

7.1 List of Abbreviations

2D	two dimensional
3D	three dimensional
AFM	atomic force microscopy
AN	acetonitrile
B3LYP	Becke, three-parameter, Lee-Yang-Parr exchange-correlation functional
BMIm	1-butyl-3-methylimidazolium
CNM	carbon nanomaterials
CNO	carbon nanoonion
CNT	carbon nanotube
EDL	electrical double layer
EDLC	electrical double layer capacitors
EMIm	1-ethyl-3-methylimidazolium
FAP	tris(pentafluoroethyl)trifluorophosphate
FFT	fast Fourier transform
HS	hydration shell
IL	ionic liquid
KB	Kirkwood-Buff
LJ	Lennard-Jones
MD	molecular dynamics
MIm	3-methylimidazolium

NMP	N-methyl-2-pyrrolidone
OMIm	1-octyl-3-methylimidazolium
OPLS-AA	optimized potential for liquid simulations – all atom
PBC	periodic boundary conditions
PCF	pair correlation function
PME	particle mesh Ewald
PMF	potential of mean force
PPPM	particle-particle particle-mesh Ewald
Py	1-butyl-1-methylpyrrolidinium
QM	quantum mechanical or quantum mechanics
RDF	radial distribution function
RDP	radial density profile
RPM	revolutions per minute
RTIL	room-temperature ionic liquid
SCI-PCM	Self consistent isodensity polarizable continuum model
SPME	smooth particle mesh Ewald
SS	solvation shell
SWNT	single-wall carbon nanotube
TBA^+	tetrabutylammonium
TBA-BF4,$TBA^+BF_4^-$	tetrabutylammonium tetrafluoroborate
TEA^+	tetraethylammonium
TEA-BF4,$TEA^+BF_4^-$	tetraethylammonium tetrafluoroborate
TEM	transmission electron microscopy
TFSA	bis(trifluoromethylsulfonyl)amide

TFSI	bis(trifluoromethylsulfonyl)imide
TIP4P	four-point transferable intermolecular potential
TIP4Pew	four-point transferable intermolecular potential optimized for Ewald summation

7.2 Short summary

In this thesis we investigated ion interactions with the surfaces of carbon nanomaterials dispersed in different aqueous and non-aqueous solvents: aqueous dispersions, N-methyl-2-pyrrolidone dispersions, organic salt/acetonitrile dispersions and room temperature ionic liquids/acetonitrile dispersions. We used molecular dynamics simulations to understand the molecular-scale mechanisms of ion interactions with the CNM surfaces. We considered carbon nanotube and carbon "nanoonion" structures as representatives of the CNMs. Despite the high diversity of the system compositions studied in the thesis, the main features of ion interactions with CNM surfaces can be rationalized by similar mechanisms:

1. Interaction of ions with the CNT surface in dispersions are determined by the interplay of the particle-particle interactions: ion-solvent, CNT-solvent, solvent-solvent and ion-CNT interactions.

2. To make direct contacts with the carbon nanomaterial surface, ions have to become partially desolvated. The partial desolvation might be, however, energetically favorable or unfavorable depending on the strength of ion-solvent interactions. In this thesis we show that there is a strong negative correlation between the strength of ion solvation and the probability of a direct CNM-ion contact: the interfacial region becomes increasingly populated by weakly solvated ions.

3. The penalty for the partial desolvation of CNM surface adds an additional energetic "barrier" for ions to come close to the CNM surface. This can be low (like in the case of aqueous dispersions) and thus will not prevent ions to come to the surface, or it can be high (like in the case of N-methyl-2-pyrrolidone dispersions) and, thus, will prevent ions to come to the CNM surface.

In this thesis we compare the structure of the electric double layer (EDL) at a CNM electrode for a neat ionic liquid (EMIm-TFSI) and its mixture with an organic solvent (acetonitrile). Mixing RTIL with acetonitrile decreases the ion-counterion correlations in the EDL.

In this work we showed that one can use salt addition to alter the stability of the CNMs dispersions. Such, we predicted the "salting out" of CNTs from the stable CNT dispersions in N-methyl-2-pyrrolidone. This effect leads to an efficient safe and inexpensive method of regulating the CNT concentration in non-aqueous dispersions.

7.3 List of Publications

Peer-reviewed publications

a) submitted manuscripts:

1. **Frolov A. I.**, Arif R. N., Kolar M., Romanova A. O., Fedorov M. V., Rozhin A. G., "Molecular mechanisms of salt effects on carbon nanotube dispersions in an organic solvent (N-methyl-2-pyrrolidone)", *Chem. Sci.* **2011**, (under review).

b) accepted manuscripts:

1. **Frolov A. I.**, Kirchner K., Kirchner T., Fedorov M. V., "Molecular-scale insights into the mechanisms of ionic liquids interactions with carbon nanotubes", *Faraday Discuss.* **2011**, (in press).
2. Palmer D. S., **Frolov A. I.**, Ratkova E. L., Fedorov M. V., "Towards a Universal Model to Calculate the Solvation Thermodynamics of Druglike Molecules: The Importance of New Experimental Databases", *Mol. Pharmaceutics* **2011** (in press), DOI: 10.1021/mp200119r.
3. Fedorov M. V., Arif R. N., **Frolov A. I.**, Kolar M., Romanova A. O., Rozhin A. G., "Salting out in Organic Solvent: A New Route to Carbon Nanotube Bundle Engineering", *Phys. Chem. Chem. Phys.* **2011**, (in press), DOI: 10.1039/C1CP21440C.

c) published articles:

1. **Frolov A. I.**, Ratkova E. L., Palmer D. S., Fedorov, M. V., "Hydration Thermodynamics using the Reference Interaction Site Model: Speed or Accuracy?", *J. Phys. Chem. B* **2011**, *115*, 6011-6022.
2. Palmer S., **Frolov A. I.**, Ratkova E. L., Fedorov M. V., "Towards a universal method to calculate hydration free energies: a 3D reference interaction site model with partial molar volume correction", *J. Phys.: Cond. Matt.* **2010**, *22*, 492101.
3. **Frolov A. I.**, Rozhin A. G., Fedorov M. V., "Ion Interactions with the Carbon Nanotube Surface in Aqueous Solutions: Understanding the Molecular Mechanisms", *ChemPhysChem* **2010**, *11*, 2612-2616.
4. Kolombet V. A., **Frolov A. I.**, "Na^+/K^+-selectivity at ion pairing in water solutions", *Russian J. Phys. Chem. B* **2010**, *4*, 875-882.

5. Idrissi A., Vyalov I., Damay P., **Frolov A.**, Oparin R., Kiselev M., "Nearest neighbor assessments of spatial distribution in sub- and super-critical CO2: A molecular dynamics analysis", *J. Phys. Chem. B* **2009**, *113*, 15820.

Conference presentations

a) oral presentations :

1. **Frolov A. I.**, "Ion Interactions with Carbon Nanotube and Biomolecular Surfaces", *DUE-L workshop*, Sundern/Hagen, Germany, **2010**.
2. **Frolov A. I.**, Rozhin A. G., Fedorov M. V., "Interaction of Halide Anions with the Carbon Nanotube Surface in Water: a Molecular Dynamics Study", *Trilateral seminar (Russia-Germany-France): Solvation in Complex Liquids: Bridging Length Scales by Theory and Experiment*, Leipzig, Germany, **2010**.
3. **Frolov A. I.**, Kiselev M. G., Fedorov M. V., "Structure of the aliphatic alcohols on the binodal curve", *RCCT2009: XVII International Conference on Chemical Thermodynamics in Russia*, Kazan’, Russia, **2009**.
4. **Frolov A. I.**, Kiselev M. G., Fedorov M. V., "Structure of the aliphatic alcohols in supercritical state", *5th International Theoretical and Practical Conference "Supercritical Fluids: Fundamentals, Technologies, Innovations"*, Suzdal’, Russia, **2009**.
5. **Frolov A. I.**, Oparin R. D., Kiselev M. G., "Investigation of local structure of supercritical CO2 on an isobar with the IR-spectroscopy and MD-simulation", *II Regional conference of young scientists "Theoretical and experimental chemistry of liquid systems"*, Ivanovo, Russia, **2007**.
6. Kiselev M. G., **Frolov A. I.**, Oparin R. D., Fedotova M. V., "Self-organization of carbon dioxide structure at isothermal compression", *XVI International Conference on Chemical Thermodynamics in Russia*, Suzdal, Russia, **2007**.
7. Oparin R. D., **Frolov A. I.**, Kiselev M. G., "Local structure investigation of Supercritical CO2 under isobaric heating conditions based on IR-spectroscopy and MD-modeling data", *IV International Scientific-Practical Conference “Supercritical fluids: Basic foundations, technologies, innovations”*, Kazan’, Russia, **2007**.

8. **Frolov A. I.**, "Local structure of supercritical CO2 based on the molecular dynamics data", *Students scientific conference "Scientific Days-2009"*, Ivanovo State University of Chemical Technology, Ivanovo, Russia, **2007**.

b) poster presentations:

1. **Frolov A. I.**, Rozhin A. G., Fedorov M. V., "Ion Interactions with the Carbon Nanotube Surface in Aqueous Solutions", *241st American Chemical Society (ACS) National Meeting and Exposition* COMP division, Anaheim, California, USA, **2011**.
2. **Frolov A. I.**, Rozhin A. G., Fedorov M. V., "Ion Interaction with the Carbon Nanotube (CNT) Surface in Aqueous Solutions: Modelling Aspects", *Trilateral seminar (Russia-Germany-France): Solvation in Complex Liquids: Bridging Length Scales by Theory and Experiment*, Leipzig, Germany, **2010**.
3. **Frolov A. I.**, Kiselev M. G., Fedorov M. V., "From subcritical to supercritical state: percolation transition in van der Waals clusters", *EMLG-JMLG Annual Meeting 2009: Intermolecular Interactions and Liquid Structure*, Salzburg, Austria, **2009**.
4. Oparin R. D., Fedotova M. V., **Frolov A. I.**, Kiselev M. G., "An investigation of associative ability of the sub- and supercritical carbon dioxide molecules under isothermal compression and isobaric heating", *International conference “Modern Physical Chemistry for Advanced Materials”*, Kharkiv, Ukraine, **2007**.

The biography is not included in the online version for reasons of data protection

The biography is not included in the online version
for reasons of data protection

The biography is not included in the online version for reasons of data protection

The biography is not included in the online version for reasons of data protection

7.5 Erkärung

Hiermit versichere ich, dass ich die vorliegende Arbeit mit dem Titel

"Ion Interactions with Carbon Nanomaterial Surfaces in Aqueous and Non-aqueous Solutions"

selbst verfasst und keine außer den angegebenen Hilfsmitteln und Quellen benutzt habe, und dass die Arbeit in dieser oder ähnlicher Form noch bei keiner anderen Universität eingereicht wurde.

Essen, im Juni 2011

7.6 Acknowledgements

It is a pleasure to thank all the people who made this thesis possible.

First and foremost I offer my deep and sincere gratitude to my scientific supervisor, Dr. Maxim V. Fedorov, PhD, DSc, Priv.-Doz., Leader of the Computational Physical Chemistry and Biophysics Group at the Max Planck Institute for Mathematics in the Sciences. He helped me and advised me during the whole period of my studies. I would like to thank him for scientific expertize I acquired working in his group. He taught me how to organize working time, efficiently communicate with colleagues and the whole set of skills for the efficient scientific work.

I would like to express my deepest appreciation to Prof. Dr. Eckhard Spohr and Prof. Dr. Dr. h.c. Wolfgang Hackbusch for their invaluable assistance encouragement and help during the work on this thesis. I would like to show my gratitude to Prof. Philippe A. Bopp for his guidance consultations on the theory behind the computer simulation, and especially on modelling the ionic solutions. I would like to express my deepest appreciation to Prof. Michail G. Kiselev from the Institute of Solution Chemistry of Russian Academy of Sciences for his support. Without the knowledge I acquired under his supervision during my BSc and MSc studies this PhD thesis would not be possible.

I am grateful to Prof. Arkady M. Kolker and Prof. Anatoly G. Zakharov for supporting me during my BSc and MSc studies.

I would like to thank many teachers from the Ivanovo State University of Chemistry and Technology and the Institute of Solution Chemistry of the Russian Academy of Science: Prof. Dr. Yuriy V. Chistyakov, Prof. Dr. Olga V. Lefedova, Dr. Alexander V. Burov, Prof. Dr. Lubov P. Safonova, Prof. Dr. Georgiy V. Girichev, Prof. Dr. Alexander I. Maksimov, Prof. Dr. Michael V. Ulitin, Prof. Dr. Elena V. Antina, and Dr. Elena L. Gavrilova for their deeply interesting lectures in fields of general chemistry, computational chemistry, mathematics, physics, physical chemistry, biochemistry, etc.

I am grateful to Prof. Margarida C. Gomes for the information on the ionic liquid solubility in acetonitrile.

I owe my deepest gratitude to my co-workers: Anastasia O. Romanova, Raz N. Arif and Martin Kolar for the experimental work they conducted on the carbon nanotube dispersions in N-methyl-2-pyrrolidone. I am very thankful to Dr. Aleksey G. Rozhin for inviting me to the Aston university for the collaborative project and inspired discussions on the correlations between simulation and experimental data. I would like to thank my co-workers Kathleen

Kirchner for helpful scripts to assign molecules potential parameters and Tom Kirchner for the help in the literature search and finding correlations between experimental and simulation data.

I am very thankful to Prof. Gennady N. Chuev for the helpful discussions and teaching me statistical mechanics. I am indebted to my colleagues in the Max Planck Institute for mathematics in the Sciences: Dr. Nicolaj Georgi, Dr. David S. Palmer and Roman Saburdjajew to support me. I am grateful to Ekaterina L. Ratkova for the help in QM calculations.

I am very grateful to the Guest support service of Max Planck Institute for providing me with an environment where I can do my research without spending much time on practical everyday matters associated with my living in Leipzig (accommodation, visas, etc). Honestly speaking, I have not seen any better support service for scientists anywhere else. I am particularly thankful to our Guest Program Manager, Ms. Heike Rackwitz, who made my movement to the Institute to be very easy and well organized. Ms. Rackwitz very quickly resolved all the visa-related issues, registrations, etc. Really, I had many issues related with the everyday life in Germany (doctors, residence permits, etc) and all the time our administrators helped me to solve them in a very efficient way. I am very thankful to Ms. Valeria Hünniger for her care and support. She made all my business trips easy: she did booking of the hotels and flight and train tickets and so on. I am very grateful to all our secretaries and members of our Library Group (led by Mr. Ingo Brüggemann) and Computer Group (led by Mr. Rainer Kleinrensing) for their daily work to organize our living and working in the Institute: Ms. Valeria Hünniger, Ms. Theresa Petsch, Ms. Elke Herrmann, Ms. Katrin Scholz, Ms. Saskia Gutzschebauch, Ms. Gertraude Torkler, Ms. Jana Gregor, Ms. Antje Vandenberg, Ms. Johanna Göpfert, and Ms. Katarzyna Baier. I really appreciate this support as it allows me to fully concentrate on my scientific problems without spending much time on the organization of everyday life.

I am very grateful to secretaries and members of International Office of the University of Duisburg-Essen: Ms. Gudrin Ciolek, Ms. Olga Zaglov, and Ms. Elke Kalle. Their advertence, invaluable assistance, and consultations have been an important support throughout this thesis.

I acknowledge the supercomputing support from the John von Neumann-Institut für Computing (NIC), Juelich Supercomputing Centre (JSC), Forschungszentrum Juelich GmbH, Germany. Project ID: HLZ16 and HLZ18. I am very grateful to Dr. Godehard Sutmann for the expertize in the field of modelling the electrostatic interactions. I acknowledge Deutsche Forschungsgemeinschaft (DFG) - German Research Foundation, Research Grant FE 1156/2-1. Some part of the work has been performed under the HPC-EUROPA2 project (project number: 228398) with the support of the European Commission - Capacities Area - Research Infrastructures. Part of the computations were performed with the facilities of HECToR, the UK's national high-performance computing service, which is provided by UoE HPCx Ltd at the University of Edinburgh, Cray Inc and NAG Ltd, and funded by the Office of Science and Technology through EPSRC's High End Computing Programme. I am very thankful to Dr. Chris Johnson for the technical support.

I would like to acknowledge the use of the Max Plack Society supercomputing center facilities in Garching. I am very thankful to the computer support in Garching supercomputer center, and especially to Dr. Ingeborg Weidl.

My special gratitude is due to my mother, Olga Yu. Frolova, my father, Igor V. Frolov, and my sister Anna I. Frolova for their loving support. I would like to thank my cousin, Alexander V. Borodin, for opening for me the field of theoretical chemistry. I acknowledge the use of the VMD software for visualization of the simulation results [194].